

8-30-2011

Polymerization in emulsion microdroplet reactors

Nick J. Carroll

Follow this and additional works at: https://digitalrepository.unm.edu/cbe_etds

Recommended Citation

Carroll, Nick J.. "Polymerization in emulsion microdroplet reactors." (2011). https://digitalrepository.unm.edu/cbe_etds/9

This Dissertation is brought to you for free and open access by the Engineering ETDs at UNM Digital Repository. It has been accepted for inclusion in Chemical and Biological Engineering ETDs by an authorized administrator of UNM Digital Repository. For more information, please contact disc@unm.edu.

Nick J. Carroll

Candidate

Chemical and Nuclear Engineering


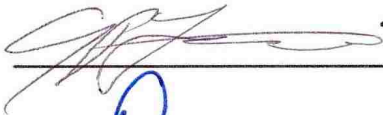
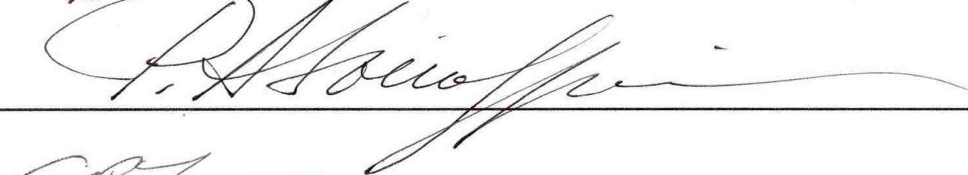
Department

This dissertation is approved, and it is acceptable in quality and form for publication:

Approved by the Dissertation Committee:



, Chairperson



POLYMERIZATION IN EMULSION MICRODROPLET REACTORS

BY

NICK J. CARROLL

B.S. Chemical Engineering, University of New Mexico, 2006.

DISSERTATION

Submitted in Partial Fulfillment of the
Requirements for the Degree of

**Doctor of Philosophy
Engineering**

The University of New Mexico
Albuquerque, New Mexico

July, 2011

© 2011, Nick J. Carroll

DEDICATION

To my daughter Nicole, I hope my education lights the path for your own dreams and success.

ACKNOWLEDGEMENTS

I would like to thank my advisor, Dr. Dimiter Petsev, for being my teacher and mentor over the course of this dissertation work. Thank you for your guidance, willingness to impart knowledge, patience, and encouragement. Working under you was an honor. I would also like to extend a sincere thank you to my dissertation committee, Dr. David Weitz, Dr. Gabriel Lopez, and Dr. Plamen Atanassov for their generosity with resources, guidance, and encouragement. Thanks to my colleague and friend, Dr. Sergio Mendez, for teaching me about the politics of this business. Also, I would like to thank Peter Crowder, my undergraduate research assistant who was a great help in finishing this dissertation work.

On a personal note, I would like to acknowledge my parents, Roy and Anna Carroll. My father taught me the value of hard work (to be a ‘bulldog’) and to always strive to be a good man. My mother is my heart and inspiration, thank you for your unconditional love. Thank you to John and Marie Garcia for your support, encouragement, and belief in me. Thank you to my Jonnie, for your infinite support and patience. You were with me every step of this long and sometimes lonely journey; without you I would have never made it this far, I will be forever grateful.

This work was supported by the NSF/PREM (DMR 0611616), NSF/IGERT (DGE 0549500), and DoE-EPSCoR Implementation Program: Materials for Energy Conversion.

POLYMERIZATION IN EMULSION MICRODROPLET REACTORS

BY

NICK J. CARROLL

ABSTRACT OF DISSERTATION

Submitted in Partial Fulfillment of the
Requirements for the Degree of

**Doctor of Philosophy
Engineering**

The University of New Mexico
Albuquerque, New Mexico

July, 2011

Polymerization in Emulsion Microdroplet Reactors.

By

Nick J. Carroll

B.S., Chemical Engineering, University New Mexico, 2006
Ph.D., Chemical Engineering, University of New Mexico, 2011

Abstract

The goal of this research project is to utilize emulsion droplets as chemical reactors for execution of complex polymerization chemistries to develop unique and functional particle materials. Emulsions are dispersions of immiscible fluids where one fluid usually exists in the form of drops. Not surprisingly, if a liquid-to-solid chemical reaction proceeds to completion within these drops, the resultant solid particles will possess the shape and relative size distribution of the drops. The two immiscible liquid phases required for emulsion polymerization provide unique and complex chemical and physical environments suitable for the engineering of novel materials.

The development of novel non-ionic fluorosurfactants allows fluorocarbon oils to be used as the continuous phase in a water-free emulsion. Such emulsions enable the encapsulation of almost any hydrocarbon compound in droplets that may be used as separate compartments for water-sensitive syntheses. Here, we exemplify the promise of this approach by suspension polymerization of polyurethanes (PU), in which the liquid precursor is emulsified into droplets that are then converted 1:1 into polymer particles. The stability of the droplets against coalescence upon removal of the continuous phase by evaporation confirms the formation of solid PU particles. These results prove that the water-free environment of

fluorocarbon based emulsions enables high conversion. We produce monodisperse, cross-linked, and fluorescently labeled PU-latexes *with controllable mesh size* through microfluidic emulsification in a simple one-step process.

A novel method for the fabrication of monodisperse mesoporous silica particles is presented. It is based on the formation of well-defined equally sized emulsion droplets using a microfluidic approach. The droplets contain the silica precursor/surfactant solution and are suspended in hexadecane as the continuous oil phase. The solvent is then expelled from the droplets, leading to concentration and micellization of the surfactant. At the same time, the silica solidifies around the surfactant structures, forming equally sized mesoporous particles. The procedure can be tuned to produce well-separated particles or alternatively particles that are linked together. The latter allows us to create 2D or 3D structures with hierarchical porosity.

Oil, water, and surfactant liquid mixtures exhibit very complex phase behavior. Depending on the conditions, such mixtures give rise to highly organized structures. A proper selection of the type and concentration of surfactants determines the structuring at the nanoscale level. In this work, we show that hierarchically bimodal nanoporous structures can be obtained by templating silica microparticles with a specially designed surfactant micelle/microemulsion mixture. Tuning the phase state by adjusting the surfactant composition and concentration allows for the controlled design of a system where microemulsion droplets coexist with smaller surfactant micellar structures. The microemulsion droplet and micellar dimensions determine the two types of pore sizes (single nanometers and tens of nanometers). We also demonstrate the fabrication of carbon and carbon/platinum replicas of the silica microspheres using a “lost-wax” approach. Such particles have great potential for the design of

electrocatalysts for fuel cells, chromatography separations, and other applications. It was determined that slight variations in microemulsion mixture components (electrolyte concentration, wt% of surfactants, oil to sol ratio, etc.) produces strikingly different pore morphologies and particle surface areas. Control over the size and structure of the smaller micelle-templated pores was made possible by varying the length of the hydrocarbon block within the trimethyl ammonium bromide surfactant and characterized using X-ray diffraction. The effect of emulsion aging was studied by synthesizing particles at progressive time levels from a sample emulsion. It was discovered surface pore size increases after just a few hours, with high number of hollow particles observed. After 3 days, the particles were irregular shaped with little surface porosity observed via scanning electron microscopy. This may indicate that the microemulsion in the standard synthesis is not at equilibrium and that the alkoxide monomer, tetraethylorthosilicate, may change surface activity over time as additional levels of hydrolysis are obtained.

Monodisperse, microemulsion nanoporous particles were synthesized utilizing a microfluidic platform. Emulsification of silica precursor in a pure oil phase at the microfluidic orifice, with infusion of surfactant-laden oil phase into the device downstream of the orifice, allows for successful fluidic treatment of a low interfacial tension system and the formation of monodisperse particles. Temperate evaporation of the solvent from the droplets at ambient conditions preserves the excellent size distribution of the fluidic-formed precursor droplets during gelation. Successful synthesis of monodisperse silica particles with bimodal nanoporosity demonstrates engineering control at three different length scales: the nanoscale via surfactant molecular templating, tens of nanometers via spontaneous microemulsion

templating and at the micron level through control of overall size distribution via a microfluidic platform.

Table of Contents

Abstract	vii
Table of Contents	xi
- Introduction	1
1.1 Emulsion Science	3
1.2 Droplet-Based Microfluidics	8
1.2.1 Soft Lithography	10
1.2.2 Pressure-Driven Microdroplet Formation.....	11
1.3 Nanoporous Particles.....	18
1.3.1 Sol-Gel Processing of Silica.....	18
1.3.2 Surfactant Self Assembly	21
1.4 Characterization Techniques	24
1.4.1 Dynamic Light Scattering.....	25
1.4.2 Interfacial Tension Measurements	26
1.4.3 Scanning Electron Microscopy.....	29
1.4.4. Transmission Electron Microscopy.....	31
1.4.5 X-Ray Diffraction.....	32
1.4.6 Nitrogen Sorption Analysis	35
1.5 Research Goals	40

Monodisperse Particle Synthesis in Microfluidic Droplet Reactors.....42

2.1 Synthesis of Monodisperse Polyurethane Latex Microspheres..... 42

 2.1.1 Methods 44

 2.1.2 Results/Discussion..... 48

 2.1.3 Conclusion..... 55

2.2 Droplet-Based Microfluidics for Emulsion and Solvent Evaporation Synthesis of Monodisperse Mesoporous Silica Microspheres..... 56

 2.2.1 Introduction 56

 2.2.2 Materials and Methods 57

 2.2.3 Results/Discussion..... 59

 2.2.4 Concluding Remarks 65

Microparticles with Bimodal Nano-Porosity Derived by Microemulsion

Templating.....67

3.1 Introduction 67

3.2 Experimental Approach..... 69

3.3 Microemulsion Templated Silica Results/Discussion..... 71

3.4 Microemulsion Templated Silica Concluding Remarks 83

3.5 Microemulsion Templated Niobium Oxide 84

3.7 Emulsion Aging/Surface Tension Studies..... 93

Droplet-Based Microfluidics for Synthesis of Monodisperse Silica Particles with Multi-Modal Nanoporosity.....	101
4.1 Introduction	101
4.2 Experimental Methods	104
4.3 Results/Discussion	107
4.4 Conclusion.....	115
Templated Platinum/Carbon Oxygen Reduction Fuel Cell Electrocatalysts	116
5.1 Introduction	116
5.2 Experimental Methods	118
5.3 Results and Discussion.....	121
5.4 Conclusions	137
6.1 Summary	139
6.2 Conclusions	143
6.3 Recommendations for Future Work	146
References.....	147

List of Figures

Figure 1.1: Polymerization in emulsion droplets provides a rich system which can facilitate mass diffusion in and out of microdroplet reactors and templating of nanostructured materials via interfacial phenomena.	2
Figure 1.2. Winsor Type I microemulsion (O/W), Winsor Type III microemulsion (bicontinuous phase), and Winsor Type II microemulsion (W/O) [8].....	7
Figure 1.3: PDMS device fabricated using soft lithography. There are 10 devices on the chip...	10
Figure 1.4. In flow regimes with low Re , forces associated with viscous shear flow dominate the system and are on the same order as those associated with interfacial forces. This makes microfluidics ideal for controllable droplet formation [23].....	13
Figure 1.5: Droplet Formation in Microchannels	14
Figure 1.6 CFDRC simulation of velocity distributions in channels with different geometries. (a) Orifice connected to long straight channel. (b) Orifice connected to a short channel with subsequent rectangular expansion. (c) Orifice connected to an expansion nozzle. This design allows the max velocity to occur at the orifice [24].....	16
Figure 1.7. Microfluidic T-junction diagram. Droplet formation within T-junction devices is due to a pressure drop across the emerging droplet and independent of shear stress. Image reproduced from [23].	17
Figure 1.8: Acid and base catalyzed silica sol-gel reactions.	20
Figure 1.9. Left: The packing parameter, g . Right: Packing parameter, g , and corresponding aggregate structures.	22

Figure 1.10. Surfactant liquid crystalline structures can form as shown in this surfactant/aqueous solution/oil phase diagram [75].	23
Figure 1.11. Left: Diagram of Du Nouy ring. Right: Force versus displacement for the ring. The maximum force, F_3 is used to estimate surface or interfacial tension.	28
Figure 1.12. Single lens configuration of a TEM.	32
Figure 1.13. Diffraction of X-rays from sets of crystal planes.	34
Figure 2.1: Isocyanates can react to form urethanes, if the stoichiometry of isocyanates to alcohol is 1:1. However, they react much more rapidly with water forming an amine that then reacts with another isocyanate to form a urea bond.....	43
Figure 2.2: Krytox-b-PEG-b-Krytox triblock copolymers were coupled by an amide bond. These amphiphilic molecules stabilize organic-in-fluorocarbon emulsions.....	45
Figure 2.3. The geometry of the surfactant can be tuned by adjusting relative chain length of the perfluoro- or PEG blocks (top) or the number of blocks coupled (bottom).	46
Figure 2.4. (Top) A stable emulsion will have a uniform, opaque appearance, while an unstable emulsion (Bottom) will not be uniformly opaque and will instead contain regions where droplet coalescence or phase separation is observed.	47
Figure 2.5: . Micrographs of Fluorescein-labelled polyurethane particles obtained through suspension polymerization. Left: brightfield. Right: cross-polarization. Stable, polydisperse emulsions were obtained from shaking the precursor and the fluorocarbon oil in the pre the presence of non-ionic fluorosurfactants. Drying a partially converted emulsion on a glass slide is a simple way to confirm conversion: Particles with low conversion coalesce, whereas fully converted particles remain stable. Low conversion is also indicated by the lack of	

fluorescence – unreacted isocyanates quench fluorescein, which acts as a probe for conversion.....	49
Figure 2.6: Microfluidic emulsification produces monodisperse emulsion droplets that can be converted 1:1 into solid polyurethane particles. a) Micrograph of a monodisperse precursor emulsion in a fluorocarbon oil. b) Micrograph of dried monodisperse polyurethane latex particles.....	50
Figure 2.7: Micrographs of the dried, fluorescently labeled, monodisperse particles of a polyurethane latex. The synthesis of fluorescent particles is one example of chemical modification through the addition of functional reagents to the PU-precursor.....	51
Figure 2.8: Cross-linked and fluorescently labeled polyurethane particles obtained from suspension polymerization in a single processing step. The addition of THF swells, but does not dissolve the particles, indicating high conversion and efficient cross-linking.....	52
Figure 2.9: Demonstration of the versatility of PU-suspension polymerization: Diluting the precursor before emulsification with an inert solvent allows the mesh size of cross-linked particles to be tuned. The micrographs show particles that were polymerized while being diluted 1:1 with DMSO. The wrinkles appear upon drying of the particles.....	54
Figure 2.10. Left: Silica precursor drops suspended in hexadecane; Right: Silica particles after EISA processing. The droplets shrink ~ 50% due to the evaporation process.....	59
Figure 2.11: (a) Polydisperse silica microspheres templated from shaken bulk emulsion. Scale bar is 20 μm . (b) Silica microspheres templated by monodisperse microfluidic device-generated droplets. Scale bar is 100 μm . (c) Scanning electron microscopy image and (d) optical photograph (scale bar is 40 μm) of particles that have fused together in a hexagonal array. The particles are connected by “bridges” which form when the particles come into	

contact before the completion of the gelation process. The particles were then collected and centrifuged followed by calcination in air at 500 °C for 5 h to remove the templating surfactant. 60

Figure 2.12: TEM image of P104 templated mesoporous silica particles (scale bar is 1 μm). 62

Figure 2.13. Nitrogen sorption isotherm for emulsion and evaporation synthesized silica particles. 63

Figure 2.14: TEM of hexagonally ordered cylindrical nanopores obtained by the emulsion and solvent evaporation method. 64

Figure 3.1: Sketch of liquid silica precursor emulsion system. (a) Aqueous silica precursor emulsion drops (light gray) in hexadecane oil (dark gray). Microemulsion droplets form and occupy the internal drop volume (small dark gray circles). (b) Single aqueous silica precursor drop. The CTAB is above the CMC forming, micelles (red) in addition to microemulsion droplets (dark gray). (c) Oil/water interface with adsorbing surfactants from the two immiscible phases. 71

Figure 3.2: DLS of aqueous silica precursor solution suggest the presence of structures in the single nanometers existing with structures with dimensions in the tens of nanometers. 73

Figure 3.3: (a), (b): SEM images of microemulsion templated silica particles; (b), (c): SEM images indicate large pores are present throughout template silica particles. 74

Figure 3.4: (a) TEM image of microemulsion templated silica suggest pores open at surface; (b), (c) TEM images of cross-sectioned silica particles. 75

Figure 3.5: XRD for microemulsion templated silica suggests presence of smaller pores, hexagonally ordered, with a d-spacing of ~6 nm. 76

Figure 3.6: (top): Nitrogen sorption isotherm; (bottom) pore size distribution using NLDFT model.....	77
Figure 3.7. Isotherm of a typical plugged hierarchically porous silica material [115].....	78
Figure 3.8: Characterization of templated carbon particles and template carbon particles decorated with platinum nanoparticles. (a) SEM image of carbon particle surface. (b) TEM image of the carbon particle cross section showing the internal structure. (c) TEM of the template carbon particle decorated with platinum nanoparticles. (d) TEM of the cross section of templated carbon particle decorated with platinum nanoparticles showing the internal structure and dispersion of the platinum nanoparticles. (e) TEM of the templated carbon particle decorated with platinum nanoparticles at higher magnification.	80
Figure 3.9. Electrochemical characterization of the template 30%wt.Pt/ and 30%wt.Pt/Vulcan XC-72R. Cyclic voltammograms in rotating disk electrode configuration were obtained in 0.1 M HClO ₄ saturated with O ₂ at 25°C at 10mV/s and 1600rpm. The catalyst loading was 20.5 μgPt/cm ² for Pt supported on templated carbon and 21.7 μgPt/cm ² for Pt supported on Vulcan XC-72R, from ETEK. The steep slopes on the right for both curves demonstrate the Pt-catalyst behavior.....	82
Figure 3.10: Niobium oxide particles formed via microemulsion templating.....	85
Figure 3.11. Different pore morphologies and particle surface areas created by varying microemulsion mixture components. Particles formed by: (a) Standard microemulsion mixture, BET surface area 1000 m ² /g. (b) Adding 0.075 M NaCl, BET surface area 650 m ² /g. (c) Adding 0.15 M NaCl, BET surface area 850 m ² /g. (d) 2:1 oil to water ratio, BET surface area 1038 m ² /g. (e) Reducing molar concentration of Abil EM-90 surfactant by 25%, BET	

surface area 975 m ² /g. (f) Increasing mass of CTAB surfactant by 25%, BET surface area 1250 m ² /g.	86
Figure 3.12. TEM of standard microemulsion templated silica. The rough surface of the particles prevents their use as drug-delivery ‘protocells.’	88
Figure 3.13. (top) Nitrogen isotherm and (bottom) Pore size distribution of multimodal silica particles.	89
Figure 3.14. Multimodal silica particles used as drug delivery vehicles. Fluorescence imaging of liposome fused particles in cell nucleus, loaded with quantum dots [127].	90
Figure 3.15. XRD data for mesoporous silica particles. The first peak is for the standard CTAB templating surfactant, with each subsequent peak representing material templated with a cationic trimethyl ammonium bromide surfactant each with progressively one less methyl group within the hydrophobic chain.	92
Figure 3.16. Silica particles formed after EISA processing of the emulsion after (a) t = 0; (b) t = 3 hrs; (c) t = 24 hrs; (d) t = 3 days.	94
Figure 3.17. Silica particles processed 3 days after emulsification.	95
Figure 3.18. Complete phase separation is observed for Q0 organic TEOS in water and HCl (a) even under vigorous stirring (b). Upon hydrolysis, no phase separation is observed (c) and the solution foams upon shaking (d) indicating partially hydrolyzed TEOS is surface active.	96
Figure 3.19. Surface tension measurements indicate hydrolyzed TEOS is surface active, lowering the measured surface tension of an H ₂ O+HCl solution from 69 mN/m to 34 mN/m. ...	97
Figure 3.20. Particle from 3 day aged emulsion. Micron-sized cavities (arrows) ‘fossilized’ within the particles indicate possible oil droplet coalescence.	98

Figure 3.21. Surface tension of H₂O+HCl+TEOS solution evolving with time from t = 0 (initial hydrolysis) to 90 hours. The rapid increase in surface tension in the first few hours followed by a gradual increase over the next few days follows the trend of surface pore change observed from SEM images in figure 3.16..... 99

Figure 4.1. Polydisperse silica particles with bimodal nanoporosity. The emulsions were prepared in bulk using inhomogeneous vigorous stirring. As a result, the droplets, and therefore the particles, were produced with a broad size distribution. (Scale bar is 20 μm)..... 103

Figure 4.2 Microfluidic configuration. Aqueous silica precursor (1) is emulsified in a 10 μm diameter orifice with pure hexadecane oil (2,3). Droplets travel down the 10 μm diameter channel where hexadecane with 2 wt% Abil EM90 surfactant (4,5) is added allowing the microemulsion phase to form and penetrate the aqueous silica precursor droplets (6). The droplets are collected in a reservoir (6 mm diameter) where EISA is carried out at ambient pressure and temperature. 106

Figure 4.3. Aqueous silica precursor droplets in hexadecane oil phase. Opaqueness is observed in the continuous phase near the droplets (Scale bar 20 μm). 108

Figure 4.4. Silica particles in hexadecane oil phase after evaporative processing. (Scale bar is 15 μm). 109

Figure 4.5. SEM image of monodisperse microemulsion-templated silica particles. 110

Figure 4.6. SEM micrograph shows existence of smaller particles due to satellite droplet formation (arrows) and large particles due to droplet coalescence (circle). 111

Figure 4.7. SEM micrograph showing surface morphology of microemulsion templated particles. Surface cavities are ~40 nm in diameter as was observed in previous synthesis experiments using a bulk emulsion system [125]. 113

Figure 4.8. Successful synthesis of monodisperse silica particles with bimodal nanoporosity demonstrates control at three different length scales: the nanoscale via surfactant molecular templating, 10s of nanometers length scale via spontaneous microemulsion templating, and at the micron level through control of overall size distribution through microfluidic platform..... 114

Figure 5.1. SEM images of a) silica particle, b) silica particle at higher magnification demonstrating open structure of the surface, c) templated carbon particles decorated with platinum nanoparticles, after pyrolysis and silica removal and d) templated carbon particles decorated with platinum nanoparticles after pyrolysis and silica removal, at higher magnification demonstrating templated structure..... 121

Figure 5.2. HRTEM micrographs of cross sections of a) silica particle showing porous structure obtained by templating with micelles and microemulsion droplets, b) carbon particle after pyrolysis and silica removal demonstrating the internal porous structure, and c) templated carbon particle decorated with platinum nanoparticles after pyrolysis and silica removal showing the dispersion of platinum nanoparticles..... 122

Figure 5.3. HRTEM images of 30 wt% Pt/TC a) showing edge of the carbon particle , and b) higher magnification image demonstrating size and dispersion of platinum nanoparticles. 124

Figure 5.4. HRTEM images of 30 wt% Pt/TC a) showing edge of the carbon particle , b and c) higher magnification images demonstrating size and dispersion of platinum nanoparticles. 125

Figure 5.5. Representative high-resolution XPS spectra of Pt/TC materials a) Pt 4f spectrum and b) C 1s spectrum..... 126

Figure 5.6. XRD patterns of Pt/TC materials a) 10 wt% Pt/TC and b) 30 wt% Pt/TC. 127

Figure 5.7. RDE polarization curves in 0.1M HClO₄ solution saturated with O₂ at 25 °C and 1600 rpm. Scan rate is 10 mV/s. Catalyst loading is 9.1 μg_{Pt}/cm² for 10 wt% Pt/TC, 20.5 μg_{Pt}/cm² for 30 wt% Pt/TC and 9.6 μg_{Pt}/cm² for 10 wt% Pt/Vulcan XC-72R, ETEK..... 128

Figure 5.8. TGA analysis of a) silica filled with carbon precursor (sucrose) and b) silica filled with carbon (sucrose) and platinum (H₂PtCl₆·6H₂O) precursors. Conditions of the TGA analysis simulate conditions of the pyrolysis..... 130

Figure 5.9. Polarization curves in RDE in 0.1M HClO₄ solution saturated with O₂ at 25 °C and 1600 rpm. Scan rate is 10 mV/s. Catalyst loading is 9.1 μg_{Pt}/cm² for GEN1 and GEN2 10 wt% Pt/TC, pyrolyzed at 900 °C, and 9.6 μg_{Pt}/cm² for 10 wt% Pt/Vulcan XC-72R, ETEK. 131

Figure 5.10. Polarization curves in RDE in 0.1M HClO₄ solution saturated with O₂ at 25 °C and 1600 rpm. Scan rate is 10 mV/s. Catalyst loading is 9.1 μg_{Pt}/cm² for GEN2 10 wt% Pt/TC, pyrolyzed at various temperatures, and 9.6 μg_{Pt}/cm² for 10 wt% Pt/Vulcan XC-72R, ETEK. 133

Figure 5.11. Polarization curves obtained during MEA testing with H₂/O₂ gas feeds heated and humidified at 85 °C and 30 psi backpressure. The cell temperature is 80 °C. Cathode catalyst is GEN2 10 wt% Pt/TC..... 135

- Introduction

An emulsion is a mixture of two or more liquids in which one is present on the form of droplets, of microscopic or ultramicroscopic size, distributed throughout the other. Macro emulsions are thermodynamically unstable and are typically formed from the component liquids by mechanical means such as agitation provided that the liquids that are mixed have no (or a very limited) mutual solubility. Because macro emulsions are thermodynamically unstable, kinetic stabilization is required to maintain the formed drops. Emulsions are kinetically stabilized by agents that form films at the surface of the droplets (*e.g.*, surface active molecules) or that impart to them a mechanical stability (*e.g.*, colloidal carbon or bentonite). Unstable emulsions eventually separate into two liquid phases. Far less frequently, emulsion systems known as microemulsions can spontaneously form upon combining of specially selected emulsion mixture components. Microemulsions are thermodynamically stable with droplet dimensions in the tens of nanometers. Emulsions are utilized in many fields: pharmaceuticals, the oil industry, the food industry, dyeing and tanning industries, in the manufacture of synthetic rubber and plastics, in the preparation of cosmetics such as shampoos, and of salves and therapeutic products (*e.g.*, sun-block lotions). Emulsions tend to have a cloudy or opaque appearance, because the droplets can scatter light that passes through the emulsion.

Emulsion polymerization is defined herein as emulsification of an inorganic, organic, or biological polymer precursor followed by execution of the polymer chemistry within emulsion droplet reactors. Emulsion polymerization is used in the production of a wide range

of specialty polymers including adhesives, paints, binders for nonwoven fabrics, additives for paper, textiles and construction materials, impact modifiers for plastic matrices, diagnostic tests, and drug-delivery systems. The development of this industry has been due to both the possibility of producing polymers with unique properties and the environmental concerns and governmental regulations to substitute solvent-based systems by waterborne products.

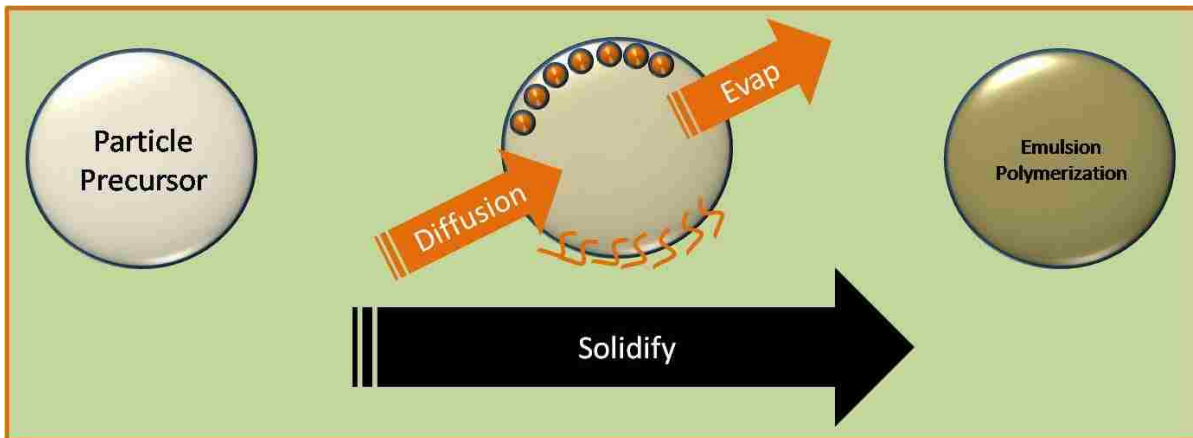


Figure 0.1: Polymerization in emulsion droplets provides a rich system which can facilitate mass diffusion in and out of microdroplet reactors and templating of nanostructured materials via interfacial phenomena.

This type of conventional emulsion polymerization accounts for the majority of the world's production (20×10^6 tons/year). Not surprisingly, if a liquid-to-solid chemical reaction proceeds to completion within emulsion drops, the resultant solid particles will possess the shape of the droplets [1, 2]. The two immiscible liquid phases required for emulsion polymerization provide unique and complex chemical and physical environments suitable for the engineering of novel materials and biological assays (Figure 1.1). Polymerization in microdroplet reactors facilitates control of particle size distribution and morphology [3-5]. Additionally, it allows for controllable diffusion of chemical constituents into and out of the

microdroplet reactors through the surrounding continuous phase [6]. Interfacial phenomena such as surfactant adsorption and spontaneous formation of complex microemulsion phases [7, 8] present exceptional and generally less-explored avenues for particle nanostructure templating. Emulsion polymers are “products by process” whose main properties are determined during polymerization. A critical point is to understand how these process variables affect the final properties of the product. The key to understanding the scientific and engineering components of such complex chemical reaction systems is pursuing knowledge-based strategies that use the polymer microstructure (here, the term microstructure is used in a broad sense including aspects such as copolymer composition, molecular weight distribution, branching, crosslinking, gel fraction, particle morphology, and particle size distribution (PSD) of the dispersion) as a link between the droplet reactor variables and the final physical properties.

1.1 Emulsion Science

The liquid comprising the droplets in emulsion systems are referred to as the dispersed or discontinuous phase, while the surrounding fluid is the continuous phase. At constant volume and temperature, the Gibb’s free energy of forming an emulsion is [9]:

$$\Delta G_{\text{form}} = \gamma\Delta A - T\Delta S^{\text{m}} \quad (1.1)$$

where γ is the interfacial tension, ΔA is the change in interfacial area, T is temperature and ΔS^{m} is the change in entropy gained upon mixing (emulsification). Immiscible fluids in contact can produce a large interfacial tension, therefore the interfacial energy is generally much larger than the entropic contribution and in most cases, and the emulsification process is neither spontaneous nor thermodynamically stable. Adsorption of amphiphilic surfactant

molecules at the droplet interface reduces interfacial energy and provides kinetic stability by providing steric interference between drops (usually polymeric nonionic surfactants) or electrostatic repulsion (typically in oil-in-water (O/W) emulsions). In the case of steric stabilization, the polymer projects loops and tails into the continuous phase and the interaction of these projections hinders the approach of the droplets to one another. An electric charge associated with its double layer is not necessary; even uncharged droplets can be stabilized by this mechanism. Thus steric stabilization may be effective in non-aqueous continuous phases where charge stabilization is unsatisfactory. Factors to be considered when two sterically stabilized droplets approach one another include [10]:

- in regions where the adsorbed layers on the two particles interpenetrate there is an increase in the osmotic pressure which tends to draw more solvent into that region tending to force the droplets apart;
- there may also be changes in the conformations of the polymer loops and tails as the two droplets approach.

The general function of the emulsifying surfactant is to reduce interfacial tension at the droplet interface and provide kinetic stability against coalescence, but there are more subtleties than this simple description would imply. The selection of a suitable emulsifier is a key aspect of emulsion preparation in determining whether an O/W or water-in-oil (W/O) emulsion will form. One of the first attempts to predict emulsion type is known as the Bancroft rule [11] which simply states that the phase in which the emulsifier is the more soluble tends to form the continuous phase.

Further understanding based upon film balance studies, came with the work of Langmuir and Harkins which showed that the emulsifier forms an oriented monolayer at the oil-water interface. The oriented wedge theory of Harkins arises from this insight and suggests that the end of the emulsifier molecule with the loosely defined 'larger size' will lie in the continuous phase. Further work by Winsor and Bancroft considered 10 different cohesive energies, including those between the hydrophilic part of the surfactant and water (E_{HW}) and between the lipophilic (or hydrophobic) block of the surfactant and oil (E_{LO}). When these two cohesive energies are greater than the other cohesive energies then the ratio [12]:

$$R = \frac{E_{LO}}{E_{HW}}$$

determines the type of emulsion formed: if $R < 1$, and O/W emulsion forms; whereas for $R > 1$, a w/o emulsion is formed. Such emulsions are designated *Winsor I* and *Winsor II* respectively.

Dynamic effects also contribute to droplet kinetic stability. When two drops approach, the flow or draining of liquid from between them (a necessary condition for coalescence) is retarded by the concomitant dilution of the emulsifier film at the interface. This produces a gradient in interfacial tension, with interfacial tension higher in the interparticle region than elsewhere on the drops, so fluid convective flow tends to move emulsifier back to the interparticle region while dragging fluid back with it, thereby impeding coalescence. The viscosity of the interfacial film fluid also affects such movements and coalescence events.

If a fluid interface is curved the pressures on either side must be different. The pressure inside of an emulsion droplet is greater than that outside. For a system at equilibrium, every part of the interface must be in mechanical equilibrium. For a curved interface, the forces of surface tension are exactly balanced by the differences in pressure on the two sides of the interface. This is expressed by the Laplace equation:

$$\Delta P_L = \frac{2\gamma}{r} \quad (1.2)$$

which holds for a spherical interface of radius r . Thus, droplets within high-interfacial tension systems produce a large Laplace pressure and are less deformable and susceptible to shearing than those in a low-interfacial tension system.

At ultra low interfacial tensions ($\sim 10^{-3}$ mN/m or lower) the entropic term in the Gibb's free energy of forming an emulsion (equation 1.1) is greater than the increase in interfacial energy due to increasing the interfacial area [12]:

$$T\Delta S^m > \gamma\Delta A$$

Thus, $\Delta G < 0$ and an emulsion (typically with droplets < 100 nm diameter) can form spontaneously upon combining of the emulsion components. Microemulsions are thermodynamically stable dispersions of oil and water stabilized by a large surfactant and, in many cases, also a smaller cosurfactant. The microemulsions can be of the droplet type (Figure 1.2), either with spherical oil droplets dispersed in a continuous medium of water (oil-in-water microemulsions, O/W, Winsor Type I) or with spherical water droplets dispersed in a continuous medium of oil (water-in-oil microemulsions, W/O, Winsor Type

II). The droplet-type microemulsions can be either a single-phase system or part of a two-phase system wherein the microemulsion phase coexists with an excess dispersed phase (an upper phase of excess oil in the case of O/W and a lower phase of excess water in the case of

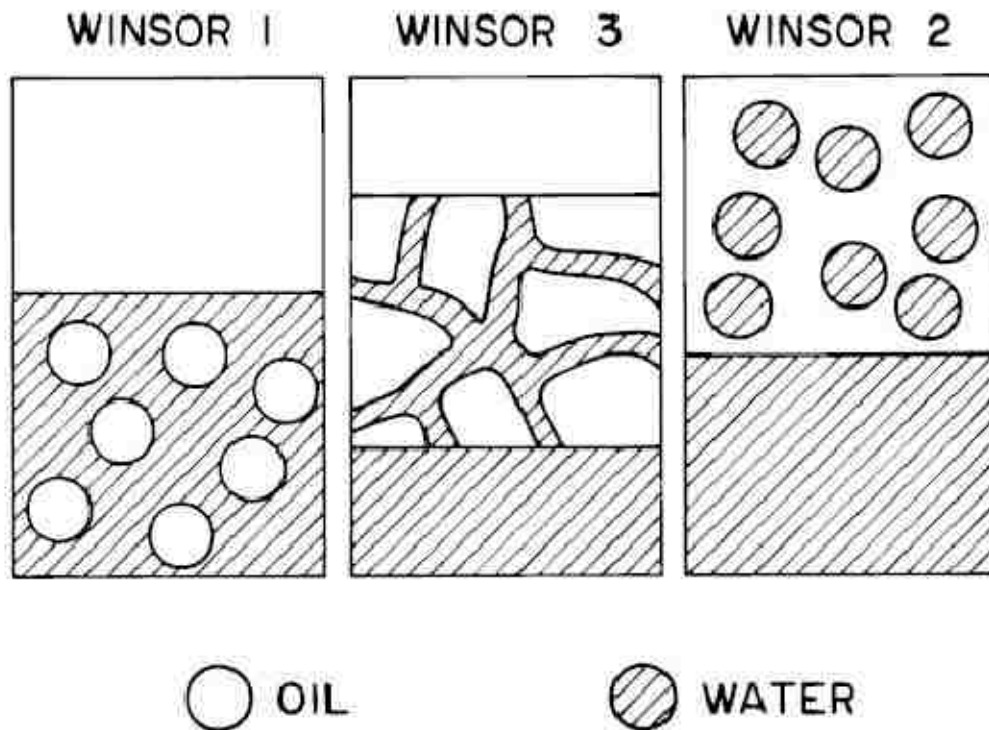


Figure 0.2. Winsor Type I microemulsion (O/W), Winsor Type III microemulsion (bicontinuous phase), and Winsor Type II microemulsion (W/O) [8].

W/O microemulsions). There may also exist nondroplet-type microemulsions, referred to as middle-phase microemulsions (Winsor Type III). In this case, the microemulsion is an equilibrium three-phase system with a mixed phase in the middle coexisting with an upper phase of excess oil and a lower phase of excess water. One possible structure of this middle-phase, characterized by randomly distributed oil and water microdomains and bicontinuity in both oil and water domains, is known as the bicontinuous microemulsion. Because of the

small size of the microemulsion droplets their surfaces are highly curved and it is possible to predict, to a certain extent, whether a particular surfactant or cosurfactant will promote a Winsor Type I or Type II emulsion by examining the shape of the molecules. Large hydrophobic blocks will favor a Winsor Type I, while relatively large hydrophilic groups will favor a Winsor Type II [8]. Microemulsions have found increasing applications in food, pesticides, drug delivery, as well as oil recovery.

There is debate as to whether these systems should be described as emulsions or swollen micelles. However, there are clear distinctions between microemulsions and micelles [13]. As solubilized materials are added to a micelle system, the originally isotropic (approximately spherical) micelles (a few nanometers in diameter) can only swell to a limited extent before they undergo a conformational change to reorganize into different, anisotropic, shapes (i.e. cylinders and lamellae) in order to accommodate the extra material. In contrast, microemulsions are able to accept significantly larger amounts of materials while retaining their isotropic nature, with the caveat that additional surfactant must be available to maintain the interface during swelling.

1.2 Droplet-Based Microfluidics

The miniaturization of chemical flow and analysis systems has opened up exciting avenues of scientific and engineering possibilities. Channels with widths in the tens of micrometer range are referred to as microfluidic devices. Fluidic behavior at the microscale may differ from that at larger scales in that interfacial tension, viscous effects, and energy dissipation

can dominate the system. A key advantage of microfluidics is the ability to perform experiments and bioassays using miniscule quantities of solution. This provides an economic benefit and is important for certain biosensing applications, experiments requiring single-molecule interrogation (e.g., deoxyribonucleic acid (DNA) sequencing [14, 15], or diffusion-limited regimes. Another benefit is that rapid measurements of these minute quantities can be performed with miniaturized analytical systems [16-18]. In some applications slow or minimal mixing is required, and the laminar flows obtained in microchannels become highly desirable.

Unless special care is taken during preparation, the particle sizes in an emulsion are distributed over a significant range. Such a range may be characterized by a geometric mean and a standard deviation related usually to the diameters of the particles. For ordinary emulsions the size distribution is rarely a normal or Gaussian distribution. Mostly it is a log-normal distribution where the distribution of frequencies of the various sized, plotted against the logarithm of the size is Gaussian. Water-in-oil emulsions can be formed in microfluidic devices to form a steady stream of monodisperse aqueous droplets with volumes as small as picoliters [19]. The drops can be loaded with reactants to perform chemical reactions of interest [20].

1.2.1 Soft Lithography

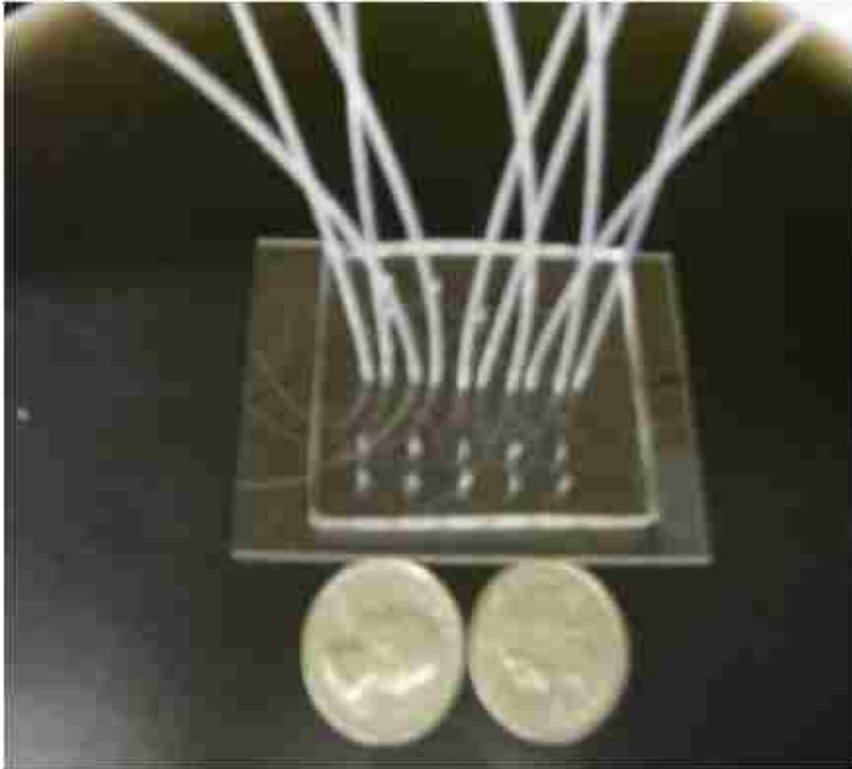


Figure 0.3: PDMS device fabricated using soft lithography. There are 10 devices on the chip.

Various methods have been presented in the literature to fabricate microfluidic devices. One of the most widely used are those made from poly(dimethylsiloxane) (PDMS) gels (figure 1.3) [19, 21, 22]. The materials for these devices are relatively inexpensive and they can be made with established soft lithography processes. This approach has also the potential to form complicated and intricate flow patterns. The soft lithography process is robust and reproducible, which allows replicating flows in different devices that have the same design. The first step in soft lithography is the production of a master mold, which is typically a silicon wafer with epoxy structures. The epoxy structures are created with a high-resolution

transparency as a photomask for generation of the master by photolithography. A negative photoresist is a type of epoxy in which the portion of the photoresist that is exposed to light becomes nearly insoluble to the photoresist developer. The unexposed portion of the photoresist is dissolved by the photoresist developer, leaving behind the desired channel features. Liquid PDMS precursor base along with a curing agent (typically 1:10 ratio) is then poured over the master mold. The liquid PDMS precursor conforms to the shape of the master mold, thus replicating the designed features. Vinyl groups present in the base react with silicon hydride groups in the curing agent to form a clear, cross-linked, elastomeric solid. The PDMS is then peeled away from the master mold; the master mold is not destroyed during the removal process, allowing it to be used again for subsequent devices. The PDMS channels are then sealed to a glass slide by exposing both the PDMS device and the glass slide to oxygen plasma and then pressing both together within 1 min after exposure to the plasma. The disadvantages are that PDMS devices typically can only handle low pressure drops before catastrophic rupture, and untreated PDMS can become swollen or chemically react with some liquids, thus making the channels not reusable. Recently, there have been reports demonstrating that the walls of such channels can be coated with material that can improve the flow properties [22].

1.2.2 Pressure-Driven Microdroplet Formation

Microfluidic channels, as suggested by the name, have dimensions that are in the micrometer range. The typical dimensions of the cross-section range are between a micrometer and a few

hundreds of micrometers. A typical flow rate might be of the order of $\mu\text{L}/\text{minute}$. The small channel dimensions imply that the Reynolds number (Re) will typically be <1 . This results in laminar flow meaning that viscous forces dominate over inertial forces. In such cases, it becomes impossible to stir the fluid by turbulent flow (e.g., shaking). Another practical consideration is the pressure drop across such channels. Because the pressure drop is proportional to the square of the equivalent diameter, we can appreciate the fact that small decreases of channel dimensions can result in large increases in pressure drops—so much that the microchannels can rupture catastrophically. An alternative way to move fluids in microfluidic devices is by using electric fields. Most often this is accomplished by exploiting various electrokinetic phenomena.

The equations of motion for an incompressible Newtonian fluid are:

$$\rho \left(\frac{\partial \mathbf{v}}{\partial t} \right) + \mathbf{v} \nabla \mathbf{v} = \eta \nabla^2 \mathbf{v} - \nabla p, \nabla \cdot \mathbf{v} = 0 \quad (1.3)$$

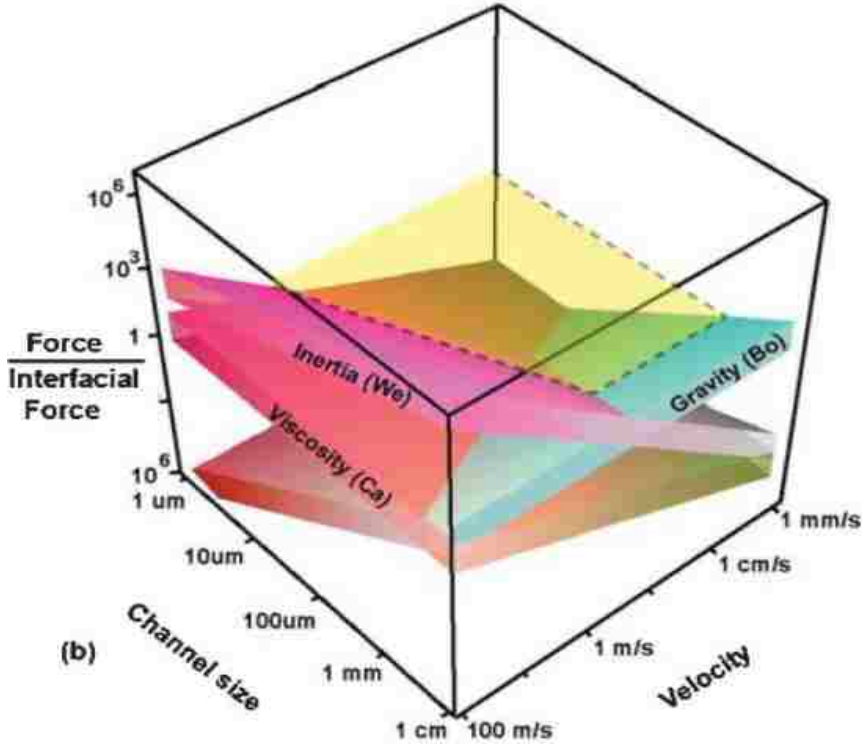


Figure 0.4. In flow regimes with low Re , forces associated with viscous shear flow dominate the system and are on the same order as those associated with interfacial forces. This makes microfluidics ideal for controllable droplet formation [23].

where \mathbf{v} is the velocity field, ρ is the fluid density, p is the pressure, and η is the dynamic viscosity. The relative importance of the acceleration (left side of equation 1.3) and viscous terms (right hand side of equation 1.3) is expressed by the Reynolds number: $Re = \rho U l / \eta$, where U and l are some characteristic velocity and length scale for the system. For viscous-dominated low Re fluid flow the equations of motion are:

$$\eta \nabla^2 \mathbf{v} - \nabla p = 0, \nabla \cdot \mathbf{v} = 0 \quad (1.4)$$

For slit shaped channels, the momentum balance for fluid flow in the z -direction is

$$\eta \frac{\partial^2 \mathbf{v}_z}{\partial y^2} = \frac{\partial p}{\partial z} \quad (1.5)$$

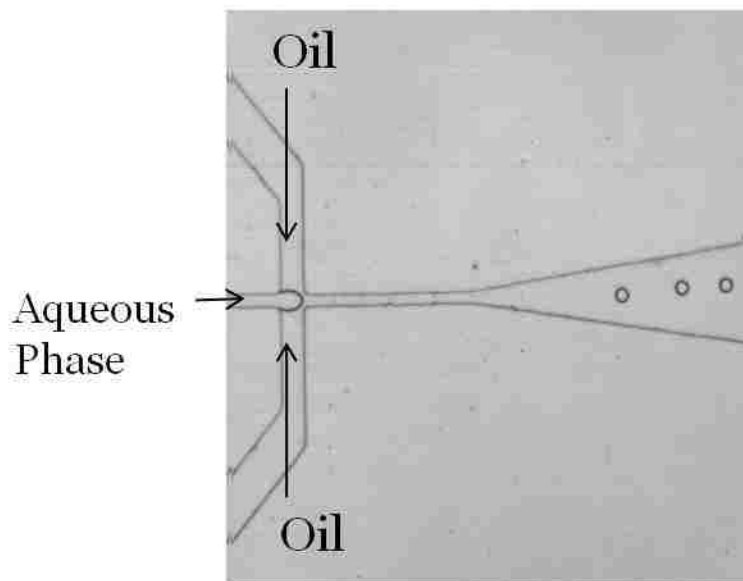


Figure 0.5: Droplet Formation in Microchannels.

Pressure driven viscous flow in microfluidic channels can be utilized to form emulsion droplets. Because of the thermodynamic penalty, emulsion formation typically requires an energy input. In bulk systems, this can most easily be achieved by vigorous stirring or shaking of the whole oil/water/surfactant system. This approach leads to an emulsion with broad droplet size distribution. Microfluidics allows for the minimization of polydispersity and the creation of droplets that are virtually identical in size. At the dimensions and flow rates associated with microfluidic devices, Re are very small, which means that inertia is negligible. Thus, viscous stresses associated with the imposed flow field dominate the system. This makes microfluidics ideal for droplet formation as the forces associated with viscous shear flow are of the same order as those associated with interfacial tension forces

(figure 1.4). In these regimes droplet breakup can be described by Ca which is the ratio of shear stress to capillary stresses due to interfacial tension:

$$Ca = \frac{R_d \tau_{ij}}{2\gamma} \approx \frac{\eta U_d}{\gamma} \quad (1.6)$$

Where R_d is the critical thread radius, η is the continuous phase viscosity, τ_{ij} is the relevant component of the viscous stress tensor, and U_d is the characteristic velocity. At $Ca \sim 1$, the energy input is sufficient enough to hydrodynamically focus the thread to a critical radius which then experiences capillary instability within the enclosed orifice. The necessary viscous stress can be generated by applying pressure or electrically driven flow.

Figure 1.5 shows a microfluidic flow focusing device. A pressure gradient along the long axis of the device forces two immiscible liquids through the orifice. The continuous phase is infused from two sides. The liquid stream comprising the dispersed phase is supplied from the central channel. In what is known as the dripping regime, the continuous phase focuses the inner, immiscible liquid so that the inner thread reaches a critical radius, becoming unstable and breaking in the narrow orifice in a periodic manner. A liquid thread flowing concurrent to a second immiscible fluid in an open channel can also form into droplets via capillary instability, but the droplets formed are not monodisperse [19]. Thus a necessary condition to produce monodisperse droplets is to adjust the flowrates and channel geometries to ensure that capillary stability occurs within the enclosed orifice. In some flow regimes the drop size is effectively set by the size of the orifice. In other cases the flow-focusing geometry produces threads that break into drops substantially smaller than the orifice. Droplets can also be formed further downstream away from the orifice in what is called the

jetting regime; however these droplets are less monodisperse as the mechanism for droplet formation is similar to thread capillary stability in an open channel.

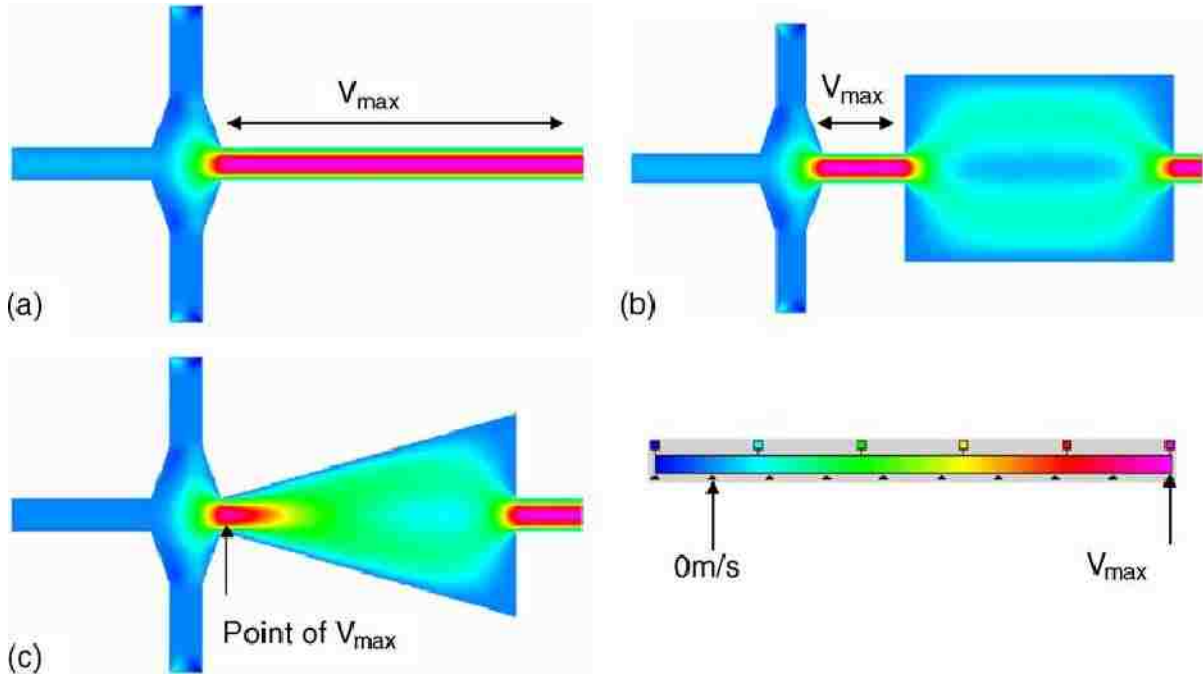


Figure 0.6 CFDRC simulation of velocity distributions in channels with different geometries. (a) Orifice connected to long straight channel. (b) Orifice connected to a short channel with subsequent rectangular expansion. (c) Orifice connected to an expansion nozzle. This design allows the max velocity to occur at the orifice [24].

Channel geometry can be designed to assist in reducing jetting effects and help ensure droplet formation occurs within the orifice in the dripping regime. Figure 1.6 shows three different channel geometries and velocity distributions inside the channel published by Tan and coworkers [24] using a CFDRC ACE single phase flow simulation: a straight channel, a short straight channel leading to an abrupt increase in channel diameter, and expanding channel geometry. Within the two straight channels, the maximum velocity occurs across the whole length of the channel which results in no velocity gradient in the flow direction. In the

expanding nozzle design, fluid velocity increases before entering the nozzle and reaches the maximum velocity at the orifice before decreasing as it exits the orifice. As a result, a high velocity gradient within the orifice of the nozzle is created. In the expanding nozzle geometry, the droplet always forms at the orifice due to designed shear gradient. If the exit from the orifice was into a straight channel as in Fig. 1.6a and b, then due to the constant maximum velocity throughout the length of the channel, the droplet break-off could vary anywhere along inside the parallel channel that may result in jetting and the breakup of polydisperse drops as demonstrated in Anna et al. [19].

Droplet formation can also occur independent of viscous shear stress due to The controlled formation of water-in-oil emulsion droplet stream in a *T*-junction (Figure 1.7) microfluidic system was first demonstrated by Thorsen [25].

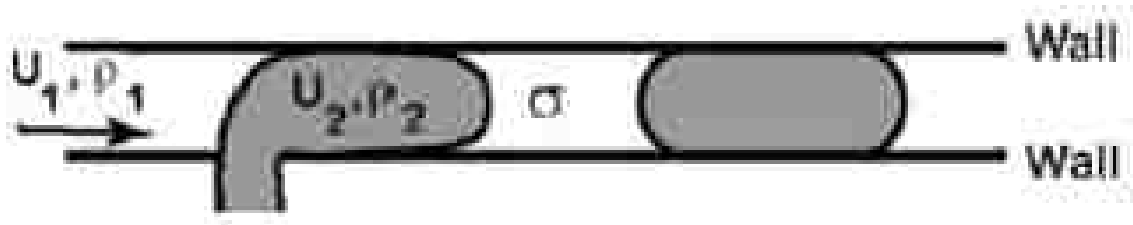


Figure 0.7. Microfluidic T-junction diagram. Droplet formation within T-junction devices is due to a pressure drop across the emerging droplet and independent of shear stress. Image reproduced from [23].

The analysis of the mechanism for droplet formation in a *T*-junction device was proposed by Garstecki et al. [26]. At low capillary numbers, it was demonstrated that breakup of drops or bubbles in a microfluidic *T*-junction is due to the pressure drop across the emerging bubble

or drop and not dependent on shear stress. A similar pressure drop mechanism can also produce droplets within a microfluidic flow focusing geometry if the dispersed phase liquid makes contact with the orifice walls and ‘plugs’ the channel.

1.3 Nanoporous Particles

Materials synthesis based on surfactant self assembly enables a remarkable ability to reproducibly control the structure and composition of porous particles at the nanoscale. The synthesis of mesoporous silicate solids was discovered more than a decade ago and since then there has been extensive research utilizing this technique to synthesize highly ordered mesoporous materials. Particles with well-defined internal mesoporous structure present a special interest. They have application as chemical and biochemical sensors [27-34], catalysts and catalyst templates [35-41], drug delivery vehicles [42-50], biomolecular and cellular encapsulation [51-63], and materials for fuel cell electrodes [64-69]. Developing pathways for fabrication of monodisperse oxide particles with internal mesoporous structure provides additional opportunities and level of complexity of the structural design. Same-size spherical microparticles are essential for developing novel families of functional digital inks for printing catalysts, current collectors, and creating polymer/oxide composites at the microscale [70].

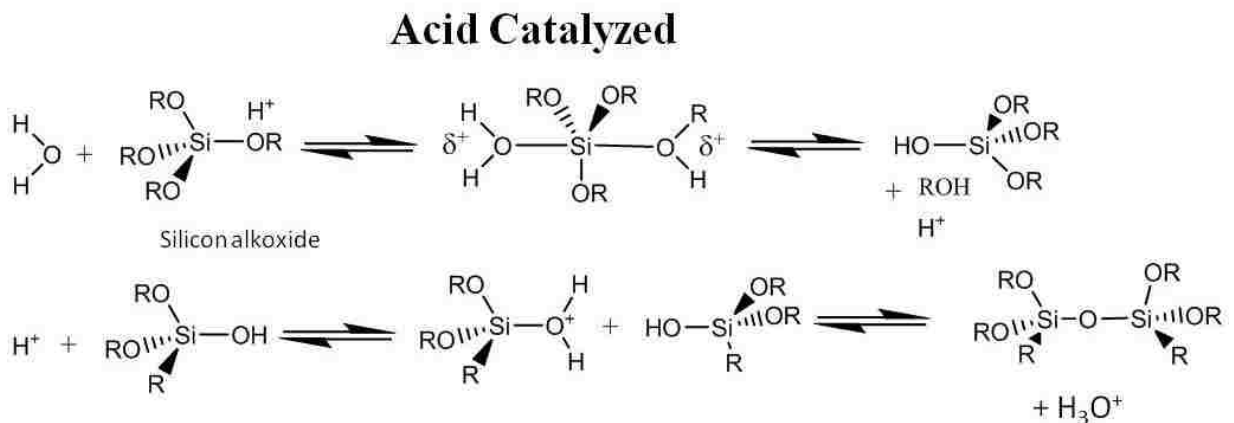
1.3.1 Sol-Gel Processing of Silica

A wide variety of organic/inorganic composite materials have been synthesized via the sol-gel method. It represents an attractive method for formation of various materials, such as

colloidal powders, coatings, membranes, etc. under mild reaction conditions. Metal oxides can be prepared using sol-gel processing of corresponding metal oxide precursors. Silica, alumina, titania, and zirconia are the most common metal oxides prepared due to availability of the alkoxide precursors and the stability of the products.

The sol-gel process can be described by hydrolysis of an alkoxide monomer with concurrent or subsequent condensation reactions. For a silica sol-gel system SiABCD , A, B, C, or D may be OR, OH, or OSi (where R is an alkyl group), and the system can be defined in terms of $\text{Si}(\text{OR})_x(\text{OH})_y(\text{OSi})_z$ where $x + y + z = 4$.

Use of a catalyst dramatically increases the rate of hydrolysis of the alkoxide precursor. For ease of understanding (there are 1365 distinct local silicon environments corresponding to 199,290 forward reaction rate constants [71, 72]) three reactions, either acid or base catalyzed, are used to describe the sol-gel process of silica:



Base Catalyzed

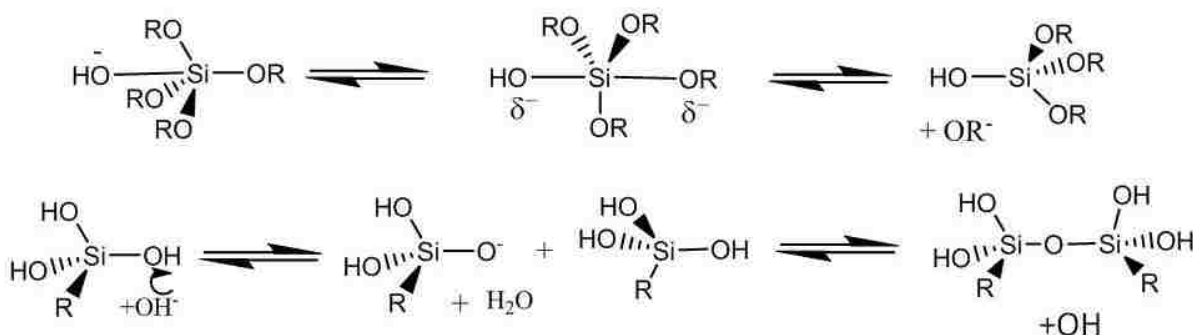


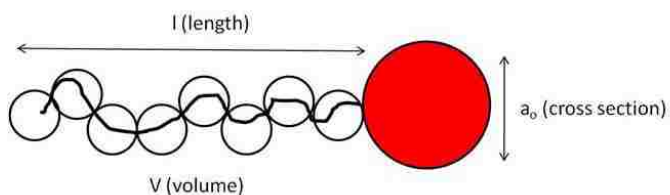
Figure 0.8: Acid and base catalyzed silica sol-gel reactions.

The three forward reactions are hydrolysis, alcohol condensation, and water condensation, respectively. The three reverse reactions are esterification, alcoholysis, and hydrolysis. Under acid conditions, the hydrolysis of the alkoxy silane to the trialkoxy silanol $(RO)_3Si-OH$ is very rapid. Subsequent hydrolysis of this protonated species is less favorable due to the loss of the electron donating alkoxy groups. Condensation reactions involving the trialkoxy silanol monomers produce a linear, homogeneous polymer with cross-linkage occurring during subsequent hydrolysis/condensation reactions. For basic conditions, the hydrolysis of the first alkyl group of the alkoxide monomer is slow, but following this hydrolysis to a trialkoxysilanol, complete hydrolysis of the oxide monomer proceeds very rapidly, to produce fully hydrolyzed monomers. Fully hydrolyzed monomers then undergo condensation reactions to form dense polymeric colloids that are then linked together via subsequent condensation. Thus, base-catalyzed silica is typically less homogeneous than acid-catalyzed silicates, and pores are formed as a result, typically on the order of ~ 2 nm in diameter (called micropores).

1.3.2 Surfactant Self Assembly

Surface active agents, or surfactants, are amphiphilic molecules consisting of hydrophilic and hydrophobic groups. In general, there are three classes of surfactant as described by the ionic nature of the surface active species: anionic, cationic, and non-ionic. As the concentration of a surfactant in a solvent increases, the system has to accommodate more surfactant as efficiently as possible while keeping the surface area of the non-dissolvable block to a minimum. To accommodate this, many systems will form surfactant aggregates known as micelles. In an aqueous solution the amphiphilic molecules in the micelle are arranged with their hydrophilic groups outward and their hydrophobic segments sequestered inside of the aggregate. At very low concentrations the surfactant molecules will exist mostly as unimers, but at a critical concentration, the surfactants will spontaneously aggregate to form micelles. This is known as the critical micelle concentration, or CMC. As the concentration of the surfactant increases, the surfactant may form spherical, cylindrical, or lamellar micelles. Such concentration dependent mesophases are called lyotropic phases.

Isrealachvili et al [73] developed a theory which linked the thermodynamics, interaction of free energies and the surfactant molecular geometry, to explain many of the observed physical properties of various micelle structures. This work described how surfactant molecules assume effective geometries based on molecular structure, concentration, solvent,



Lipid	Critical packing parameter v/a_0l	Critical packing shape	Structure formed
Single chained lipids with large head group areas. SDS in low salt.	$< 1/3$	Cone	Spherical micelles
Single chained lipids with small head group areas. SDS and CTAB in high salt. Anionic lipids.	$1/3 - 1/2$	Truncated cone	Cylindrical micelles
Double chained lipids with large head group areas. Fluid phases: Phosphatidyl choline, phosphatidyl serine, phosphatidyl inositol, phospholipid acids, sphingomyelin, diacylglycerol, diacylglycerol phosphate, dialkyl diacyl phospholipid salts.	$1/2 - 1$	Truncated cone	Flexible bilayers vesicles
Double chained lipids with small head group areas. Anionic lipids in high salt, saturated hydrocarbon chains. Phosphatidyl serine, phospholipid acids, phosphatidyl serine + Ca ²⁺ .		Cylinder	Planar bilayers
Double chained lipids with small head group areas, zwitterionic lipids, poly-fused unsaturated chains, high T onset. Phosphatidyl ethanolamine, diethanolamine + Ca ²⁺ , phosphatidic acid + Ca ²⁺ , cholesterol, MGGG.	> 1	Inverted truncated cone or wedge	Inverted micelles

Figure 0.9. Left: The packing parameter, g . Right: Packing parameter, g , and corresponding aggregate structures.

counter ion presence, and temperature. This effective molecular geometry based upon these constraints, determines the shape of the micelle aggregate formed. The packing of surfactant can be described quantitatively by the packing parameter, g , as shown in figure 1.9 [73]:

$$g = \frac{V}{a_0 l} \tag{1.7}$$

Where V is the total volume of the hydrophobic block, l is the critical hydrophobic chain length, and a_0 is the effective headgroup area per hydrophilic headgroup. The packing parameter is thus the ratio of the effective cross-sectional area of the hydrophobic tail group to that of the hydrophilic headgroup [74]. Based upon the relative sizes of the headgroups

formation of flatter interfaces such as lamellar structures. If $g > 1$, the system will favor the formation of inverse micelles.

Figure 1.10 shows a generic surfactant/detergent phase diagram (water-oil-surfactant) [75]. The oil phase can be a variety of organic, silicone, or fluorocarbon based fluids and the water phase can be a hydrophilic inorganic precursor. Depending on the solution composition, various liquid crystalline structures are formed, such as spherical micelles, cylindrical micelles, hexagonally ordered crystals, cubic crystals, lamellar phases, inverse micelles, and inverse micellar crystals. Because the blocks of the surfactant polymers are covalently bound, macroscopic phase separation is not possible as in multi component polymer systems. Localized phase separation is possible, however, on the length scale associated with the dimensions of the surfactant polymer blocks. If the polymer blocks have a narrow size distribution, the phase separation will produce highly ordered liquid crystalline structures with dimensions in the single nanometers. This provides a powerful method for templating nanostructures via inclusion of a reactive polymeric species in the presence of self-assembled surfactant liquid crystalline structures; not only are these nanostructures highly ordered in nature, but are not random and follow a consistent, repeatable formation pattern.

1.4 Characterization Techniques

A variety of techniques were employed to characterize emulsion polymer precursor liquid phases, the nanostructure of particles synthesized in emulsion systems, and fluorescence detection for DNA sequencing. Characterization techniques include dynamic light scattering

(DLS), tensiometers, scanning electron microscopy (SEM), transmission electron microscopy (TEM), nitrogen adsorption and desorption isotherms for estimating pore size distributions and surface areas and X-ray diffraction (XRD).

1.4.1 Dynamic Light Scattering

When a coherent source of light (such as a laser) having a known frequency is directed at moving particles, the light is scattered. The scattered light has a different frequency than the incident light, whose shift is governed by the Doppler Effect. Smaller particles, with a higher average velocity than larger particles, will cause a greater shift in light frequency. The particle size is determined by the analysis of the power spectrum, which is a function of angular frequencies of the detector signal [76]:

$$S^{(i)}(q, \omega) = \int_{-\infty}^{\infty} g^1(q, \tau) \exp(j\omega\tau) d\tau \quad (1.8)$$

where ω is the angular frequency shift of the scattered light, τ is the averaged time, and g^1 is the auto correlation function:

$$g^1(q, \tau) = \exp(-q^2 D\tau) \quad (1.9)$$

with propagation vector length q :

$$q = (4\pi / \lambda) \sin(\theta / 2), \quad (1.10)$$

where λ is the wavelength of light in the medium, and θ is the scattering angle, all of which are known experimentally. Thus, the Stokes-Einstein coefficient in equation 1.9, D , can be determined to estimate particle size:

$$D = \frac{kT}{6\pi\eta r} \quad (1.11)$$

where k is the Boltzmann constant, T is temperature, η is fluid viscosity, and r is the particle radius. All Dynamic Light Scattering (DLS) measurements were conducting using heterodyne scattering via the instrument Nanotracer by Microtrac, Inc.

1.4.2 Interfacial Tension Measurements

Perhaps the most important concept of all when considering interfaces in which two immiscible liquids are in contact is that of surface or interfacial tension. Interfacial tension and the effects which arise as a consequence, play a major role in the behavior of systems with an interface. Surface tension is caused by the attraction between the liquid's molecules by various intermolecular forces. In the bulk of the liquid, each molecule is pulled equally in all directions by neighboring liquid molecules, resulting in a net force of zero. At the surface of the liquid, the molecules are pulled inwards by other molecules deeper inside the liquid and are not attracted as intensely by the molecules in the neighboring medium (be it vacuum, air or another liquid). Therefore, all of the molecules at the surface are subject to an inward force of molecular attraction which is balanced only by the liquid's resistance to

compression, meaning there is no net inward force. However, there is a driving force to diminish the surface area, and in this respect a liquid surface resembles a stretched elastic membrane. Thus the liquid squeezes itself together until it has the locally lowest surface area possible. Interfacial tension represents excess surface energy which is proportional to the area and is a driving force for various interfacial phenomena.

Possibly the easiest method for measuring the force arising from interfacial tension is to dip a flat plate through the surface of a liquid and use a balance to measure the downward force acting on it. This is known as a Wilhelmy plate. Along the contact line the liquid surface will be vertical so the interfacial tension along this line will exert a downward force on the plate, which is simply the interfacial tension multiplied by the wetted perimeter:

$$\gamma = \frac{F - F_B}{2(x + y) \cos \theta} \quad (1.12)$$

where F_B is the buoyancy force acting on the submerged plate and x and y are the horizontal length and width of the plate, respectively. The plate is typically made of a perfectly wetting material such as platinum to give a 0° contact angle.

The Du Nouy ring method is used to measure static surface and interfacial tensions of liquids. The apparatus required to carry out these measurements consists of a vessel containing the liquids to be analyzed and a metal ring (typically platinum) which is attached to a sensitive balance to measure the force. The vessel can be moved upward and downward in a precise, controlled manner while the position of the ring is kept constant. For the ‘pull method,’ the vessel is first positioned so that the ring is just below the surface of the highest

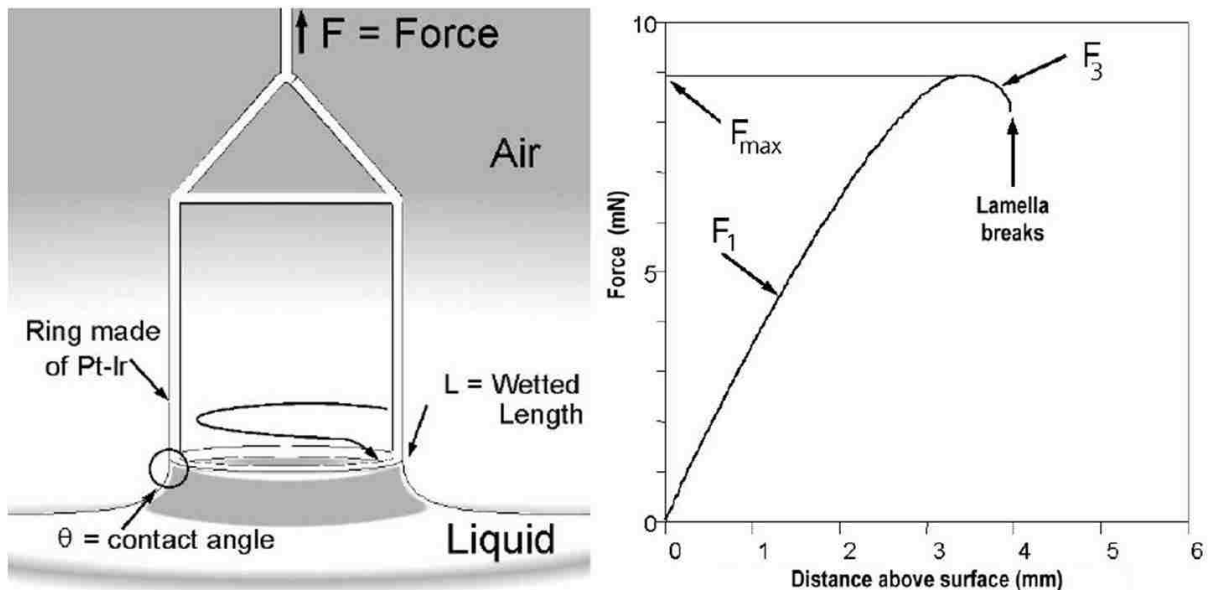


Figure 0.11. Left: Diagram of Du Nouy ring. Right: Force versus displacement for the ring. The maximum force, F_3 is used to estimate surface or interfacial tension.

density liquid. The vessel is then lowered slowly while the force exerted on the ring is recorded. As the film is stretched a maximum force is experienced, this is recorded in the measurement. At the maximum the force vector is exactly parallel to the direction of motion and at this moment the contact angle is 0° (see Figure 1.11). The distance is first increased until the area of maximum force has been passed through. The sample vessel containing the liquid is then moved back to that the maximum point is passed through a second time. The maximum force is determined exactly on this second return and is used to calculate the interfacial tension. This method is chosen over a detachment method where the force measurement is taken at the time of film rupture as there are fewer problems associated with

the kinetics of surfactant adsorption during the detachment process. The calculation is made via the following equation:

$$\gamma = \frac{F_{\max} - F_v}{L \bullet \cos \theta} \quad (1.13)$$

Where F_{\max} is the maximum force, F_v is the weight of volume of liquid lifted, and L is the wetted perimeter. A correction factor usually is used for tension measurements made with the ring. The weight of the volume of liquid lifted beneath the ring must be subtracted from the total force. An additional complication arises from the difference in curvature between the inside and outside of the ring. Harkins and Jordan have drawn up tables of correction values by determining different surface tensions with different diameter rings. The software utilizes this correction factor, which has been shown to offer excellent accuracy.

1.4.3 Scanning Electron Microscopy

The scanning electron microscope (SEM) is a powerful tool which facilitates the observation and characterization of heterogeneous organic and inorganic materials and surfaces on the micron and sub-micron length scales. The SEM uses a focused beam of high-energy electrons to generate a variety of signals at the surface of solid specimens. The signals that derive from electron-sample interactions reveal information about the sample including external morphology (texture), chemical composition, and crystalline structure and orientation of materials making up the sample. In most applications, data are collected over a selected area of the surface of the sample, and a 2-dimensional image is generated that

displays spatial variations in these properties. Areas ranging from approximately 1 cm to 5 microns in width can be imaged in a scanning mode using conventional SEM techniques (magnification ranging from 20X to approximately 30,000X, spatial resolution of 50 to 100 nm). The SEM is also capable of performing analyses of selected point locations on the sample; this approach is especially useful in qualitatively or semi-quantitatively determining chemical compositions (using energy dispersive X-ray spectroscopy (EDS)), crystalline structure and crystal orientations (using electron back scatter detection (EBSD)).

Accelerated electrons in an SEM carry significant amounts of kinetic energy, and this energy is dissipated as a variety of signals produced by electron-sample interactions when the incident electrons are decelerated in the solid sample. These signals include secondary electrons (that produce SEM images), backscattered electrons (BSE), diffracted backscattered electrons (EBSD that are used to determine crystal structures and orientations of minerals), photons (characteristic X-rays that are used for elemental analysis and continuum X-rays), visible light (cathodoluminescence--CL), and heat. Secondary electrons and backscattered electrons are commonly used for imaging samples: secondary electrons are most valuable for showing morphology and topography on samples and backscattered electrons are most valuable for illustrating contrasts in composition in multiphase samples (i.e. for rapid phase discrimination). X-ray generation is produced by inelastic collisions of the incident electrons with electrons in discrete orbitals (shells) of atoms in the sample. As the excited electrons return to lower energy states, they yield X-rays that are of a fixed wavelength (that is related to the difference in energy levels of electrons in different shells for a given element). Thus, characteristic X-rays are produced for each element in a mineral

that is "excited" by the electron beam. SEM analysis is considered to be "non-destructive"; that is, x-rays generated by electron interactions do not lead to volume loss of the sample, so it is possible to analyze the same materials repeatedly. In obtaining images of a given sample, depth of penetration into the sample, contrast, and clarity of image can be controlled by varying voltage, current, and stigmatic adjustments, respectively.

1.4.4. Transmission Electron Microscopy

Transmission electron microscopy (TEM) is a powerful instrument in characterizing nanostructures because of its amazingly high spatial resolution. A TEM can be simplified into a single lens microscope, as depicted in figure 1.12. The resolution of the TEM is mainly determined by the objective lens, allowing for this simplification to be made. A parallel or nearly-parallel electron beam illuminates the surface of a thin foil sample. The electron beam is diffracted by the lattices of a crystal, forming Bragg-like beams that propagate in all

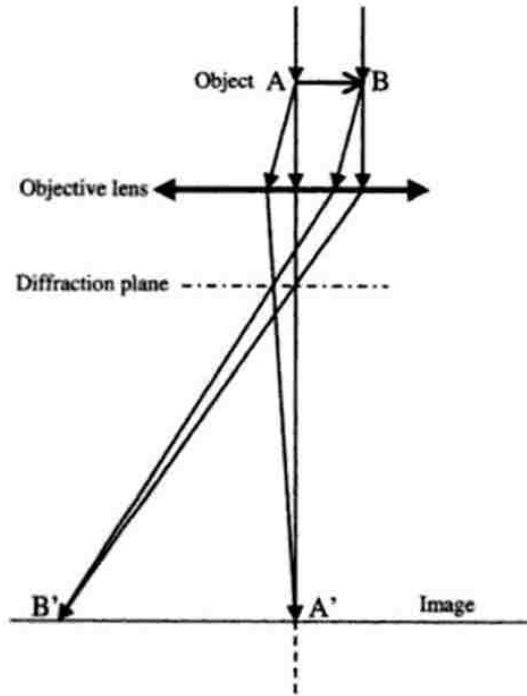


Figure 0.12. Single lens configuration of a TEM.

directions. Due to its interaction with the sample, the phase and the amplitude of the electron wave changes. These changes are determined by quantum mechanical diffraction theory.

Under conditions of sufficiently thin sample and high-energy electrons, the transmitted wave function at the exit of the specimen can be assumed to be composed of a forward-scattered wave. Under these ideal conditions, the exit wave contains the full structural information of the sample.

1.4.5 X-Ray Diffraction

X-rays can be used in chemical and physical analysis in several different ways. X-ray diffraction (XRD) involves diffraction of X-rays from the planes of a crystal or crystal-like

structure. X-ray diffraction is a versatile, non-destructive technique for identification and quantitative determination of the various crystalline phase present in a solid material sample.

When an X-ray beam is incident upon a crystal-like structure below a certain size limit, it is scattered in every direction by every atom or component of the crystal structure. Only highly ordered structures will lead to constructive interference of the incident beam. The condition for constructive interference is given by the Bragg equation:

$$n\lambda = 2d\sin\theta , \quad (1.14)$$

where: λ is the wavelength of the incident X-ray beam.

d is the distance between each set of planes in the crystal structure lattice.

θ is the glancing angle of the beam.

Atoms or nanostructures located on exactly the crystal planes contribute maximally to the intensity of the diffracted beams. Atoms or nanostructures exactly halfway between the planes exerts maximum destructive interference, and those at some intermediate location interfere either constructively or destructively as a function of their location, but with less than their maximum effect. Additionally, the scattering power of an atom for X-rays depends on the number of electrons it possesses. Therefore, the position of the diffraction beams from a crystal depends upon only the size and shape of the repetitive crystal unit and λ of the X-ray beam used, whereas the intensity of the diffracted beams depend also upon the type of atoms in the crystal and the density of the atoms in particular locations in the unit cell. Thus, no two crystalline substances have identical diffraction patterns when considering both the pattern and intensity of the diffracted beams.

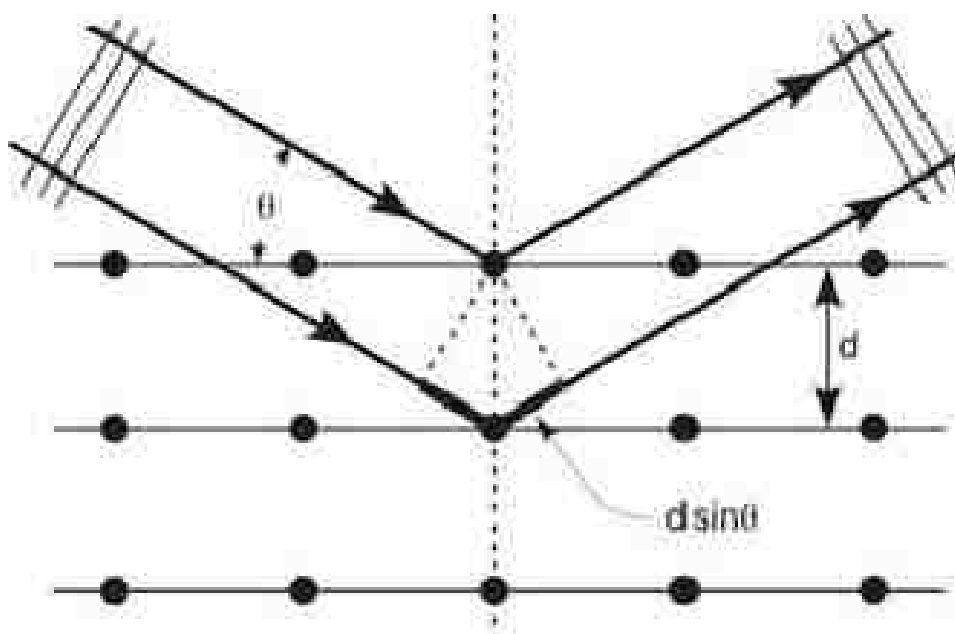


Figure 0.13. Diffraction of X-rays from sets of crystal planes.

Figure 1.13 shows a diagram illustrating the principle of X-ray diffraction analysis. The diffraction pattern is thus a ‘fingerprint’ of a crystalline compound and the crystalline components of a mixture can be identified individually. If the X-ray beam is monochromatic, there will only be a discrete and limited number of angles at which constructive diffraction of the beam can occur. The actual angles are determined by the wavelength of the incident beam, and the spacing of the planes of the crystal or crystal-like structures.

If the amount of powder sample is sufficient, X-ray diffraction is the first choice to examine the extent of periodicity in ordered nanoporous materials. As observed in the Bragg equation, ordering in the range of inter-atomic distances will produce diffraction spectrum obtained at the high-angle range. The diffraction spectrum at lower angle region ($2\theta < 10$) reflects ordering at distances larger than inter-atomic distances and is most suitable to provide

information about the periodicity of materials based on self assembly of surfactant micelle structures (> 2 nm).

For mesoporous materials, a 2-D hexagonal mesostructure (P6mm) consist of cylinders of self-assembled amphiphilic molecules arranged in a hexagonal morphology. The peaks are arranged in d-spacing ratios of $1 : \sqrt{3} : 2$. In the case of body centered cubic (Im3m), spherical micelles are arranged with d-spacing ratios of $1 : \sqrt{2}$.

1.4.6 Nitrogen Sorption Analysis

A solid surface in contact with a gas usually attracts an adsorbed layer of gas molecules. The term adsorption connotes the condensation of gases on free surfaces, in contradiction to absorption where the molecules of gas penetrate into the mass of the absorbing solid. Even a non-polar and non-reactive gas like nitrogen will adsorb to a solid surface under certain conditions. An important use of gas adsorption is the characterization of porous materials, where information about the surface area and pore size distribution can be gained from measurements of the adsorption as a function of temperature and pressure [77] [78]. The adsorption of a gas (the adsorbate) on a solid surface (the adsorbent) involves only physical interactions in a process known as physical adsorption, and does not involve a chemical reaction between the gas and solid. The physical adsorption of gas molecules is driven by van der Waals-London forces. These forces are represented by the a/V^2 term in the van der Waals equation:

$$(P + a/V^2)(V - b) = RT \quad (1.15)$$

where: b is the volume occupied by the gas molecules.

a/V^2 is the correction for the attraction forces between the gas molecules.

a is a constant characteristic for each gas.

The results of an adsorption measurement are usually plotted as an adsorption isotherm: the amount of gas adsorbed as a function of the equilibrium gas pressure.

If the adsorption of a gas is measured at a temperature well above the condensation temperature of that gas, only a monolayer will be adsorbed, i.e., second or additional layers will not build onto the first one. The total surface area can be calculated by measuring the maximum amount of gas adsorbed as follows :

Total surface area = (number of adsorbed gas molecules) x (area per molecule)

Langmuir used the following assumptions in deriving the isotherm describing monolayer adsorption:

- the surface of the adsorbent is flat
- all adsorption sites are energetically equivalent
- the adsorbed gas molecules do not mutually interact
- the adsorbed molecules have a fixed position on the surface

However, in practice these assumptions are seldom valid; surfaces are rarely flat and adsorption sites are not energetically equivalent. Additionally, the adsorbed gas molecules do

have mutual interactions, especially at higher surface coverages, and are highly mobile.

Neglecting surface heterogeneity introduces deviations at relative pressures below $p/p^0 < 0.5$ and neglecting mutual interactions between the adsorbed gas molecules causes serious mismatches at higher pressures i.e. $p/p^0 > 0.35$.

Brunauer, Emmett, and Teller introduced a number of simplifying assumptions extended to the Langmuir model to account for multi-layer adsorption to obtain an isotherm equation for estimating pore surface area (the BET surface area equation). They assumed that the adsorption forces are short range forces, i.e. the heat of adsorption of the first layer is higher than that of following layers. In the layers above the solid-gas monolayer, the heat of adsorption is estimated to be equal to the latent heat of condensation of the adsorbed gas. The BET equation is:

$$\frac{1}{v[(P_o / P) - 1]} = \frac{c - 1}{v_m c} \left(\frac{P}{P_o} \right) + \frac{1}{v_m c} \quad (1.16)$$

Where: v is the volume of the gas adsorbed (at standard temperature and pressure (STP)).

V_m is the volume of gas adsorbed at the monolayer

p/p^0 is the relative pressure of the gas

and the thermodynamic constant c accounts for the relative strength of heat of adsorption of the first layer and the heat of condensation of the gas:

$$c = \exp\left(\frac{Q - L}{R}\right) \quad (1.17)$$

where Q is the heat of adsorption of the first layer and L is the latent heat of condensation of the gas. The amount of gas adsorbed, n^a per mass of solid, m^s , depends on the equilibrium pressure p , the temperature, T , and the nature of the gas-solid system. Thus:

$$n^a / m^s = f(p, T, \text{system}) \quad (1.18)$$

For adsorption of a given gas on a particular solid at constant temperature, we have

$$n^a / m^s = f(p)_T \quad (1.19)$$

If the system is below the critical temperature of the gas, then

$$n^a / m^s = f(p / p^\circ)_T \quad (1.20)$$

where the standard pressure p° is equal to the saturation pressure of the adsorptive at system T . The above equation represents the adsorption isotherm, i.e. the plot of amount of gas adsorbed by unit mass of solid at equilibrium as a function of partial pressure at a constant temperature, usually nitrogen at its boiling point (77.4 K).

The isotherms are generally grouped in 6 classes, denoted as type I to type VI. Mesoporous materials generally lead to adsorption isotherms of type IV. These isotherms exhibit a hysteresis loop, the lower branch of which represents measurements obtained by progressive addition of the adsorbent, and the upper branch by progressive withdrawal. The hysteresis loop is usually associated with the filling and emptying of cylindrical or spherical pores due to capillary effects. The shape of the hysteresis loop varies from one system to another.

Simple condensation occurs when the actual vapor pressure exceeds the equilibrium vapor pressure. If the surface is curved, the Kelvin equation shows that this latter pressure may be significantly lower than p^o . The Kelvin equation:

$$\ln \frac{P}{P^o} = \frac{-2\gamma V_m}{rRT} \quad (1.21)$$

describes the change in vapor pressure for a curved surface of radius r , where γ is the surface tension, V_m is the molar volume, R is the gas constant, and T is the temperature. Barrett, Joyner, and Halenda modified the Kelvin equation to account for multilayer adsorption. The BJH equation is:

$$RT \ln \left(\frac{p}{p^o} \right) = \frac{\gamma v}{r - t_c} \quad (1.22)$$

where t_c is the critical thickness of the adsorbate when capillary condensation will occur.

The BJH method assumes:

- rigid pores of cylindrical shape
- hemispherical meniscus with zero contact angle
- applicability of simple Kelvin equation
- validity of the correction for multilayer adsorption.

These assumptions limit the BJH method to specific pore estimates, i.e. those which are cylindrical with a hemispherical meniscus. Thus, the BJH method is not ideal for estimates of pore size distributions of multimodal porous materials with different pore morphologies.

Pore size distribution estimates using a non-localized density functional theory, or NLDTF, allows the calculation of theoretical adsorption–desorption isotherms in pores of given shape. Moreover, the PSDF of model porous materials constituted, for instance, of cylindrical capillaries or spherical pores, can be approximated from the deconvolution of the generalized adsorption equation, which assumes the experimental isotherm to be a weighted sum of the theoretical isotherms in pores of different diameters.

$$N_{\text{exp}}(p/p_o) = \int_{D_{\text{min}}}^{D_{\text{max}}} N_S(D, p/p_o) \varphi_S(D) dD \quad (1.23)$$

Here $N_{\text{exp}}(p/p_o)$ represents the measured experimental isotherm, $N_S(D, p/p_o)$ corresponds to individual theoretical isotherms in pores of diameter D , and $\varphi_S(D)$ is the pore size distribution to be determined. The resolution algorithm of eqn. (7) allows us to obtain the best set of pore sizes of a given shape that better fits the experimental data, especially for materials with a hierarchical pore size distribution.

1.5 Research Goals

The engineering of nanostructured and polymeric particles utilizing micron-size emulsion droplet reactors is a generally less-explored area in material science, thus creating opportunities for the discovery and design of novel materials and synthesis pathways. The goal of this dissertation research is to exploit chemical environments and interfacial phenomenon unique to two liquid phase emulsion systems for the engineering of novel materials. The specific dissertation research goals are as follows:

- Develop novel materials and methods by executing polymerization chemistries within emulsion droplet reactors.
- Utilize unique physical and chemical properties of emulsions and interfaces for engineering of nanostructured materials.
- Merge complex emulsion polymerization systems with droplet-based microfluidic techniques to synthesize monodisperse particles with complex nanostructure.

The material research presented herein, with differing and unique synthesis pathways, is confined within the previously defined domain of emulsion polymerization.

Monodisperse Particle Synthesis in Microfluidic Droplet Reactors

2.1 Synthesis of Monodisperse Polyurethane Latex Microspheres

Suspension polymerization is an industrially important method that yields particles with sizes ranging from less than a micron to tens of microns[79, 80]. Unlike emulsion and dispersion polymerization it affords complete freedom of composition: a polymer precursor is emulsified into droplets that are then converted with a 1:1 stoichiometric ratio to solid polymer particles. Suspension polymerization relies on both the phase separation of the precursor from the continuous emulsion phase, as well as its chemical compatibility with the continuous phase. In conventional emulsion systems the continuous phase consists either of water or of lipophilic oils. Most polymers are made from hydrophobic precursors that can be emulsified in water only. This, however, restricts suspension polymerization to reactions that are not water sensitive. Therefore, to date it has not been applied to polyurethanes (PU). PU dispersions are used for coatings as they afford outstanding mechanical properties[81]. For example in leather finishing they afford at the same time improved hardness and elasticity resulting in greater abrasion resistance and a softer feel than acrylic dispersions[82].

Polyurethane synthesis involves water-sensitive diisocyanate precursors[83]. Isocyanates can react with alcohols (Fig. 2.1, right) to yield urethanes or with amines to yield ureas (Fig. 2.1, left). The side-reaction of isocyanates with water is very fast and yields primary amines that can react with another isocyanate to yield a urea (Fig. 2.1, middle). This side reaction is not desired as it can offset the stoichiometric ratio of reagents, limiting the maximum obtainable

molecular weight of the polymer. Müller and coworkers successfully used a catalyzed nonaqueous emulsion polyaddition/precipitation process for the fabrication of

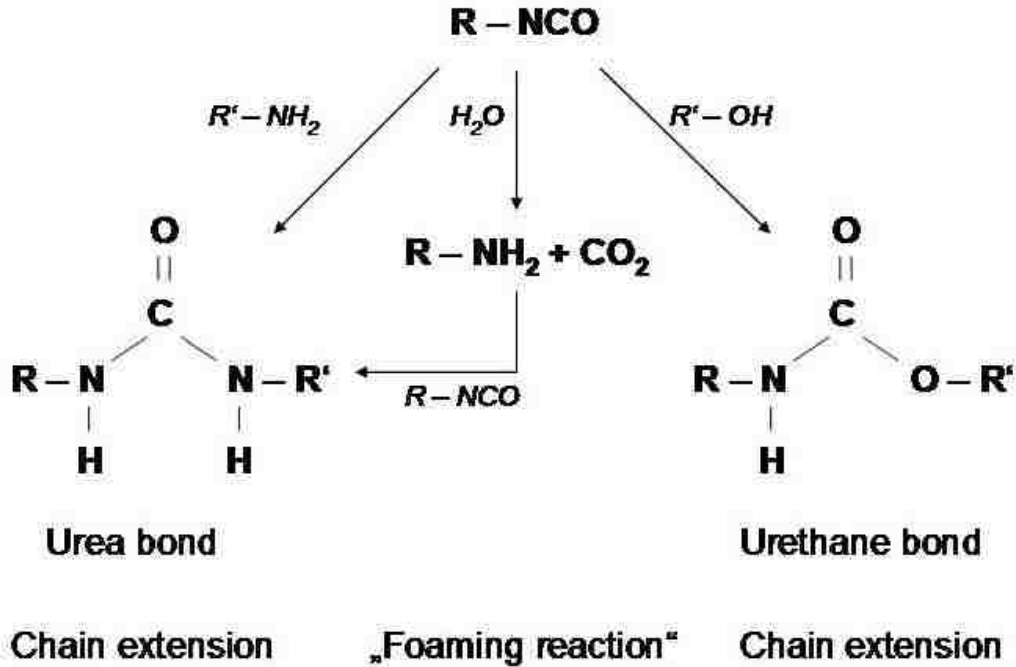


Figure 0.1: Isocyanates can react to form urethanes, if the stoichiometry of isocyanates to alcohol is 1:1. However, they react much more rapidly with water forming an amine that then reacts with another isocyanate to form a urea bond.

spherical polyurethane nanoparticles[84]. Dispersions of PU-particles (latexes) are produced on large scales through emulsification of a prepolymer or polymer solution [85]. Typical prepolymers contain carboxylic groups for stabilizing the aqueous dispersion against coalescence and residual isocyanate groups that can be used for chain extension[86, 87], while crosslinking can be achieved by reaction with multifunctional amines. In a last step, the solvent used to disperse the prepolymer must be stripped. This process is more complicated, time consuming, expensive and less versatile and environmentally friendly than solvent-free

suspension polymerization which affords the same product in a single processing step. In addition, prepolymers to be applied must have a sufficiently low water solubility to suppress the side reaction with water. Such restrictions do not apply when choosing perfluorinated oils as the continuous emulsion phase for PU suspension polymerization: they phase separate from the hydrocarbon-based PU precursors, while still being water-free. However, to date, there is no commercially-available surfactant that provides the requisite stability of the emulsion droplets against coalescence for the duration of suspension polymerization.

This work describes the development of a novel class of fluorosurfactants that stabilizes organic-in-fluorocarbon emulsions and its application for the suspension polymerization of polyurethanes. We demonstrate the versatility of this approach by synthesis of PU particles of uniform size through emulsification in microfluidic channels, by labeling them fluorescently, by synthesizing cross-linked particles, and by controlling the mesh size of the cross-linked network.

2.1.1 Methods

Surfactants for the colloidal stabilization of emulsion droplets are molecules comprised of two moieties: one that is soluble in the continuous phase and one that is soluble in the dispersed phase. Good steric droplet stabilization in a fluorocarbon oil relies on a sufficiently large perfluoro-block, such as a perfluorinated polyether (PFPE). The adsorption of the surfactant to a droplet interface relies on a block that is soluble in the dispersed phase.

Polyethylene glycol (PEG) is well suited for this purpose, as it is soluble in most common organic solvents. A straightforward way of synthesizing a fluorosurfactant is by coupling a

PFPE and a PEG-molecule. A simple method for linking these blocks is an amidation reaction, which yields a stable block-copolymer surfactant.

In addition to the appropriate choice of blocks, good emulsion stability relies on a densely packed surfactant layer. This in turn relies on the proper surfactant molecular geometry and hence on the block length ratio. A surfactant that works well with microfluidic emulsification techniques and stabilizes the polyurethane precursor emulsions for a sufficient time for

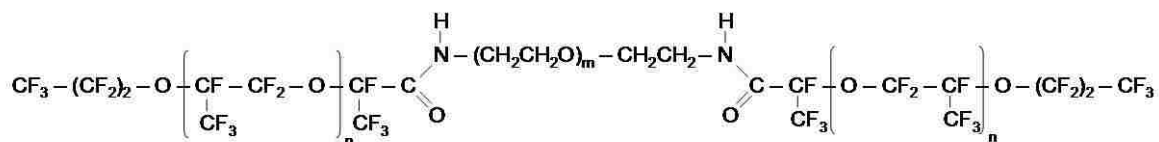


Figure 0.2: Krytox-b-PEG-b-Krytox triblock copolymers were coupled by an amide bond. These amphiphilic molecules stabilize organic-in-fluorocarbon emulsions.

polymerization is a block copolymer; we find that a suitable size consists of 400 g/mol PEG and 1890 g/mol PFPE moieties that are covalently linked by an amide bond, as shown schematically in Fig. 2.2.

The effective geometry of the fluorosurfactant can be tuned by adjusting the relative chain length of the block polymers and the number of blocks linked (figure 2.3).

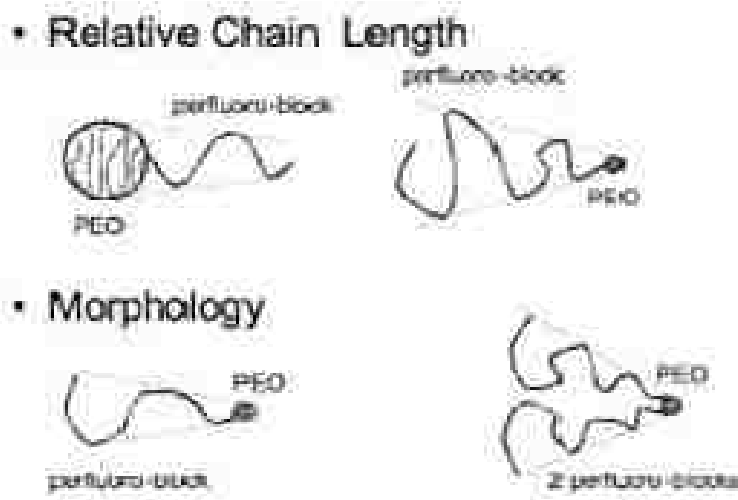


Figure 0.3. The geometry of the surfactant can be tuned by adjusting relative chain length of the perfluoro- or PEG blocks (top) or the number of blocks coupled (bottom).

The stability of a fluorocarbon continuous phase emulsion system is easily determined by observation of the liquid after emulsification. A stable emulsion will have a uniform, opaque appearance, while an unstable emulsion will not be uniformly opaque and will instead contain regions where droplet coalescence or phase separation is observed. As was discussed earlier in the introduction section, the oriented wedge theory of Harkins arises from the insight that the emulsifier forms an oriented monolayer at the oil-water interface and suggests that the end of the emulsifier molecule with the loosely defined ‘larger size’ will lie in the continuous phase. Thus if the PEG water soluble block is too ‘large,’ a water in fluorocarbon oil emulsion will not be stable as displayed in figure 2.4.

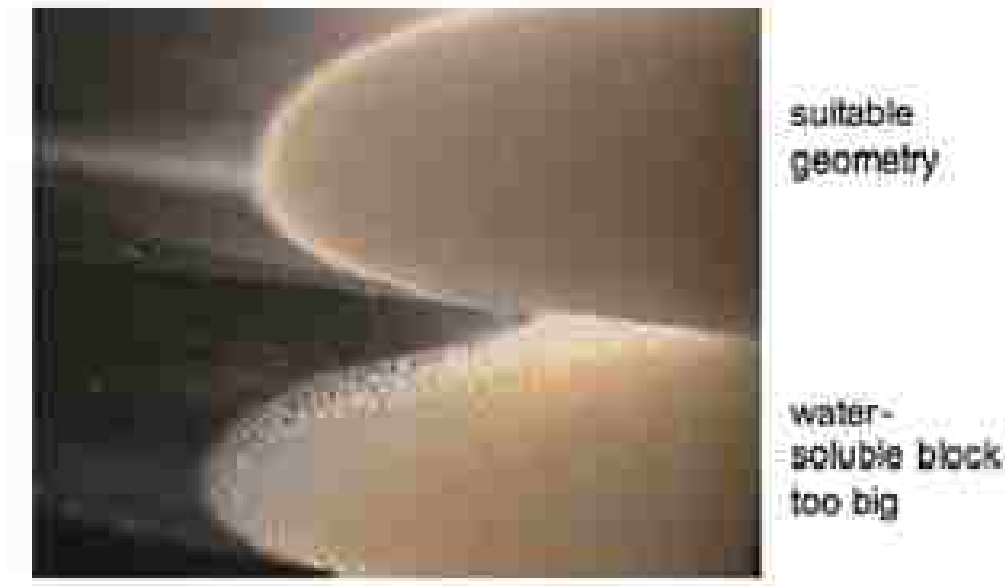


Figure 0.4. (Top) A stable emulsion will have a uniform, opaque appearance, while an unstable emulsion (Bottom) will not be uniformly opaque and will instead contain regions where droplet coalescence or phase separation is observed.

Emulsification of a polyurethane precursor yields separate droplets with the same chemical composition as that of the precursor liquid. Crude emulsions can be obtained by simply shaking the precursor and fluorocarbon oil in the presence of the fluorosurfactant; this yields a polydisperse precursor emulsion. Emulsions with precise control over the droplet size can be obtained with a microfluidic device, using hydrodynamic flow focusing [10, 11].

Microfluidic-generated drops can function as both morphological templates and chemical reactors for the synthesis of monodisperse polymer [12-15] and biopolymer [16] particles.

For rapid prototyping of such devices, we use soft lithography employing polydimethylsiloxane (PDMS) [17]. Monodisperse emulsion droplets are formed when co-flowing streams of the continuous and precursor phases are forced into a single output channel, viscous shear overcomes interfacial tension causing the dispersed stream to become

unstable within the orifice and break into discrete droplets. A surfactant dissolved in the continuous phase will adsorb onto the newly formed interfaces of the droplets, stabilizing them against coalescence. This stability is essential to allow polymerization to take place.

We use polyurethane precursor solutions consisting of dialcohols and diisocyanates that react in a polyaddition reaction to form urethane bonds. Following step kinetics, high molecular weights may be obtained only at high conversions and when the ratio of the reagents is exactly stoichiometric. Stoichiometry can only be ensured in a dry system, given that isocyanates undergo a vigorous degradation reaction with water.

As a proof of principle, we synthesize polyurethanes from an equimolar ratio of polyethylene glycol (PEG, a dialcohol) with hexanediisocyanate. It would not be possible to emulsify this particular system in water or in lipophilic oil as in either case is there sufficient miscibility to preclude phase separation. The resulting rubbery polymer resembles the soft blocks of Spandex. At high degrees of polymerization the liquid precursor becomes solid. Therefore, the mechanical properties of the product may be used as a measure of conversion.

2.1.2 Results/Discussion

Fluorocarbon-based emulsions have not been considered for suspension polymerization of polyurethanes in the past due to the lack of suitable surfactants. The simplest way to confirm a high degree of polymerization leading to solid particles is to remove the continuous fluorocarbon phase through evaporation. Only solid particles have the mechanical rigidity to resist coalescence and retain their spherical shape in spite of capillary forces. We tested this with a crude polydisperse precursor emulsion obtained by shaking; upon drying, it displays

patches of both coalesced droplets and of solid particles, as shown in the micrograph in Fig. 2.5, left). An additional

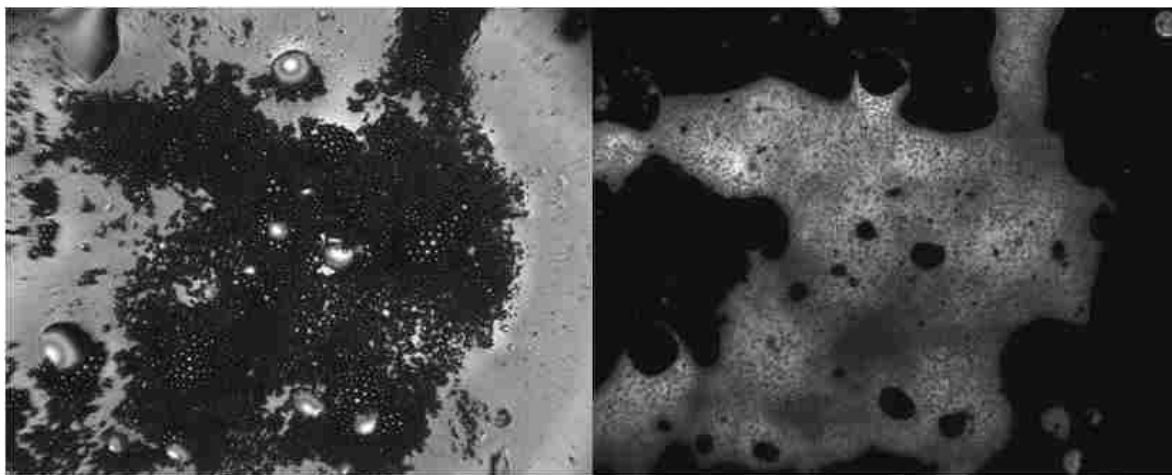


Figure 0.5: . Micrographs of Fluorescein-labelled polyurethane particles obtained through suspension polymerization. Left: brightfield. Right: cross-polarization. Stable, polydisperse emulsions were obtained from shaking the precursor and the fluorocarbon oil in the presence of non-ionic fluorosurfactants. Drying a partially converted emulsion on a glass slide is a simple way to confirm conversion: Particles with low conversion coalesce, whereas fully converted particles remain stable. Low conversion is also indicated by the lack of fluorescence – unreacted isocyanates quench fluorescein, which acts as a probe for conversion.

probe for conversion is the presence of fluorescein, a fluorescent dye added to the reaction mixture prior to emulsification. We observed that fluorescein is quenched in the presence of isocyanates and does not fluoresce. Fluorescence reappears, however, as the isocyanate is consumed during the course of the reaction. Cross-polarization microscopy (Figure 2.5, right)) confirms the low conversion of the coalesced patches by the absence of fluorescence, whereas the un-coalesced particles do exhibit fluorescence. The presence of solid particles indicates that the fluorosurfactants are suitable for stabilizing polyurethane precursor emulsions in fluorocarbon oils. Moreover, it demonstrates the benefits of this water-free

emulsion system: by maintaining an exactly stoichiometric ratio of water-sensitive isocyanate and alcohol moieties, thereby meeting the requirements for high conversion.

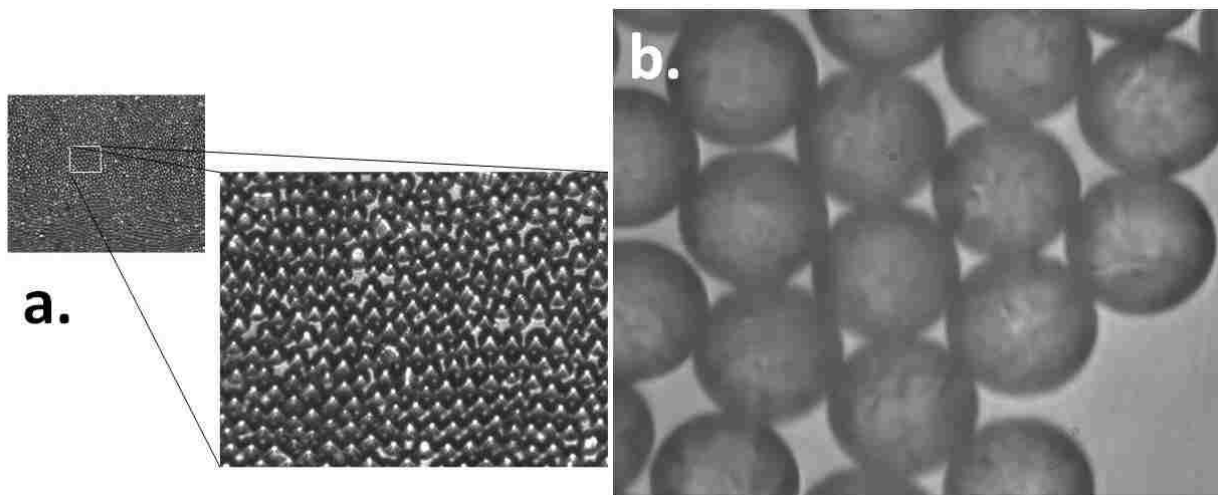


Figure 0.6: Microfluidic emulsification produces monodisperse emulsion droplets that can be converted 1:1 into solid polyurethane particles. a) Micrograph of a monodisperse precursor emulsion in a fluorocarbon oil. b) Micrograph of dried monodisperse polyurethane latex particles.

The synthesis of monodisperse particles is possible through suspension polymerization of uniformly sized precursor droplets. The method of choice for making monodisperse droplets is hydrodynamic flow focusing in microfluidic channels. Microfluidic devices fabricated from PDMS exhibit good chemical resistance to the PU-precursor and fluorocarbon continuous phase. A monodisperse PU-precursor emulsion dispersed in fluorocarbon oil is shown in Fig. 2.6. Its polymerization yields monodisperse particles (Figure 2.6 b)). Upon drying, the fully converted particles exhibit small wrinkles on their surfaces. These are due to particle deformations on the glass slide that arise from the low glass transition temperature of

the polymer. These results demonstrate that fine control over the particle size is achieved by combining microfluidic emulsification with suspension polymerization. Moreover, they show that the surfactant enables

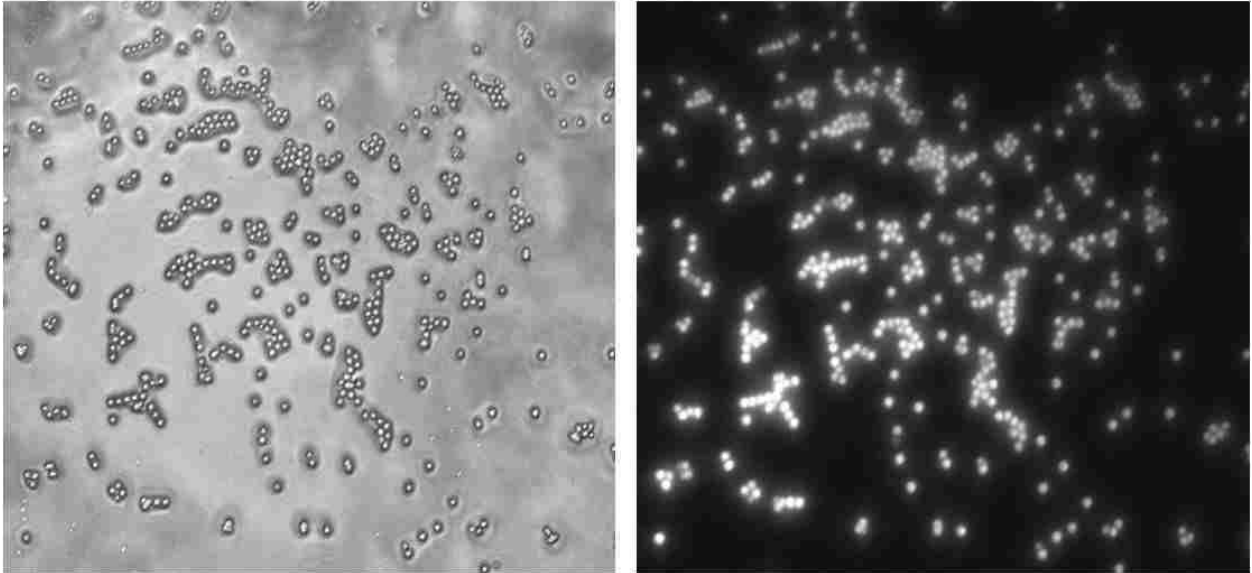


Figure 0.7: Micrographs of the dried, fluorescently labeled, monodisperse particles of a polyurethane latex. The synthesis of fluorescent particles is one example of chemical modification through the addition of functional reagents to the PU-precursor.

emulsification through hydrodynamic flow focusing and that it provides sufficient stability of the fluorocarbon-based emulsions against coalescence throughout the polymerization, even at an elevated temperature of 50 °C and even in the absence of a catalyst.

Polyurethanes may be modified by adding reagents to the precursor. These will be incorporated into the polymer backbone during the course of polymerization. The fact that the composition of the precursor droplets is identical to that of the precursor before emulsification and that it does not rely on the diffusion of precursors makes suspension polymerization much more versatile than emulsion or precipitation polymerization.

Therefore, the nature and amount of reagents may be set freely, without consideration of their diffusion constants in the continuous phase. An advantage of step-growth polymerization reactions, including the polyaddition of polyurethanes, is that the added reagents will be homogeneously distributed along all polymer chains.

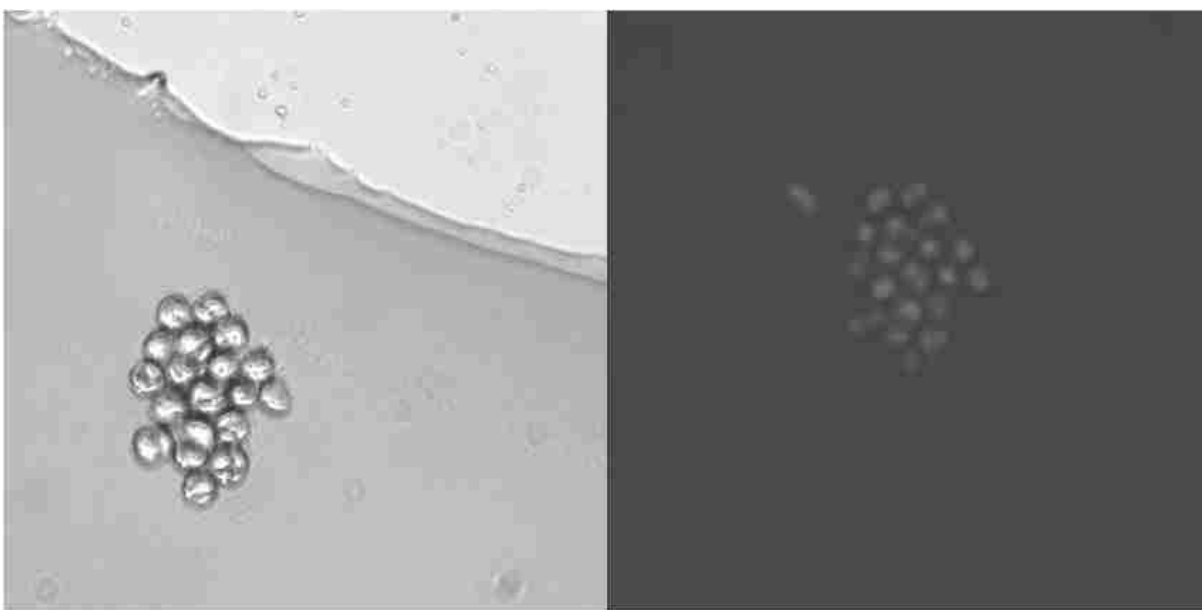


Figure 0.8: Cross-linked and fluorescently labeled polyurethane particles obtained from suspension polymerization in a single processing step. The addition of THF swells, but does not dissolve the particles, indicating high conversion and efficient cross-linking.

Reactive fluorescent dyes are a traceable example of covalently linking reactive additives to the backbone of the PU-polymer molecules in the particle (see Figure 2.7). Due to reagent availability, the fluorescent dyes are incorporated in the polyurethane through urea links. An advantage of this approach is that fluorescent particles may be obtained in a single processing step. Fluorescently labeled and monodisperse particles (Figure 2.7 b)) may be useful as tracer particles in analytical applications.

We have also synthesized cross-linked PU-particles. This is another example of the versatility that suspension polymerization affords through the addition of functional reagents. Cross-linking can be accomplished by replacing a small amount of dialcohol or diisocyanate with a trifunctional reagent, while maintaining a strictly stoichiometric 1:1 ratio of alcohol and isocyanate groups. Unlike conventional solvent-evaporation processes for the synthesis of PU particles, suspension polymerization produces cross-linked particles in a single polymerization step. Moreover, fluorescent labeling does not require any additional processing steps. With the surfactant system used here, neither cross-linker molecules nor reactive dyes change the colloidal stability of the emulsions. Effective cross-linking is confirmed by dissolution tests with an appropriate solvent, such as THF: Cross-linked particles swell, but do not dissolve (see Figure 2.8 a)) as would particles that are not cross-linked.

Cross-linked polymer particles synthesized in this way are unique in that they do not have gradients in cross-linking density. A polymer network with homogeneously distributed cross-links is inherent to the step polymerization mechanism and cannot be obtained from free radical polymerization as propagation constants always differ for the cross-linker and the monomer. Thus, in this way, we can prepare homogeneously cross-linked, monodisperse, and fluorescently labeled organic microgel particles as shown in Figure 2.8 b); these will be useful as model systems in fundamental studies on swelling and diffusion inside particles where homogenous distributions of cross-links are required.

Reducing the effective volume fraction of the precursor within a particle allows the tuning of the mechanical properties of the polymer particle. This may be achieved by diluting the

precursor with an inert solvent that dissolves both the precursor and the polymer. In this way, suspension polymerization affords control over the mesh size of a cross-linked polymer particle. Microgel-particles that are polymerized with small volume fractions of precursor will swell upon addition of a suitable solvent. The degree of swelling will determine the stiffness of the microgel particles.

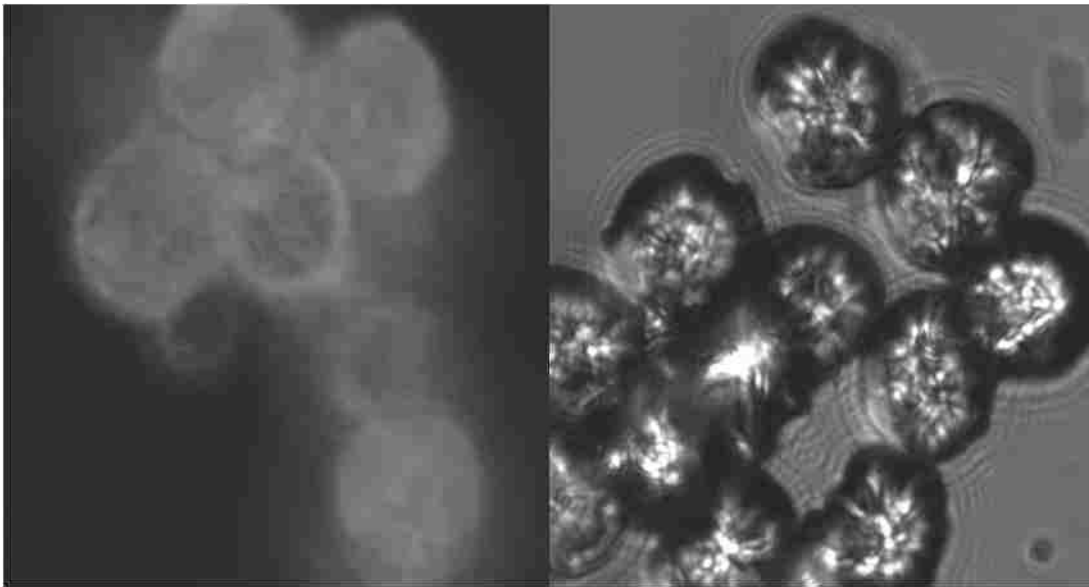


Figure 0.9: Demonstration of the versatility of PU-suspension polymerization: Diluting the precursor before emulsification with an inert solvent allows the mesh size of cross-linked particles to be tuned. The micrographs show particles that were polymerized while being diluted 1:1 with DMSO. The wrinkles appear upon drying of the particles.

Cross-linked PU-particles, whose precursor was diluted with an equal volume of DMSO prior to emulsification, are shown in Fig. 2.9. The dried particles shrink considerably as indicated by the pronounced wrinkles at their surface; for comparison, Fig. 2.8 b shows

cross-linked particles of the same composition that were synthesized from an undiluted PU-precursor.

Microgel particles may serve as a scaffold for composite particles: the microgel network is swollen with the precursor of another polymer that is subsequently polymerized. The synthesis of such particles benefits from the ability to stabilize organic droplets in a wide range of polarities, including DMSO, with PEG-based non-ionic fluorosurfactants.

2.1.3 Conclusion

We have developed non-ionic fluorosurfactants that allow an unprecedented range of particle syntheses through conversion of precursor emulsion droplets. The immiscibility of fluorocarbon oils with hydrocarbons of almost any polarity allows formation of droplets that cannot be formed in any other continuous phase. Hydrophobic chemicals may be emulsified in a dry environment facilitating water-sensitive reactions. We demonstrate the benefits of this system with the examples of suspension polymerization of polyurethane particles. In a simple one-step process, solid particles are made with the options of cross-linking, grafting fluorescent dyes to the polymer network, and controlling its mesh-size through addition of an inert solvent during polymerization. This process may be easily transferred to a variety of other polymers that rely on water-sensitive syntheses, such as polyesters, polyureas, and to transition metal alkoxides. Organic droplets that allow for water sensitive reactions are also promising for fields other than particle synthesis, such as heterogeneous catalysis or screening applications using drop-based microfluidics.

2.2 Droplet-Based Microfluidics for Emulsion and Solvent Evaporation Synthesis of Monodisperse Mesoporous Silica Microspheres

2.2.1 Introduction

Recently, Andersson et al. [88] demonstrated the synthesis of spherical, mesoporous silica particles using an approach which combines previously established emulsion-based precipitation methods [89, 90] with the EISA method. This synthesis route, referred to as the emulsion and solvent evaporation method (ESE), produced well-ordered 2D hexagonal mesoporous silica microspheres. The advantages of this method are control of synthesis parameters such as emulsion droplet size, temperature, evaporation speeds, humidity, and the composition of the surfactant solution. In comparison to aerosol methods, the relatively slower evaporation rate of the solvent from the emulsion droplets allows a high-degree of homogeneity of the components in the liquid crystalline phase prior to fossilization of the structures by silica condensation. This is perhaps the most important distinction of the emulsion EISA method from aerosol-based EISA methods. The emulsions were prepared in bulk using inhomogeneous vigorous stirring. As a result, the droplets, and therefore the particles, were produced with a relatively broad size distribution.

The fabrication of monodisperse silica microparticles containing highly ordered nanometer-scale pores (mesopores) of controllable size presents both a fundamental challenge and is of practical interest [91]. They can be used for controlled drug delivery, molecular, biomolecular [92] and cellular [63] encapsulation. Monodisperse particles can be ordered

into 2D and 3D lattices [93, 94], which allow the fabrication of catalysts with well-defined pore hierarchy. Mesoporous particles also have significant potential for the design and implementation of chemical and biochemical sensors [95].

Microfluidic flow focusing devices (MFFDs) provide a straightforward and robust approach to formation of highly monodisperse emulsion drops [19]. It has been demonstrated that microfluidic-generated drops can function as both morphological templates and chemical reactors for the synthesis of monodisperse polymer [3, 5, 19] and biopolymer [6] particles.

In this paper we suggest a novel procedure for fabrication of well-defined monodisperse mesoporous silica particles. It is based on MFFD emulsification of an aqueous-based sol [96] with subsequent EISA processing utilizing the ESE method [88]. The droplet-based microfluidic methodology can be easily developed further to allow for controlled loading and incorporation of cells, biomolecules, functionalized particles, and polymers within monodisperse, highly structured silica mesoporous microspheres.

2.2.2 Materials and Methods

The silica precursor solution was prepared by hydrolyzing 5.2 g of tetraethylorthosilicate (TEOS, Purum >98%) in 3 g of ethanol (99.7%), and 2.7 g of .01 N hydrochloric acid (pH 2) under vigorous stirring at room temperature for 30 min. Next, 1.4 g of the amphiphilic, triblock copolymer templating molecule (Pluronic, BASF: P104) was dissolved in 5.43 g of DI water and subsequently mixed with the hydrolyzed TEOS solution to complete the

preparation of the aqueous-based sol. We designed this particular recipe to allow the use of Pluronic surfactant as a templating reagent in the presence of a much lower concentration of ethanol than used by other authors [88].

Emulsification of the aqueous siliceous precursor was achieved by supplying the sol dispersed phase and organic oil continuous phase to the microfluidic device using two digitally-controlled Harvard Pico Plus syringe pumps. The continuous phase was prepared by dissolving ABIL EM 90 (Degussa) surfactant in hexadecane (3 wt %) which served as an emulsion stabilizer. The volumetric flow rate for the dispersed sol was optimized to 0.5 $\mu\text{L}/\text{min}$, with a flow rate of 3.5 $\mu\text{L}/\text{min}$ for the continuous oil phase. The SU-8 photoresist-templated poly(dimethylsiloxane) (PDMS) microfluidic device was fabricated using a well established soft-lithography method [21]. The microfluidic devices used in this study was discussed in chapter 1.

The MFFD-produced droplets were transferred to a 50 mL round bottom flask, and heated to 80 °C under a reduced pressure of 70 mTorr for two hours. The flask was pretreated with RAIN-X solution to make it hydrophobic. This was necessary to prevent the droplets from sticking to the flask bottom. To prevent droplet flocculation and coalescence before the sol-gel transition is complete, the emulsion was subject to constant stirring at 200 rpm. This stirring was sufficient to keep the droplets suspended and separated. At the same time it did not lead to shear deformation. As shown in figure 2.10, the droplets lose approximately half of their diameter due to the evaporation process.

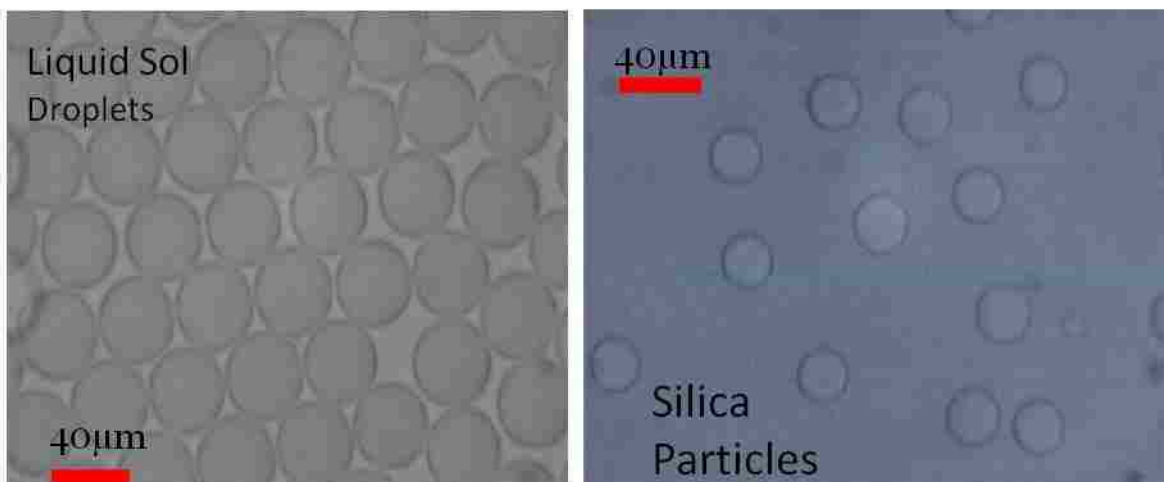


Figure 0.10. Left: Silica precursor drops suspended in hexadecane; Right: Silica particles after EISA processing. The droplets shrink ~ 50% due to the evaporation process.

2.2.3 Results/Discussion

Figure 2.11 shows silica particles obtained from TEOS precursor droplets formed in hexadecane oil. The hexadecane allows for the solvent (DI water and ethanol) to be expelled from the droplets, which leads to polymerization of the templated silica. Figure 2.11 a shows particles that were obtained from a shaken bulk emulsion. The particles have a well-defined spherical shape but are very polydisperse. It is not possible to improve on this because a shaken emulsion produces polydisperse droplets, which later result in a wide particle size distribution. Increasing the energy input (stirring intensity) during emulsion formation narrows the size distribution but cannot produce monodisperse droplets. (See also ref 88.) Furthermore it will lead to the formation of smaller droplets on average. Therefore, varying the energy input does not allow us to decouple the size from the polydispersity.

Using the microfluidic flow focusing device, we were able to form monodisperse droplets, which is the necessary condition for obtaining well-defined monodisperse particles. The size of the droplets depends on the dimensions of the microchannel, the flow rates in the central and side channels, the viscosity of the fluids (water/ethanol and oil), and the surfactant.

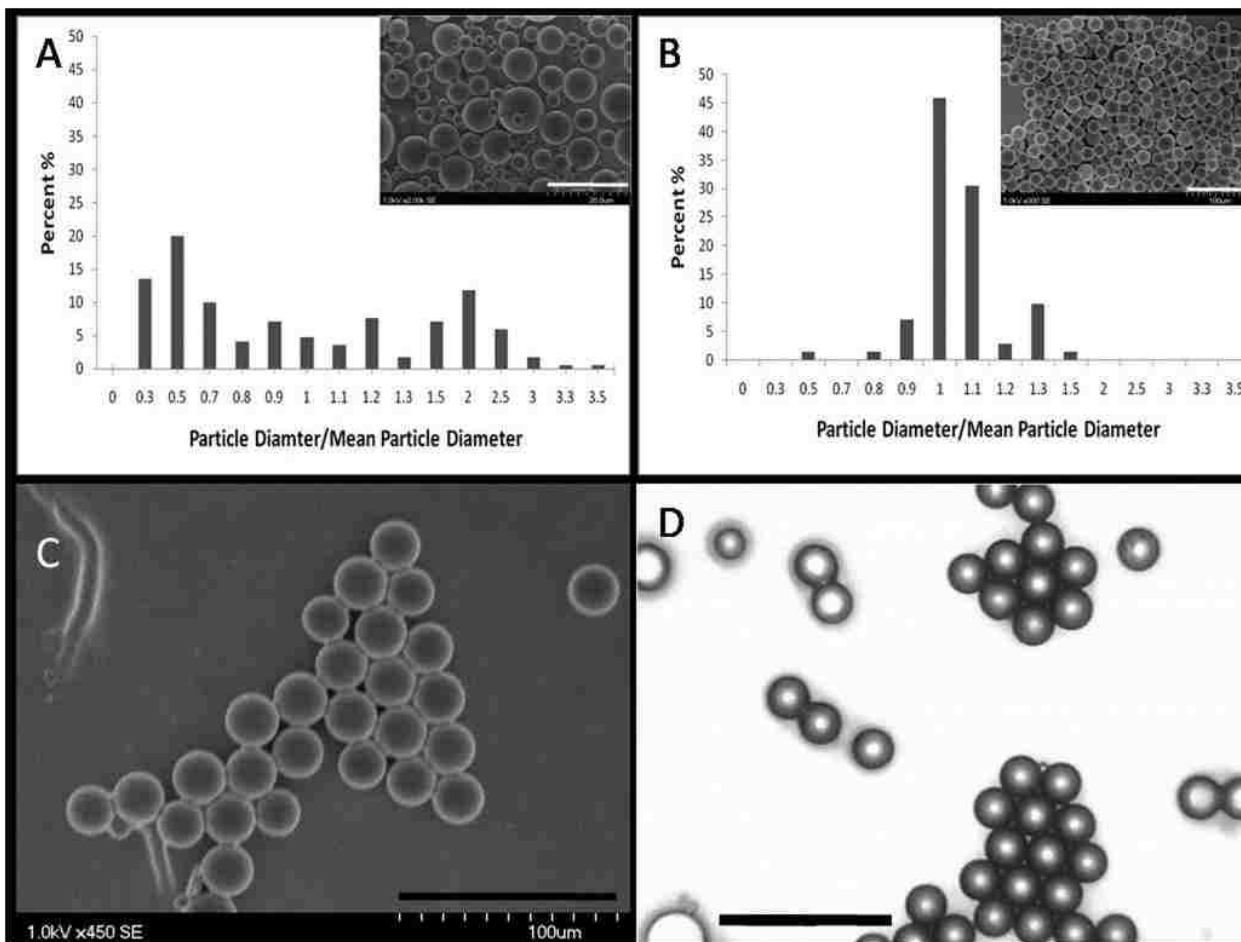


Figure 0.11: (a) Polydisperse silica microspheres templated from shaken bulk emulsion. Scale bar is 20 μm. (b) Silica microspheres templated by monodisperse microfluidic device-generated droplets. Scale bar is 100 μm. (c) Scanning electron microscopy image and (d) optical photograph (scale bar is 40 μm) of particles that have fused together in a hexagonal array. The particles are connected by “bridges” which form when the particles come into contact before the completion of the gelation process. The particles were then collected and centrifuged followed by calcination in air at 500 °C for 5 h to remove the templating surfactant.

Hence, a single device can produce monodisperse droplets of different sizes by varying the relative magnitude of the viscous and interfacial forces that are involved [19]. We were able to vary the droplet size by 1 to 3 times the channel width. Hence, to cover a wider range of sizes one may need more than one microfluidic device or may have several channels, each with different sizes, fabricated on the same device.

The size distribution and the corresponding SEM image of the particles are shown in Figure 2.11 b. These particles were obtained using the microfluidic device shown in Figure 1.15, which has 25 μm wide channels. This device can produce droplets between 25 and 75 μm and particles of about half that size. The particle size distribution in Figure 2.11 b exhibits one well-defined peak centered at around 23 μm . Particles like these are obtained from droplets that were initially between 35 and 40 μm in diameter. After the solvent (water and ethanol) is expelled, the final size is the one shown in Figure 2.11 b. There is a second peak at 30 μm that is most likely due to some coalescence that occurred before the droplets turned into silica particles. The lower limit for the dimension for soft lithography is determined by the printing process that is used. Fabricating channels that are about 10 μm wide using soft lithography is quite plausible. Such channels will produce particles on the order of 5 μm in diameter. To produce smaller particles, one may need to fabricate smaller channels using different methods [97, 98] or exploiting the extreme hydrodynamic regimes [19].

As we discussed above, the particles might stick together during the final stages of solvent evaporation unless some precautions are taken. However, this sticking could be exploited to obtain arrays of interconnected particles. Such interconnection adds to the structural integrity and allows robust 2D layers of well defined monodisperse mesoporous particles to be

fabricated. A layer of bound particles can be manipulated, transferred to different substrates, and incorporated into other applications in catalysis, sensing, and so forth. An example of such multiparticle 2D structure is depicted in parts c and d of Figure 2.11, which shows a scanning electron microscopy image and an optical photograph of particles that have stuck together in a hexagonal array, respectively. The particles are connected by “bridges” that form when the particles come into contact before the completion of the gelation process.

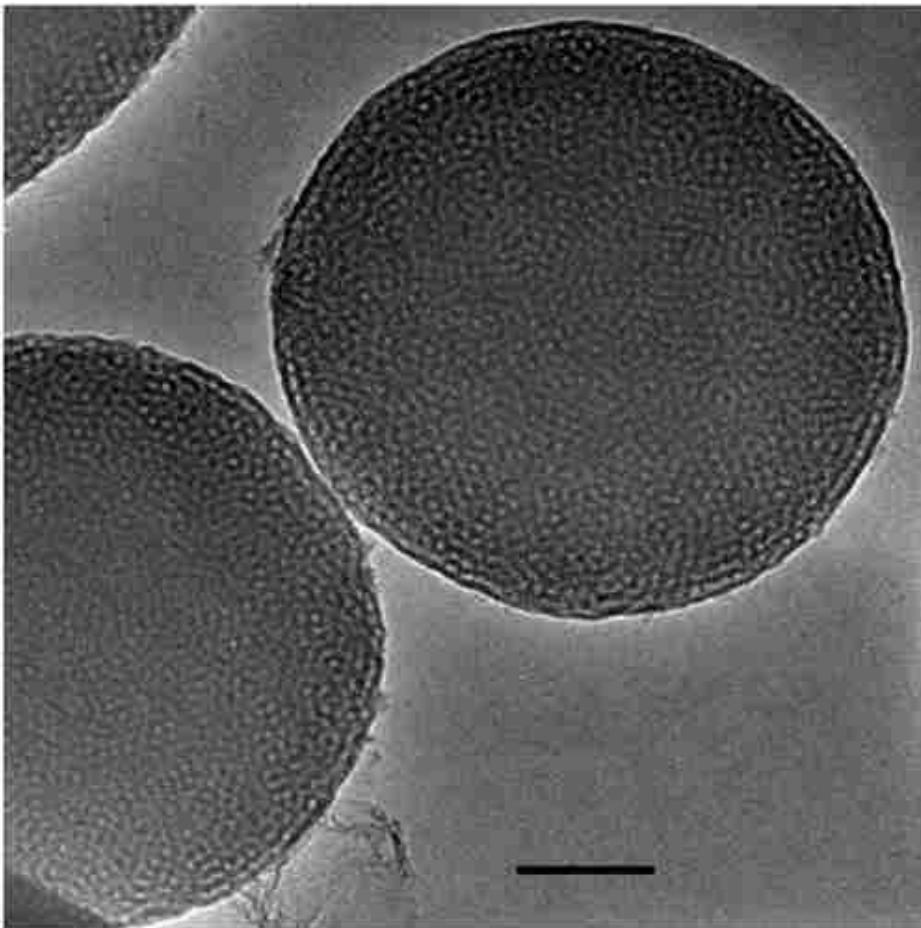


Figure 0.12: TEM image of P104 templated mesoporous silica particles (scale bar is 1 μm).

Figure 2.12 shows a transmission electron microscope image of silica particles with internally ordered mesoporous structure. The particles were selected from the lower end of the distribution curve in Figure 2.11 b. This allowed us to get a better image of the internal mesoporous structure. The pores have an approximately uniform size, which for the

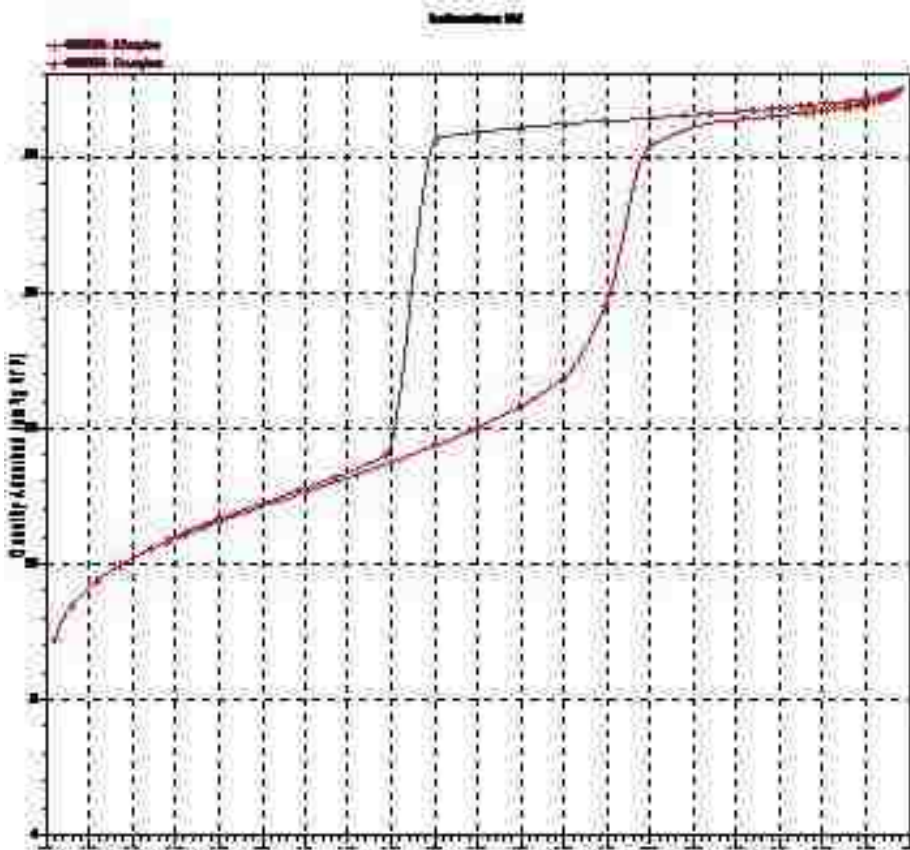


Figure 0.13. Nitrogen sorption isotherm for emulsion and evaporation synthesized silica particles.

surfactant that we used (and BJH pore-size model) is 6.4 nm, and a pore volume of 0.56 cm³/g. The pores seem to be closed at the surface, which is also the case reported by other authors [88, 96] Hence, microfluidics can be successfully used to fabricate

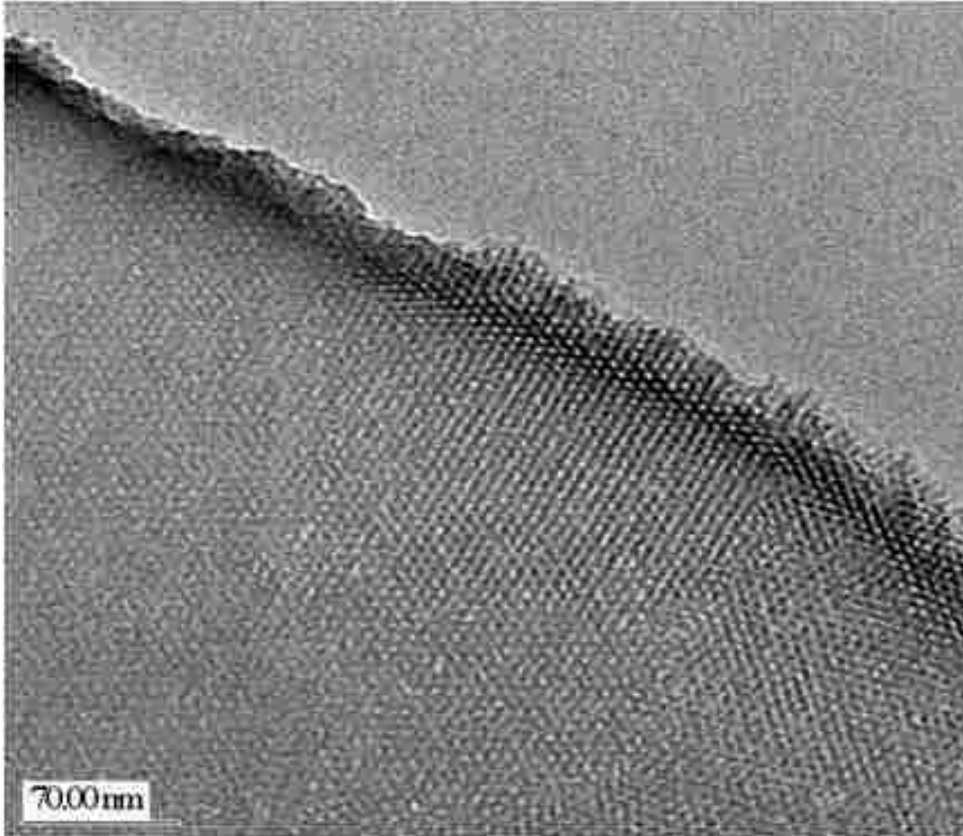


Figure 0.14: TEM of hexagonally ordered cylindrical nanopores obtained by the emulsion and solvent evaporation method.

silica spheres with well-defined size and internal porosity. Other types of water-soluble surfactants may be used for templating, which could extend the range of pore size and morphology.

By varying the concentration of the templating surfactant, P104, particles were obtained with hexagonally ordered cylindrical pores as shown in figure 2.14.

2.2.4 Concluding Remarks

We have demonstrated that microfluidics can be successfully used to fabricate monodisperse mesoporous silica particles with well defined size. A great advantage of the monodisperse particles is that they can be ordered in 2D arrays on various substrates [99, 100]. Controlled bridging and sticking of the particles allows fabrication of arrays with sufficient structural integrity for subsequent manipulation and application. Monodisperse mesoporous particles can also be ordered in three dimensional structures for example by repeated deposition of layers following the technique from Refs. 99 and 100. This would allow structures with well defined pore hierarchy to be obtained. Particles with surfactant templated mesopores define two very different length-scales: one in the micrometer (particle size) range and the other in the nanometer (surfactant templates) range. The methodology developed here can be applied to derive mesoporous particles in a wide variety of sizes and can be modified to include other metal oxides.

The processing conditions for the surfactant templating described in this work are very different from those used in the alternative aerosol method [91]. The kinetics of solvent evaporation in our case is much slower because the solvents (water and alcohol) are transported across the continuous hexadecane phase. This means that the surfactant has a longer time to self assemble into micellar structures that are closer to equilibrium. In the aerosol method the solvent removal is very fast and some of the structures can be kinetically trapped. Thus, the slower kinetics will lead to better control on the pore structure and sizes. It also allows the study of the surfactant self-assembly process in the silica which is not tractable when the solvent evaporation is too fast. Solvent evaporation and removal across

the continuous organic (hexadecane) phase can also be used to obtain other mesoporous structures like films and membranes. These structures do not require the use of microfluidics but may benefit from the slower kinetics.

Microparticles with Bimodal Nano-Porosity Derived by Microemulsion Templating



3.1 Introduction

Particles with well-defined pore morphology are essential for many areas of modern technology. Potential applications include catalysis [101, 102] and electro-catalysis [103], chromatography [104] and drug delivery [105]. Precise control over the pore-size and shape is crucial for the successful performance of the particles. It allows for optimization of fluid

transport in a catalyst, determines the molecular release of solute by a drug delivery vehicle, or defines the size selectivity in chromatography. Templating of oxide materials with surfactant micelles is a powerful method to obtain mesoporous structures with controlled morphology [106]. Oxide (e.g. silica) precursor solution is mixed with a templating surfactant and evaporation of the solvent leads to an increase in the surfactant concentration. The surfactant forms supra-molecular structures according to the solution phase diagram. This is known as evaporative induced self-assembly (EISA) and has been used to obtain bulk porous materials or microparticles using high-temperature aerosol methods [75, 107]. Microfluidics was also used by Lee *et al.* [108] to fabricate monodisperse particles with very interesting surface morphology.

To address the requirements of emerging technologies, the next generation of porous oxide materials must be highly structured and functionalized. Hierarchically porous structures offer advantages in design of materials where catalytic activity is to be utilized in immediate conjunction with transport of reactants. Templating approaches for hierarchical materials fabrication are attractive as they can be combined with other methods such as impregnation or precipitation to yield structures with controlled porosity, surface chemistry and hydrophilicity or hydrophobicity.

This chapter describes the design of mesoporous microparticles with biporous internal structure. The two types of pores are due to the coexistence of oil microemulsion droplets with smaller ionic micelles in aqueous drops of a few microns in diameter. This has been accomplished by tuning the phase state of oil/water surfactant mixture to ensure the presence of the different species.

3.2 Experimental Approach

The silica precursor solution was prepared by dissolving 1.82 grams of cetyl trimethylammonium bromide (CTAB) in 20 g of DI water under vigorous stirring at 40 °C until the solution is clear. Next, 5.2 g of tetraethylorthosilicate (TEOS, Purum >98%) and 0.57 g of 1 N hydrochloric acid was added to the mixture under vigorous stirring at room temperature for 30 min to hydrolyze and dissolve the TEOS monomer. The measured acidity of the hydrolyzed sol showed pH \approx 2. The oil phase was prepared by dissolving a modified polyether-polysiloxane/dimethicone copolyol surfactant with the trade name ABIL EM 90 (Degussa) in hexadecane (3 wt %). The aqueous siliceous precursor solution was then added to the oil phase and subsequently emulsified by brisk shaking of the vial. The emulsion was transferred to a 1000 mL round bottom flask and heated to 80 °C under a reduced pressure of 70 mTorr for 3 h. The particles were collected and centrifuged, the supernatant oil removed, followed by calcination in air at 500 °C for 5 h to remove the templating surfactant. The carbon precursor was prepared by dissolving 475 mg of sucrose in 1 ml of 2M H₂SO₄ and then adding 2.6 ml of acetone. Addition of acetone was necessary to obtain good wetting of silica particles with sucrose solution. The resulting solution was added to 200 mg of silica particles in increments of 100 μ l and was dried between infusions. After all solution was added to the silica particles they were dried in the oven at 70°C overnight. This was followed by pyrolysis at 900°C in an N₂ atmosphere for 4 hours, ramp rate at 3° per min. After pyrolysis silica was etched in 6M KOH for 4 days. Synthesis of carbon decorated with

platinum nanoparticles proceeded in a similar way. First, silica was impregnated with carbon precursor. Then, platinum precursor, H_2PtCl_6 , dissolved in 2M H_2SO_4 and mixed with acetone, was added to silica particles filled with sucrose. Resulting material was heat-treated and pyrolyzed at the same conditions as the silica-carbon material. The material was then filtered, washed 5 times with DI water and dried in the oven at 70°C.

Dynamic light scattering (DLS) studies were acquired on a Nanotracs NPA250 dynamic light scattering instrument from Microtrac Inc. The measurements were separately performed in the two macroscopic phases (aqueous solution of the CTAB and silica precursor that has been in contact with the oil containing the ABIL EM 90). After waiting for 48 hours the oil phase spontaneously dispersed into the water in absence of any additional stirring. The X-ray powder diffraction (XRD) patterns were obtained on a Scintag diffractometer (Cu KR radiation). Transmission electron microscopy (TEM) was conducted on JEOL 2010 and 2010F instruments, and scanning electron microscopy (SEM) was done on a Hitachi S-800 instrument. Nitrogen (77.4) adsorption/desorption measurements were performed on a Quantochrome Autosorb-I-MP instrument. Prior to analysis the sample was outgassed overnight at 120°C. The adsorption data were analyzed using an NLDFT approach and cylindrical pore model.

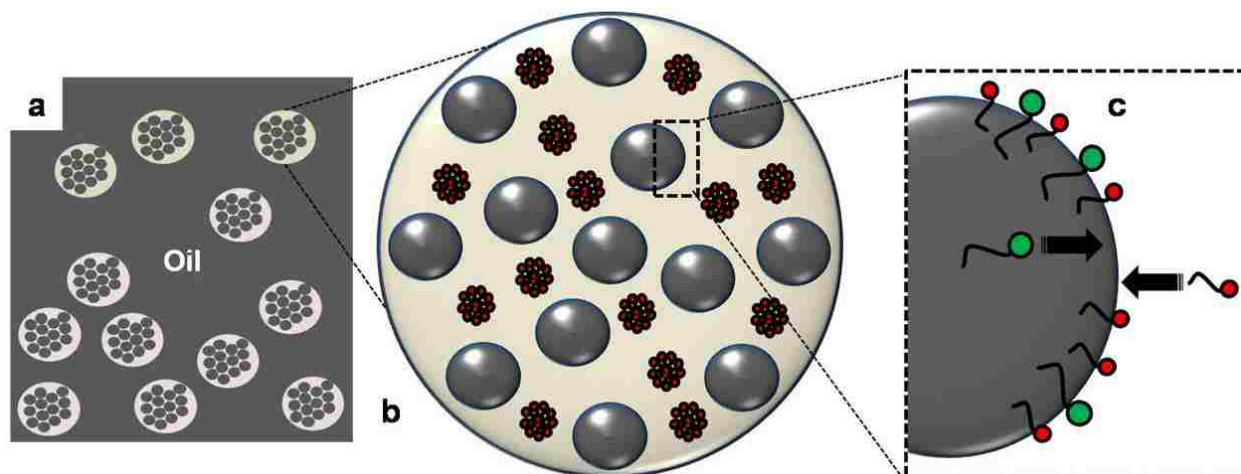


Figure 0.1: Sketch of liquid silica precursor emulsion system. (a) Aqueous silica precursor emulsion drops (light gray) in hexadecane oil (dark gray). Microemulsion droplets form and occupy the internal drop volume (small dark gray circles). (b) Single aqueous silica precursor drop. The CTAB is above the CMC forming, micelles (red) in addition to microemulsion droplets (dark gray). (c) Oil/water interface with adsorbing surfactants from the two immiscible phases.

3.3 Microemulsion Templated Silica Results/Discussion

In this study we describe the fabrication and testing of a new type of structured materials with two levels of porosity that were obtained by templating co-existing microemulsion and micellar structures. Microemulsions are thermodynamically stable oil/water/surfactant mixtures that exhibit rather complex phase behavior [7, 8, 109]. Their structure can be fine-tuned by selecting proper surfactants and oil phase, controlling the temperature and the concentration of electrolytes [110, 111]. Microemulsions can form droplets with diameters about a few tens of nanometers. Their size is much less than the micrometer-sized emulsion drops formed by agitating an oil/water/surfactants mixture. In our experiments, large aqueous drops contain smaller microemulsion oil droplets and surfactant micelles (see Figure 3.1).

The microemulsion droplets and the micelles in the space between them were used to

template and synthesize silica particles with bimodal porosity. Our procedure used an aqueous tetraethyl-ortho silicate (TEOS) precursor solution/hexadecane mixture and a combination of non-ionic and cationic surfactants [Abil EM 90 and Cetyl-trimethyl-ammonium-bromide (CTAB)]. The non-ionic surfactant (Abil EM 90) is soluble only in the oil phase while the cationic CTAB is dissolved only in the aqueous phase. Stirring the entire system leads to the formation of micrometer sized aqueous emulsion drops (containing TEOS) dispersed in a hexadecane oil phase (Figure 3.1a). These large drops are stabilized by the oil soluble Abil EM 90 surfactant. At the same time, microemulsion oil droplets spontaneously form at the larger aqueous drop interface and occupy its internal volume. This is due to the adsorption of the two surfactants at the oil-water interface and a synergistic drop in the interfacial tension (See Figure 3.1c), which facilitates the microemulsion formation [7, 8, 109-112]. Because the CTAB is above the critical micellization concentration (CMC), the aqueous phase will also contain micelles (Figure 3.1b). Finally the drops are subject to solvent removal and silica polymerization [113], which fossilizes the microemulsion and micellar structures, producing a bimodal porous network within the microparticles. As the solvent is removed the micelles may undergo further structural changes and form hexagonal structures [75, 113]. The bimodal pore-size distribution is a result of the coexistence of micelles and microemulsion droplets.

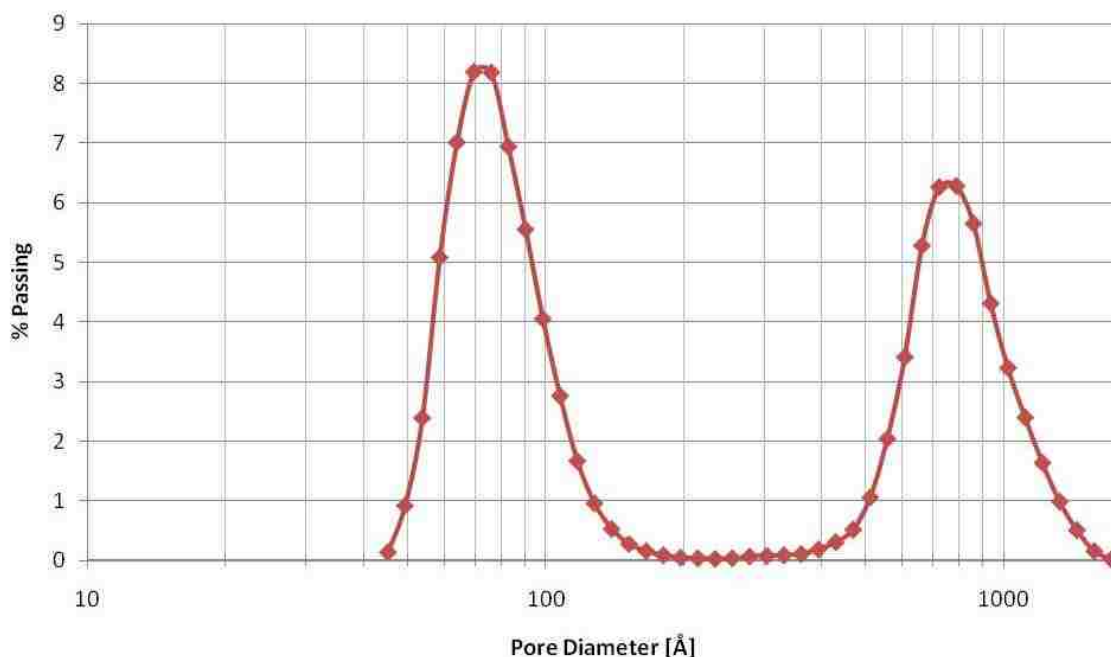


Figure 0.2: DLS of aqueous silica precursor solution suggest the presence of structures in the single nanometers existing with structures with dimensions in the tens of nanometers.

The coexistence of micelle and microemulsion structures was verified by dynamic light scattering (DLS) analysis of the precursor TEOS/CTAB aqueous phase which was in contact for 48 hours with the oil phase containing Abil EM 90. During that time we observed the spontaneous formation of microemulsion droplets at the interface. The DLS results are shown in Figure 3.2 where two well-defined peaks are present. The left peak represents the CTAB micelles, while the right peak is due to the microemulsion droplets. DLS measurements of the oil phase showed a single peak with maximum at ~ 30 nm and a long tail toward larger sizes. Determining the exact nature of these aggregates in the oil is beyond the scope of the current study.

The obtained silica particles exhibit a honeycomb-like structure observed by scanning electron microscopy (SEM) (figure 3.3), which shows the presence of cavities at the

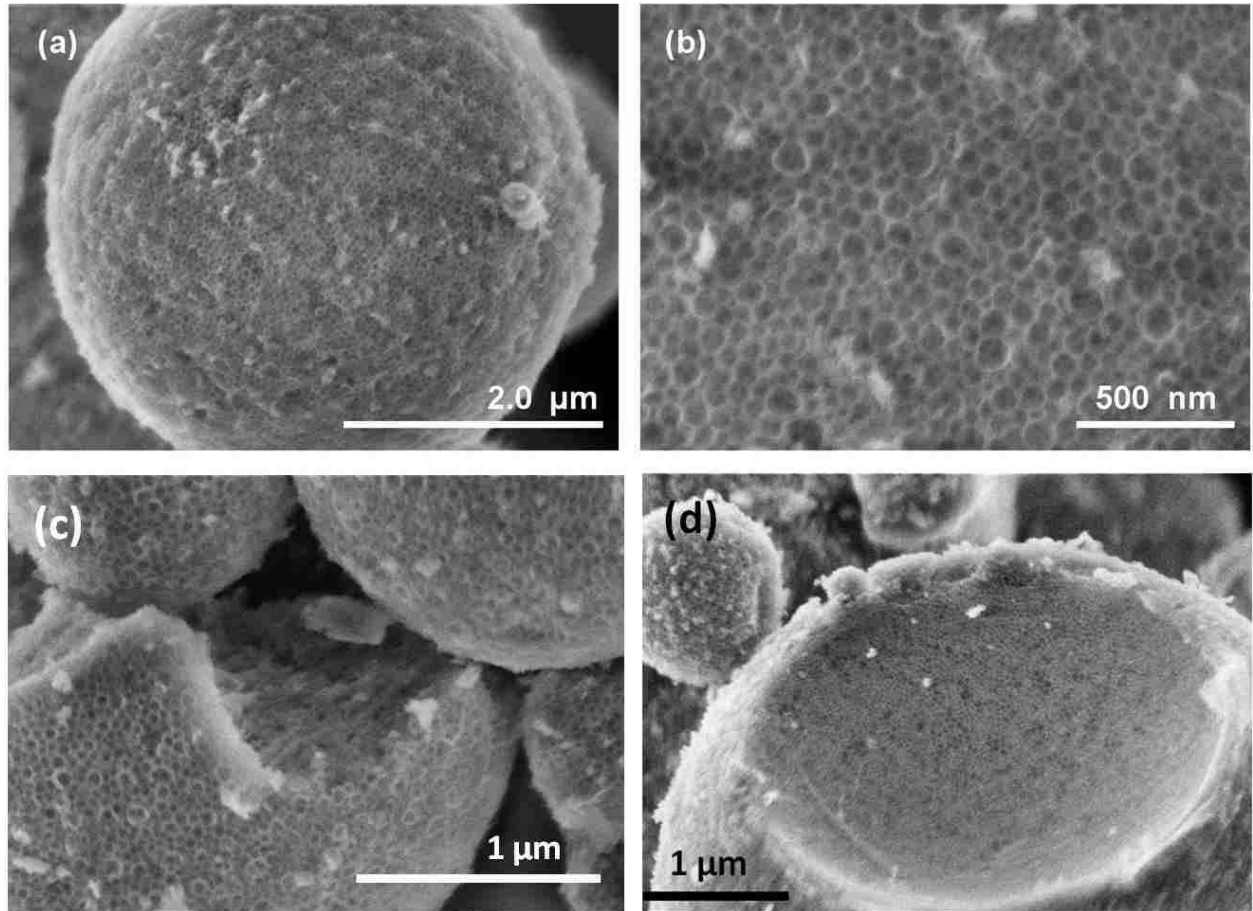


Figure 0.3: (a), (b): SEM images of miroemulsion templated silica particles; (b), (c): SEM images indicate large pores are present throughout template silica particles.

surface with diameters about 40 nm. SEM images of broken or partial particles suggest the large pores infiltrate throughout the particles. A transmission electron microscopy (TEM) micrograph of the particles indicates open access to the porous network (Figure 3.1 a), which facilitates impregnation of the interior with replica materials. Open access to the pores is

often not the case if only small surfactant micelles are templated [75, 88, 107, 113]. The TEM images of a particle cross-section in Figure 3.4 b and c confirms the presence of the large pores in the interior. The pore-size analysis (Figure 3.6) suggests the presence of larger (~10-30 nm) and smaller (~5 nm) pores. The cavities at the particle surfaces (observed by SEM) are larger than the pores in the interior of the particle.

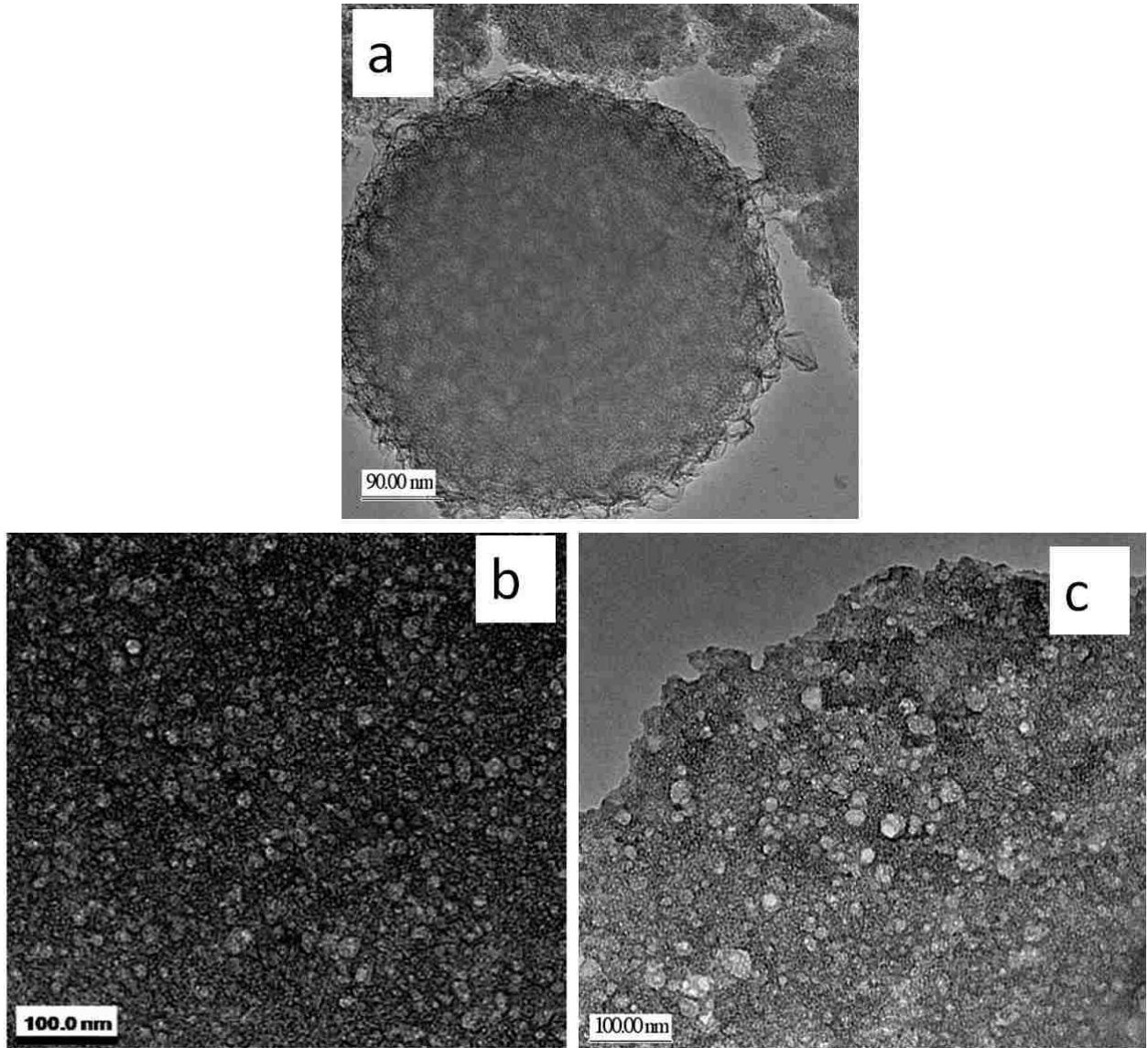


Figure 0.4: (a) TEM image of microemulsion templated silica suggest pores open at surface; (b), (c) TEM images of cross-sectioned silica particles.

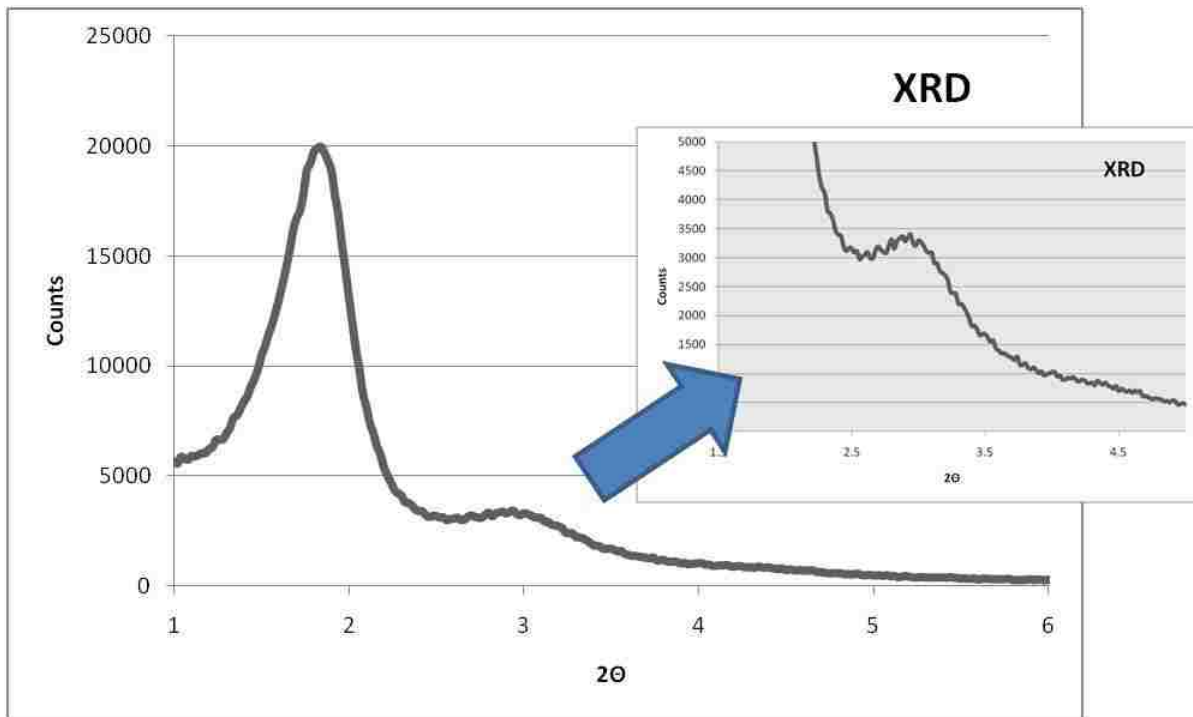


Figure 0.5: XRD for microemulsion templated silica suggests presence of smaller pores, hexagonally ordered, with a d-spacing of ~6 nm.

There is a discrepancy between the micellar and microemulsion sizes obtained by DLS and the respective pore dimensions. This can be due to shrinking of the silica upon solidification [114]. Another reason could be that DLS tends to overestimate the sizes for polydisperse samples [76].

The obtained silica microspheres have a Brunauer-Emmett-Tellert (BET) surface area and pore volume $\sim 1000 \text{ m}^2/\text{g}$ and 1.098 cc/g respectively. Most of the surface area is attributed to the presence of the smaller pores. These pores are not visible in the SEM image (Figure 3.3) however are detectable by TEM (Figure 3.4), adsorption measurements (Figure 3.6), and powder X-ray diffraction (XRD) (Figure 3.5). They are due to templating of CTAB micelles

that are present in the aqueous phase (see the first peak in Figure 3.2). The oil and surfactants are expelled by pyrolysis (see Materials and Methods).

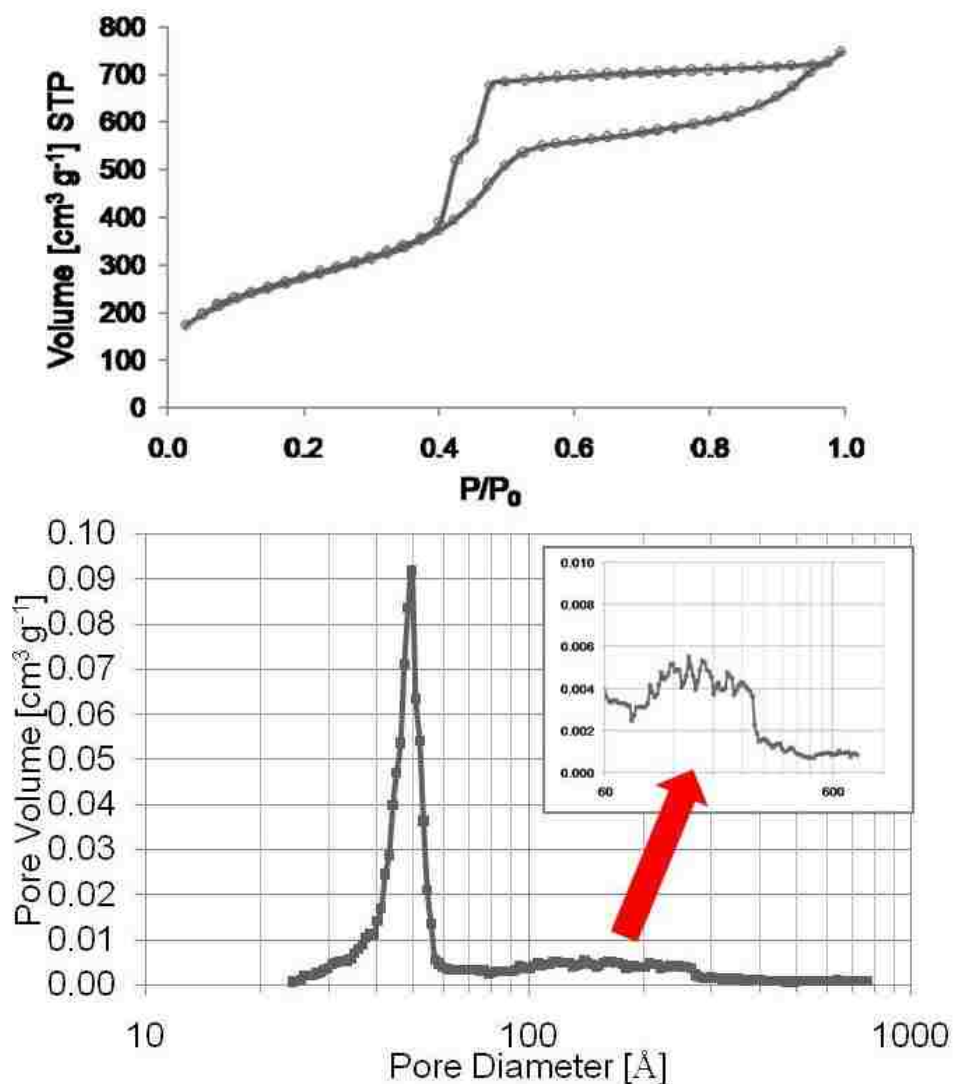


Figure 0.6: (top): Nitrogen sorption isotherm; (bottom) pore size distribution using NLDFT model

The nitrogen isotherm (Figure 3.6 top) is a type IV isotherm, with hysteresis typically observed for mesoporous materials undergoing Kelvin adsorption and desorption. The

stepwise shape of the desorption isotherm also further suggests the presence of pores with two different length scales leading to a plugging effect. The impact of the forced closure of the hysteresis loop can become even more pronounced when pore network effects occur and interconnected larger pores have to empty through pores with a smaller diameter, which can connect some of the larger pores to the outer surface of the particle. During desorption, the

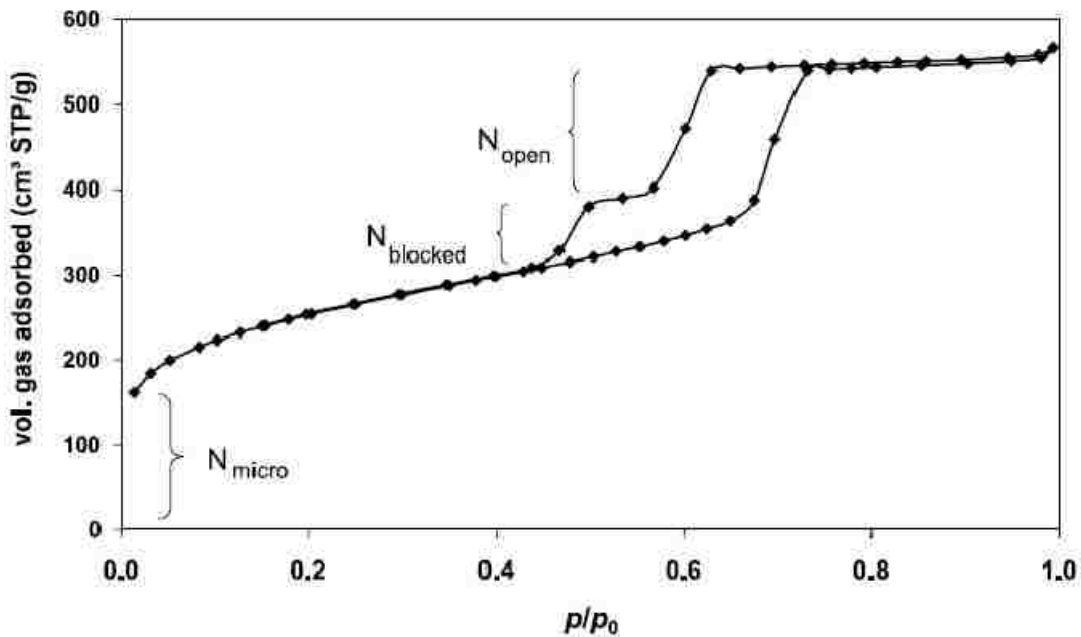


Figure 0.7. Isotherm of a typical plugged hierarchically porous silica material [115].

smaller pores empty at their corresponding pressure, being lower than that needed for emptying of the larger pores. However, some of the larger pores can only empty via passage through the small pores and accordingly will empty at lower pressure. Van Der Voort et al. [115] recently reported on the development of plugged hexagonal templated silicas containing both open and encapsulated mesopores. N₂ adsorption and desorption

experiments on these materials also result in a step-wise desorption isotherm, suggesting bimodal porosity, while the adsorption branch shows only one step representing the size of both the open and blocked mesopores. The step-wise desorption isotherm is due to the fact that the encapsulated mesopores empty at lower pressure than the open pores of similar size.

Other authors have also used microemulsion templating to fabricate monolith porous silica materials [89, 116-118]. Their materials did not have a subset of smaller nanopores because of the different templating solution used. An advantage of our approach is in offering synthetic paths toward hierarchically porous materials with controlled pore-size, chemical composition and physico-chemical properties at different length scales. This is particularly important for electrocatalysis and heterogeneous catalysis applications where fluid (gas or liquid) could easily penetrate the particles and travel inside through the large pores while the catalytic reaction occurs at the surface provided by the smaller pores. One can tailor the porous structure using Thiele-Modulus analysis. This is important for processes where no straightforward catalytic solutions are available to improve performance [103].

The development of hierarchically-porous structured electrocatalysts and their supports can effectively address some of the performance limitations of fuel cells. The design of electrocatalysts with high surface area and amount of accessible three-phase sites could potentially result in higher current densities. Highly porous structures can effectively minimize transport limitations, thus increasing the accessibility of the active sites by gas and liquid phases. The durability requirements of the fuel cells can be met by improving the corrosion stability of the current supports or design of novel resistant supports. Small pores can effectively lock Pt catalyst particles within a desired size range (see below) and will limit

their growth degradation during operation. Hence, our approach allows fabricating materials that will address mass-transport and durability limitations of the fuel cells.

The porous particles described above can be used as templates for the fabrication of porous carbon microspheres. The large pores in microemulsion templated silica allow for effective

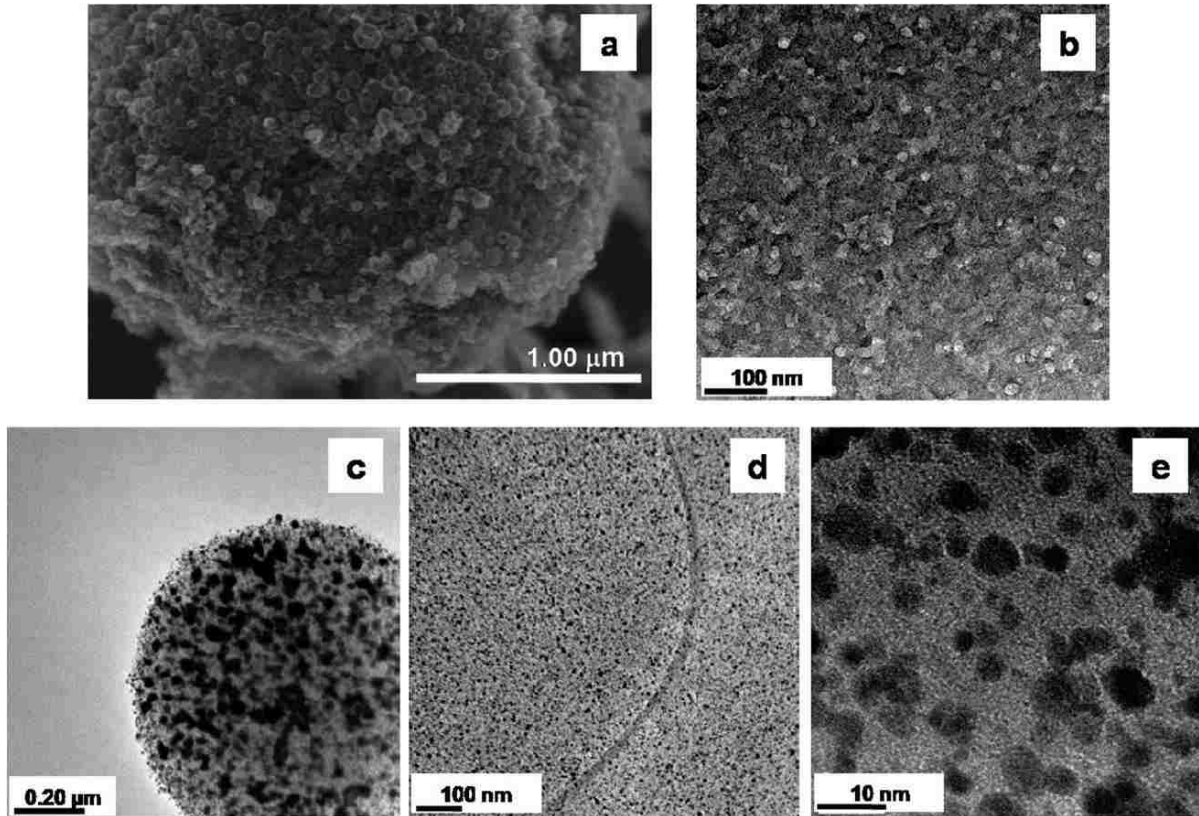


Figure 0.8: Characterization of templated carbon particles and template carbon particles decorated with platinum nanoparticles. (a) SEM image of carbon particle surface. (b) TEM image of the carbon particle cross section showing the internal structure. (c) TEM of the template carbon particle decorated with platinum nanoparticles. (d) TEM of the cross section of templated carbon particle decorated with platinum nanoparticles showing the internal structure and dispersion of the platinum nanoparticles. (e) TEM of the templated carbon particle decorated with platinum nanoparticles at higher magnification.

infiltration with precursor material to form replica of the particles. We incorporated carbon precursor (sucrose) into the pores by dry impregnation. Then, the material was pyrolyzed at 900°C for 4 hours and the silica support was etched in KOH solution. The resulting carbon material consists of particles with meso-structure that is a “lost-wax” replica of the silica. Each grain of carbon that is visible in the SEM image (Figure 3.8 a) corresponds to a microemulsion droplet that has been formed in the first step of the fabrication of silica microspheres. It is important that after the removal of the silica matrix the remaining microparticles do not disintegrate. The internal meso-structure of the carbon particle can be observed in the TEM micrograph of the cross-section of a carbon particle (Figure 3.8 b). The smaller pores of the silica were also filled with carbon precursor, creating “bridges” that provide the structural integrity to the carbon particle after the removal of silica. The BET surface area of these particles is 700 m²/g, which is comparable to commercial carbon black materials. Pore volume of carbon material is 0.382 cc/g. The size of the silica particles and the thickness of the walls of the large pores determine the dimensions and porosity of the carbon particles. The internal voids will improve the mass transport through the material when used as a support in the fuel cell. Further increase of the BET surface area and open-structure of the carbon material is possible by optimization of the synthesis procedure. This includes varying the precursor and/or its amount [119] to form porous instead of completely filled structures. For example, the precursor solution viscosity can be manipulated to obtain the desired structure.

These carbon nanostructured materials represent a unique scaffold to support noble metals such as platinum. A main goal in modern catalysis is to reduce the loading of noble metal

while maintaining high activity. Infiltration of platinum precursor immediately after the carbon precursor and preceding the pyrolysis step fixes the size of metal particles in the range of 3-6 nm by incorporation in the small pores. TEM analysis of the carbon particles decorated with platinum nanoparticles and their cross-sections has demonstrated a uniform distribution of the platinum throughout the interior (figure 3.8 c-e). The size of the platinum nanoparticles is in the desired range and can be further optimized by adjusting the synthesis procedure.

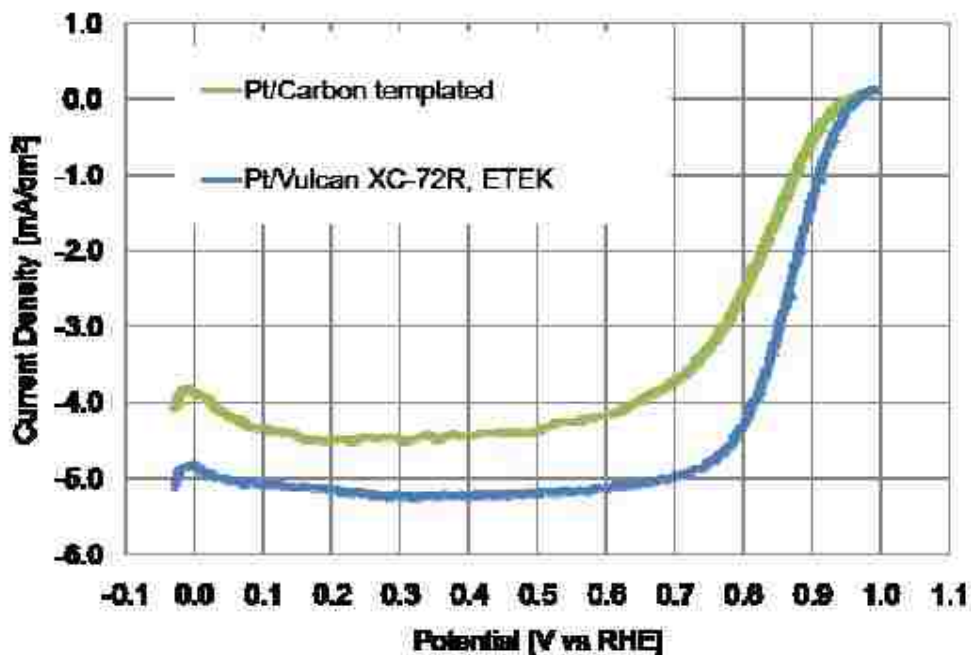


Figure 0.9. Electrochemical characterization of the template 30%wt.Pt/ and 30%wt.Pt/Vulcan XC-72R. Cyclic voltammograms in rotating disk electrode configuration were obtained in 0.1 M HClO₄ saturated with O₂ at 25°C at 10mV/s and 1600rpm. The catalyst loading was 20.5 $\mu\text{gPt}/\text{cm}^2$ for Pt supported on templated carbon and 21.7 $\mu\text{gPt}/\text{cm}^2$ for Pt supported on Vulcan XC-72R, from ETEK. The steep slopes on the right for both curves demonstrate the Pt-catalyst behavior.

The high surface area of the carbon material was preserved after decoration with platinum. The measured BET was above 600 m²/g for materials with Pt loading of 10-30 wt.%. Templated Pt/carbon electrocatalyst was tested in Rotating Disk Electrode (RDE) configuration and demonstrated promising results (figure 3.9).

The potential applications of the particles produced by the described technology can be extended by making them monodisperse using microfluidic techniques [113]. Monodisperse particles can be ordered in 2D and 3D arrays [99] that offer a third level of porosity associated with the void spaces between the microspheres.

3.4 Microemulsion Templated Silica Concluding Remarks

There are two necessary conditions for obtaining bimodal porous structures through the microemulsion templating procedure described in this paper. First the two surfactants should significantly decrease the interfacial tension when adsorbed leading to a spontaneous formation of microemulsion droplets [7, 8, 109, 110]. These droplets are templated to give the larger pores with dimensions of tens of nanometers. Second, the ionic surfactant should be soluble *only* in the aqueous phase while the non-ionic surfactant should be soluble *only* in the oil phase. The excess ionic surfactant that remains in the bulk forms micelles that are trapped in the solidifying silica, creating the subset of smaller pores with dimensions of a few nanometers. Microemulsion/micelle templating opens another avenue for materials design that can be utilized in synthesis of complex functional nano-materials. Better understanding of the physics that governs microemulsion structure will enable the next generation of

hierarchically-structured electrocatalysts through controlled design of the phase and templating. The current research aims at tailoring the morphology, pore properties and functionality of microemulsion templated materials for application as reduction and oxidation electrocatalysts in fuel cells.

3.5 Microemulsion Templated Niobium Oxide

The described methodology can be applied to other oxide materials, such as niobium, ruthenium and titanium, which are viewed as a promising alternative to carbon supports [120-124]. Below are listed various metal oxides which can be synthesized via the sol-gel process and their applications.

- SnO_2 : Tin oxide is interesting because of its conductance. Hence, mesoporous particles of SnO_2 could have an application in microfluidic-electrochemical devices for micro-fuel cells electrochemical sensing and others.
- TiO_2 : Titanium oxide has catalytic properties and the natural potential applications for mesoporous particles would be catalysis.
- RuO_2 : Ruthenium oxide has both conductive and catalytic properties. It presents interest for electrochemical, catalysis and other applications.
- NbO_2 and Nb_2O_5 : Niobium oxides have conductive properties and can be used in supercapacitors. This makes it particularly useful for energy storage in micro-devices and a variety of electrochemical applications.

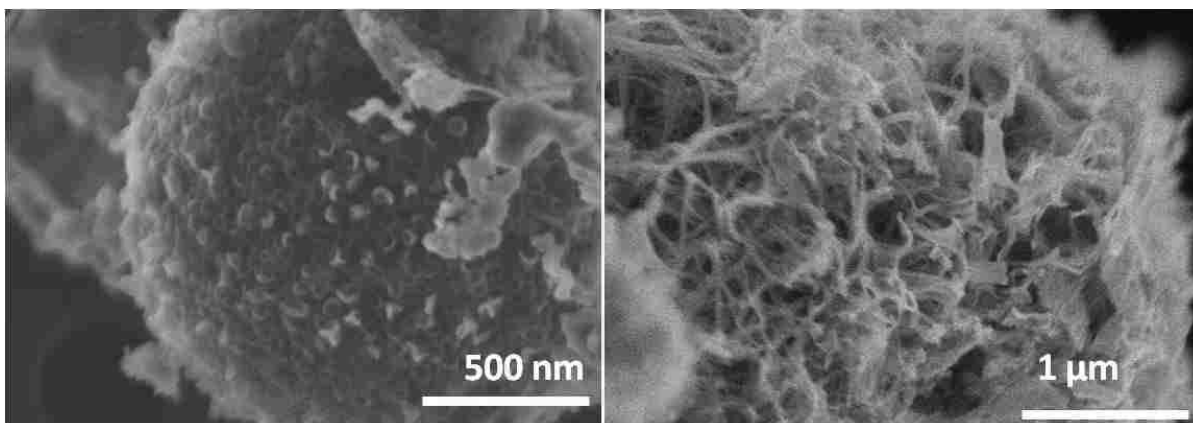


Figure 0.10: Niobium oxide particles formed via microemulsion templating.

Ammonium niobate (V) oxalate hydrate (Nb_2O_5) porous particles were fabricated by the same Microemulsion/sol-gel templating technique (figure 3.10). The particles have a measured BET surface area of $180 \text{ m}^2/\text{g}$.

3.6 Microemulsion Mixture Component Effect on Surface Pore

Morphology

It has been determined that slight variations in microemulsion mixture components (electrolyte concentration, wt% of surfactants, oil to sol ratio, etc.) can produce strikingly different pore morphologies and particle surface areas (Figure 3.11). This outcome is not surprising as variations in electrolyte concentration and surfactant concentrations has direct effect on interfacial tension values which directly determines the type and phase structure of microemulsion formed [112]. Figure 3.11 shows SEM images of the various particle surface morphologies formed and the associated BET surface areas by varying microemulsion

mixture components. The ‘standard microemulsion mixture’ was used in previous work [125] and formed particles with surface cavities(30-40 nm) in a honeycomb-like morphology (figure 3.11 a) with a BET surface area of 1000 m²/g. The molar ratios for the sol were TEOS/H₂O/HCl/CTAB = 1:44.5:0.63:0.20, with no added electrolytes. The oil phase was 3 wt% Abil EM-90 in hexadecane. Sol to oil phase ratio was 1:3.

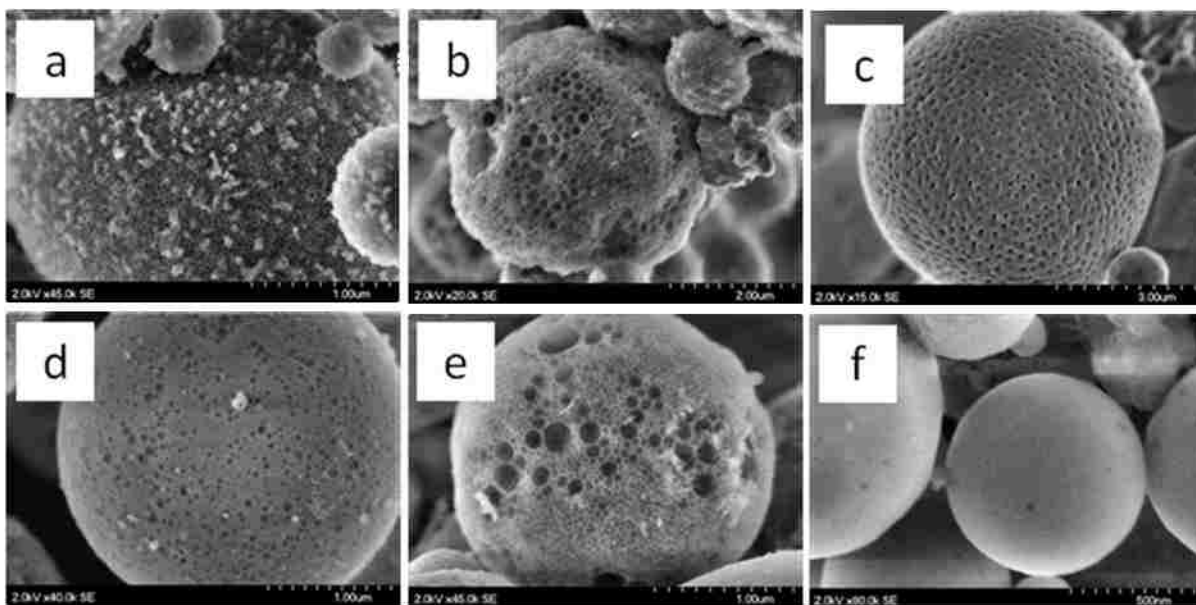


Figure 0.11. Different pore morphologies and particle surface areas created by varying microemulsion mixture components. Particles formed by: (a) Standard microemulsion mixture, BET surface area 1000 m²/g. (b) Adding 0.075 M NaCl, BET surface area 650 m²/g. (c) Adding 0.15 M NaCl, BET surface area 850 m²/g. (d) 2:1 oil to water ratio, BET surface area 1038 m²/g. (e) Reducing molar concentration of Abil EM-90 surfactant by 25%, BET surface area 975 m²/g. (f) Increasing mass of CTAB surfactant by 25%, BET surface area 1250 m²/g.

0.075 M and 0.15 M NaCl were added to the standard sol mixture and a variation from the standard ‘honeycomb’ morphology was observed (figure 3.11 b and c) with measured BET surface areas of 650 and 850 m²/g, respectively. Reducing sol to oil ratio (1:2) also altered the surface morphology (figure 3.11 d) with a measured surface area of 1038 m²/g. Reducing

the concentration of oil phase surfactant, Abil Em-90, by 25% produced particles with much larger surface cavities (figure 3.11 e) and a surface area of 975 m²/g. The larger surface cavities observed throughout the sample may be due to microemulsion emulsion coalescence related to lower emulsifying surfactant concentrations at elevated temperature. Increasing concentration of water-soluble surfactant CTAB gives particles with no observable surface cavities (figure 3.11 f) and a 25% increase in surface area over the standard surface area (1250 m²/g).

The importance of control over pore morphology via emulsion mixture variations is demonstrated in the section of these types of particles for use as drug delivery vehicles. Recently, Lui et al. [126] demonstrated that drugs could be loaded into mesoporous silica particles with controllable release by electrostatic fusion of liposomes to the surface. Such particles were named ‘protocells.’ The liposomes effectively prevent diffusion of the cargo from the silica particles until they become internalized by receptor-mediated endocytosis. Hierarchically porous materials are of interest for use as drug delivery vehicles due to their excellent transport properties and the ability to load larger molecular cargo, such as proteins, quantum dots, and DNA plasmids. Along with surface liposomes, proteins are fused to the surface to facilitate receptor-mediated entry into the cells. It was discovered that a key element in successful receptor/protocell interactions was the surface fluidity of the liposomes and surface proteins. As shown in the TEM micrograph of a standard microemulsion templated silica particle, (figure 3.12), the surface of the particles are rough and irregular with some protrusions of material adding to the rough surface morphology. Thus, it was determined that the standard microemulsion templated particles could not be modified for use

as drug-delivery protocells due to surface roughness leading to poor surface liposome/protein fluidity. A much smoother type of hierarchically porous silica can be obtained by addition of

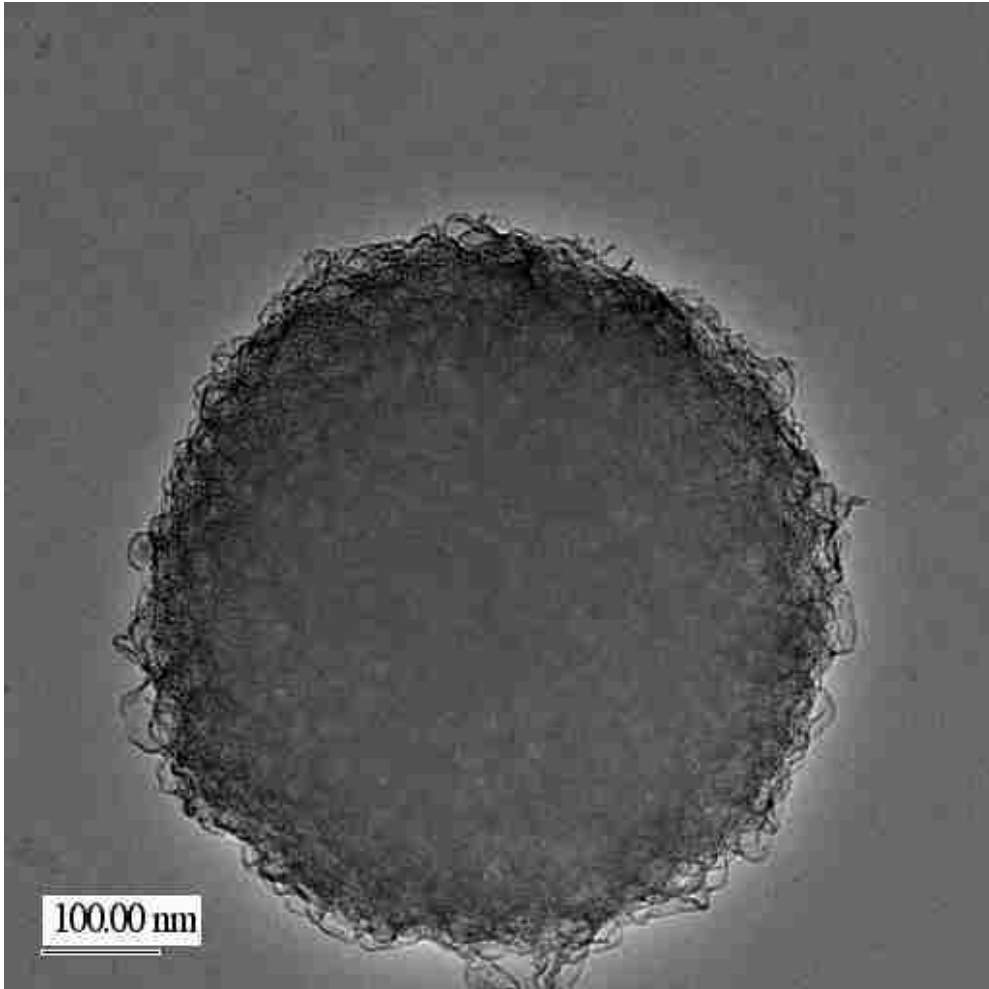


Figure 0.12. TEM of standard microemulsion templated silica. The rough surface of the particles prevents their use as drug-delivery ‘protocells.’

electrolytes (.015 M NaCl) to the emulsion mixture (figure 3.11 c). Addition of the electrolyte alters the microemulsion phase which templates a particle with a smooth surface. As the pore size distribution shows (figure 3.13) from the nitrogen sorption data, the particles

are multimodal with pores in the single nanometers coexisting with larger pores around 26 nm.

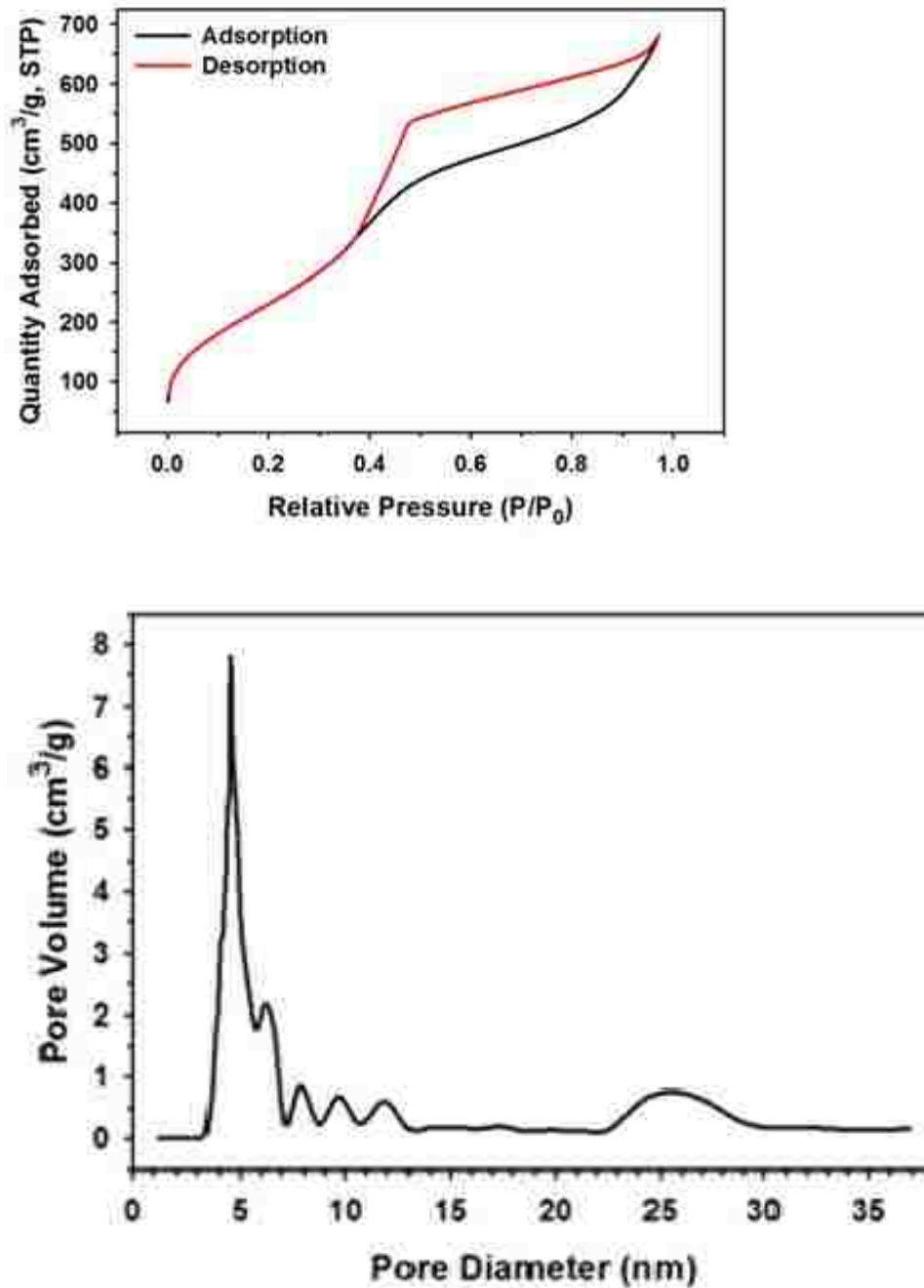


Figure 0.13. (top) Nitrogen isotherm and (bottom) Pore size distribution of multimodal silica particles.

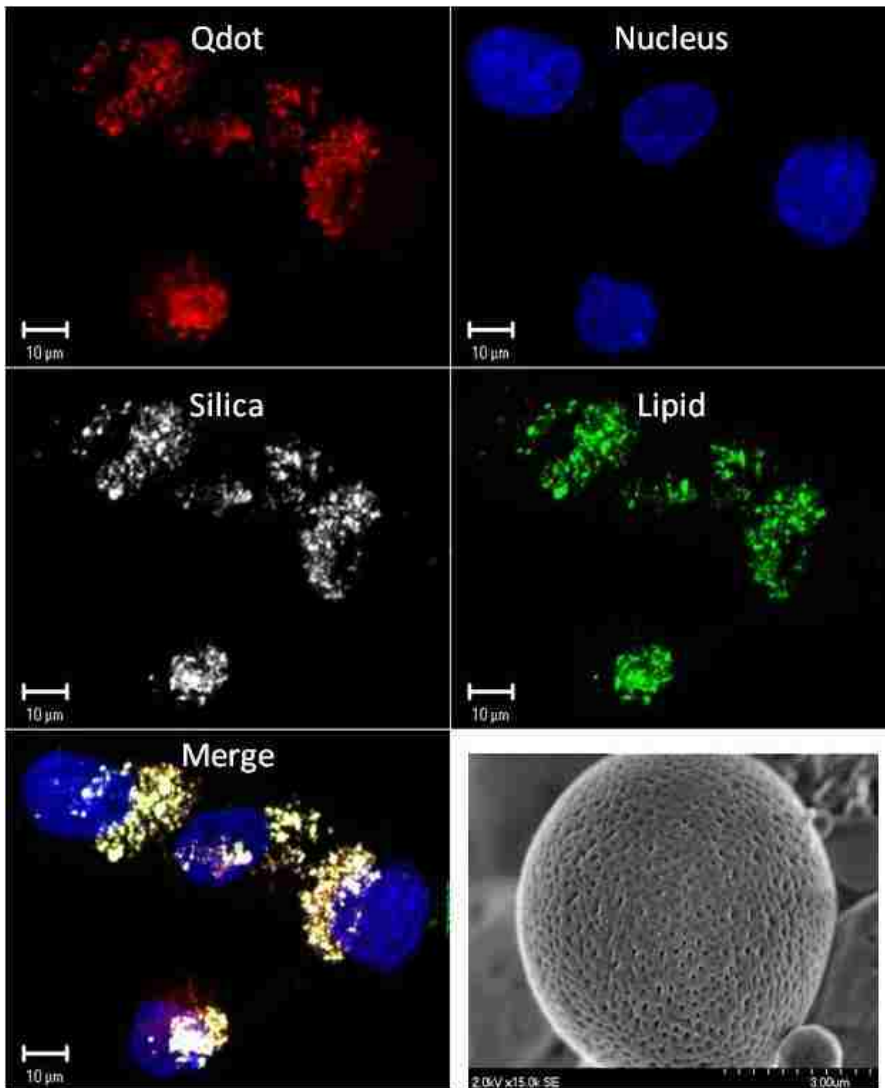


Figure 0.14. Multimodal silica particles used as drug delivery vehicles. Fluorescence imaging of liposome fused particles in cell nucleus, loaded with quantum dots [127].

The particles were loaded with fluorescent quantum dots and delivered to cells where they were taken up into the cell nucleus. Figure 3.14 shows fluorescent microscopy imaging of the quantum dots, liposomes, cell nucleus, and silica.

Practical application of nanostructured materials requires control of particle and pore morphology for different engineering situations. For the multimodal nanoporous particles presented herein, we have demonstrated that control over the microemulsion templated pores (10s of nms) can be achieved via variation of the microemulsion mixture components. While the microemulsion phase formation fossilized into the particles via gelation may not be at equilibrium, and may in fact be transient in nature, we have shown that these phases and the porous structures they template are reproducible.

Control at the length scale of tens of nanometers via microemulsion phase formation determines the morphology of the large pores as well as the surface morphology of the particles. However, in many engineering applications control over the size and distribution of the smaller, micelle templated pores can be the critical design feature. The state of the art electrocatalysts for fuel cell applications consist of noble metal particles supported on high surface carbon black. The support material allows for minimizing agglomeration and stabilizing high dispersion of particles. A goal in modern catalysis is to reduce the loading of noble metals while maintain a high surface area and activity. In this regard, control over the smaller micelle-templated pores is essential as the pore size distribution determines the size and distribution of noble metal (i.e. platinum) nanoparticles grown within mesoporous structures [128].

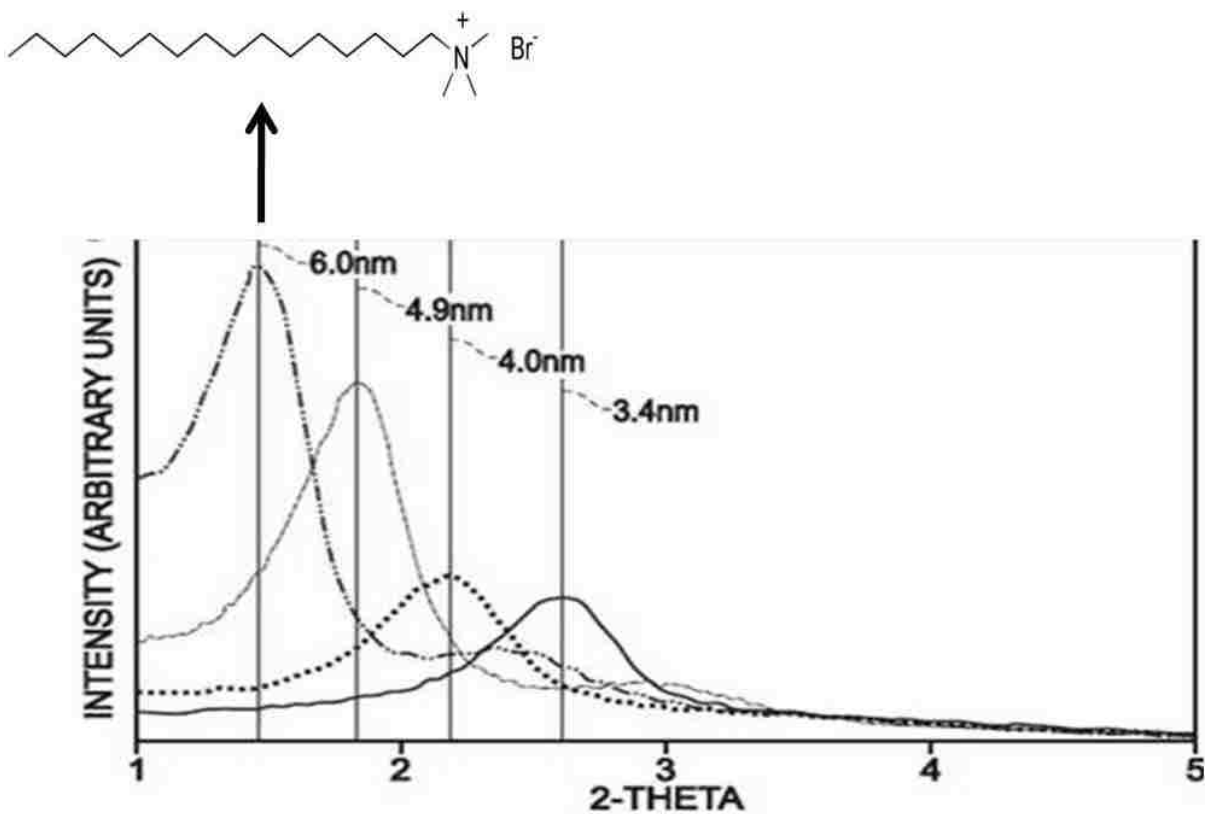


Figure 0.15. XRD data for mesoporous silica particles. The first peak is for the standard CTAB templating surfactant, with each subsequent peak representing material templated with a cationic trimethyl ammonium bromide surfactant each with progressively one less methyl group within the hydrophobic chain.

A study was conducted to determine if micelle-templated pore size could be controlled by reducing the length of the hydrocarbon block within the cationic trimethyl ammonium bromide surfactant while keeping surfactant concentration the same as the standard emulsion mixture. The XRD data shown in figure 3.15 shows that reducing the length of the hydrocarbon chain progressively by one methyl group produces porous structures of reduced size and d-spacing. While the smaller pore size distribution was altered by altering hydrophobic block length of the templating surfactant, there was no observed change in the morphology of the larger pores templated by the formation of the oil microemulsion phase.

The ability to reproducibly alter the liquid crystalline structures formed by surfactant micelle construction is another key element in providing design control for implementation of materials with complex hierarchical nanostructure.

3.7 Emulsion Aging/Surface Tension Studies

For each of the above emulsion evaporation particle synthesis, the emulsion solvent was evaporated immediately after emulsification. Thus, it is possible that the nanostructures obtained were templated by microemulsion phases not yet at thermodynamic equilibrium and the pore structures obtained were essentially ‘fossils’ or a ‘snapshot’ of a kinetically evolving microemulsion phase. The effect of aging the emulsion system was carried out by preparing a standard sol used previously in ‘standard’ bimodal porous silica particle synthesis and the corresponding hexadecane oil continuous phase. The mixture was emulsified by vigorous stirring. Immediately after emulsification ($t = 0$) a portion of the emulsion was removed and processed via EISA as previously reported to produce silica particles with bimodal nanoporosity. The silica particles formed exhibited cavities on the surface in a honey comb-like morphology as was expected (figure 3.16 a). The remaining emulsion was left undisturbed at ambient conditions and at $t = 3$ hrs another sample from the emulsion was removed and processed. SEM images of these particles (figure 3.16 b) indicated the presence of surface cavities, with cavities larger (50-100 nm) than those observed for the standard sample.

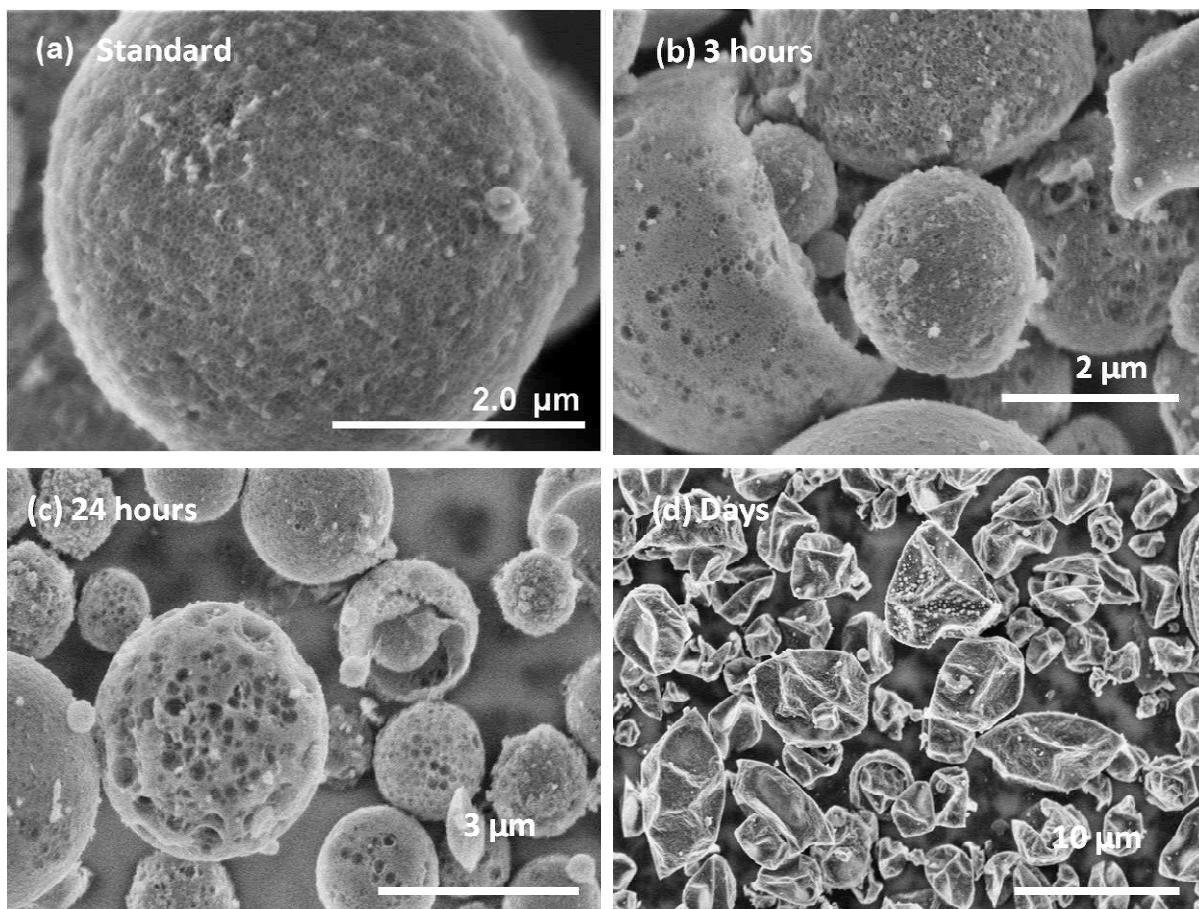


Figure 0.16. Silica particles formed after EISA processing of the emulsion after (a) $t = 0$; (b) $t = 3$ hrs; (c) $t = 24$ hrs; (d) $t = 3$ days.

At $t = 24$ hours another sample was removed from the emulsion and processed. Large (> 100 nm) surface cavities formed (figure 3.16 c) and with a greater frequency. Also observed were a much greater number of hollow or collapsed particles. Figure 3.16 d shows particles formed from the emulsion when processed 3 days after emulsification. The particles are not spherical and are irregular shaped.

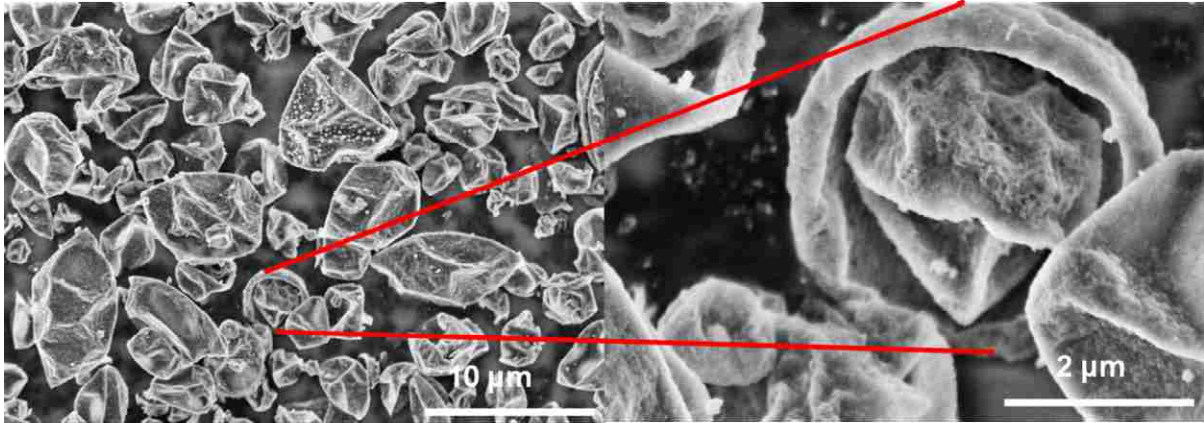


Figure 0.17. Silica particles processed 3 days after emulsification.

There were a large number of particles observed which were hollow (figure 3.17) and some particles had varying levels of surface porosity.

It is possible that the increase in surface cavity size distributions could be due to coalescence of oil microemulsion droplets as the emulsion is aged. Without evaporation induced gelation of the sol, the silicate hydrolysis and condensation reactions do not proceed to completion [129]. Instead, there exists a complex distribution of Q^0 (Si attached via oxygen links to no other Si species) through Q^4 species (Si attached via oxygen links to 4 other Si species). As time proceeds, there is a gradual decrease in the number of Q^0 , Q^1 , and Q^2 species and an increase in the number of Q^3 and Q^4 species. The organic silicate alkoxide monomer used in these experiments (TEOS) is initially insoluble in an aqueous solution. Under acid conditions, the hydrolysis of the alkoxy silane to the trialkoxy silanol $(RO)_3Si-OH$ is very rapid. We hypothesize that the trialkoxy silanol could be surface active (silanol groups as polar head) and adsorbing at the sol-oil interface, thereby contributing to the synergistic reduction of interfacial tension and subsequent formation and stabilization of the templating

oil microemulsion phase. To test this, a sol was prepared with TEOS, HCl, and water and was hydrolyzed for one hour.

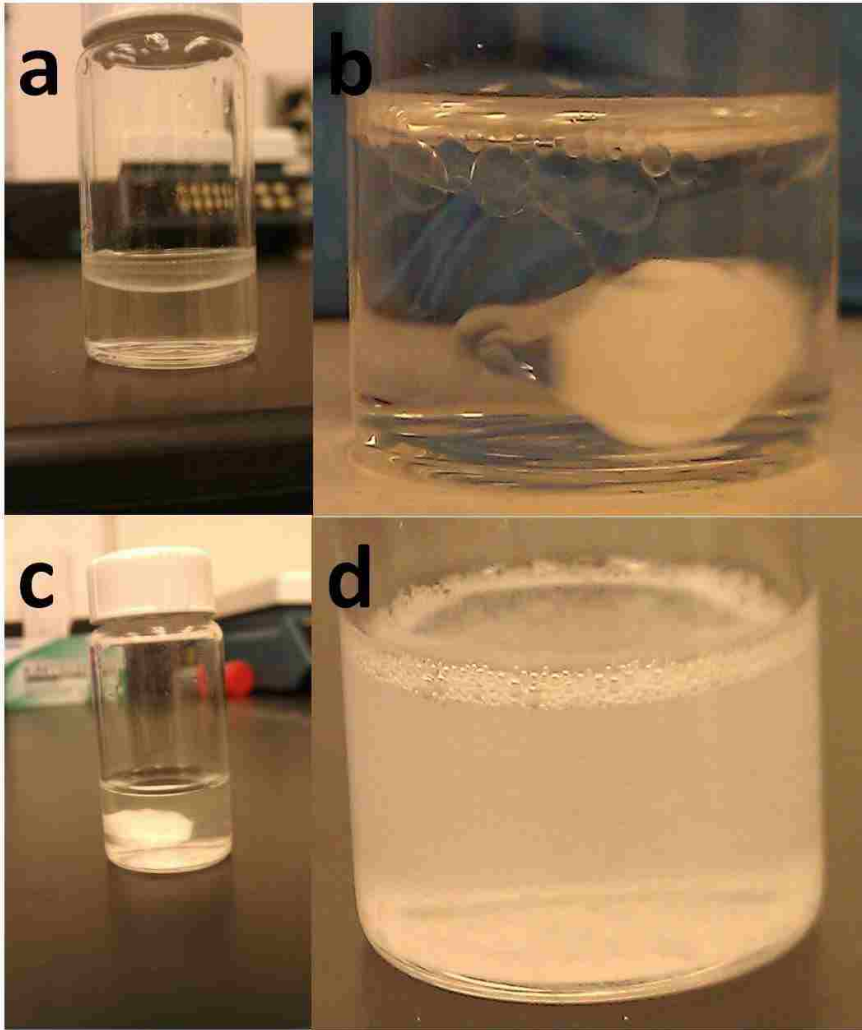


Figure 0.18. Complete phase separation is observed for Q0 organic TEOS in water and HCl (a) even under vigorous stirring (b). Upon hydrolysis, no phase separation is observed (c) and the solution foams upon shaking (d) indicating partially hydrolyzed TEOS is surface active.

Initially phase separation of the water and organic TEOS was observed, even under vigorous stirring (figure 3.18 a,b). After hydrolysis, the liquid was clear upon shaking but foamed

(figure 3.18 c,d), indicating a surface active species present. As the sol is aged and the trialkoxy silanol $(RO)_3Si-OH$ is additionally hydrolyzed or linked to additional Si species, and may lose effectiveness as a co-surfactant, leading to less stabilized oil microemulsion droplets. Surface tension measurements were taken of a water + HCl solution and compared

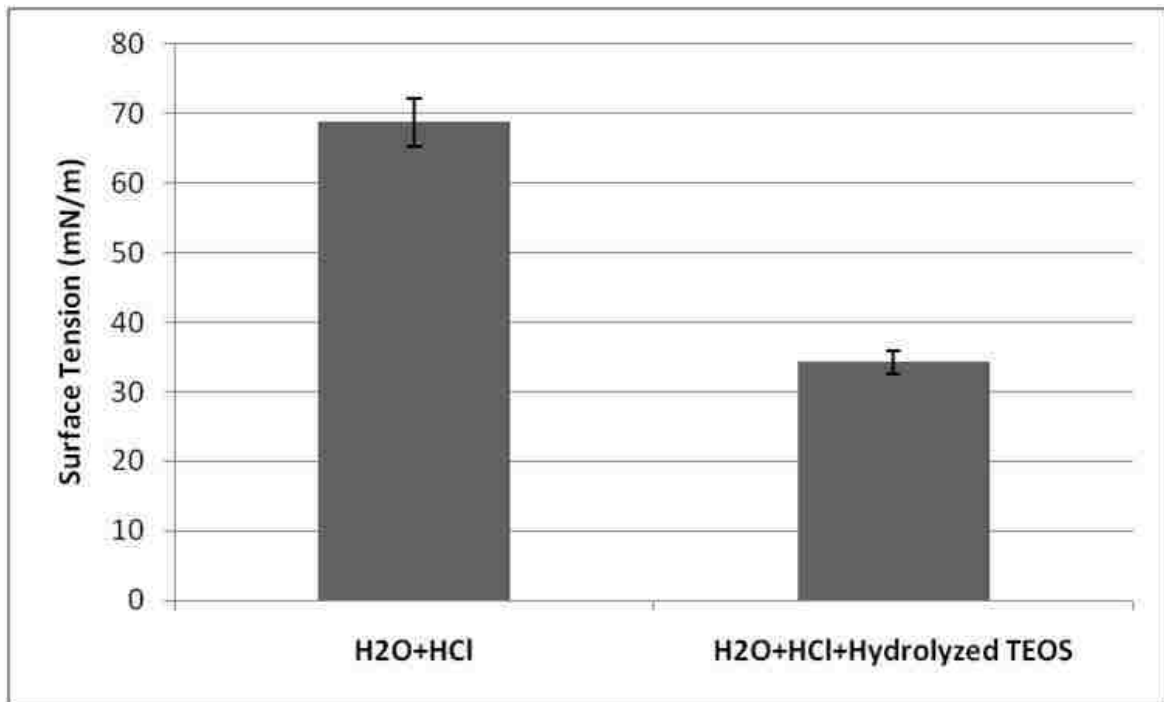


Figure 0.19. Surface tension measurements indicate hydrolyzed TEOS is surface active, lowering the measured surface tension of an H₂O+HCl solution from 69 mN/m to 34 mN/m.

to the surface tension of an aqueous H₂O + HCl solution with freshly hydrolyzed TEOS (figure 3.19). The measured surface tension was lowered from 69 mN/m to 34 mN/m with the addition of partially hydrolyzed TEOS, further suggesting surface activity.

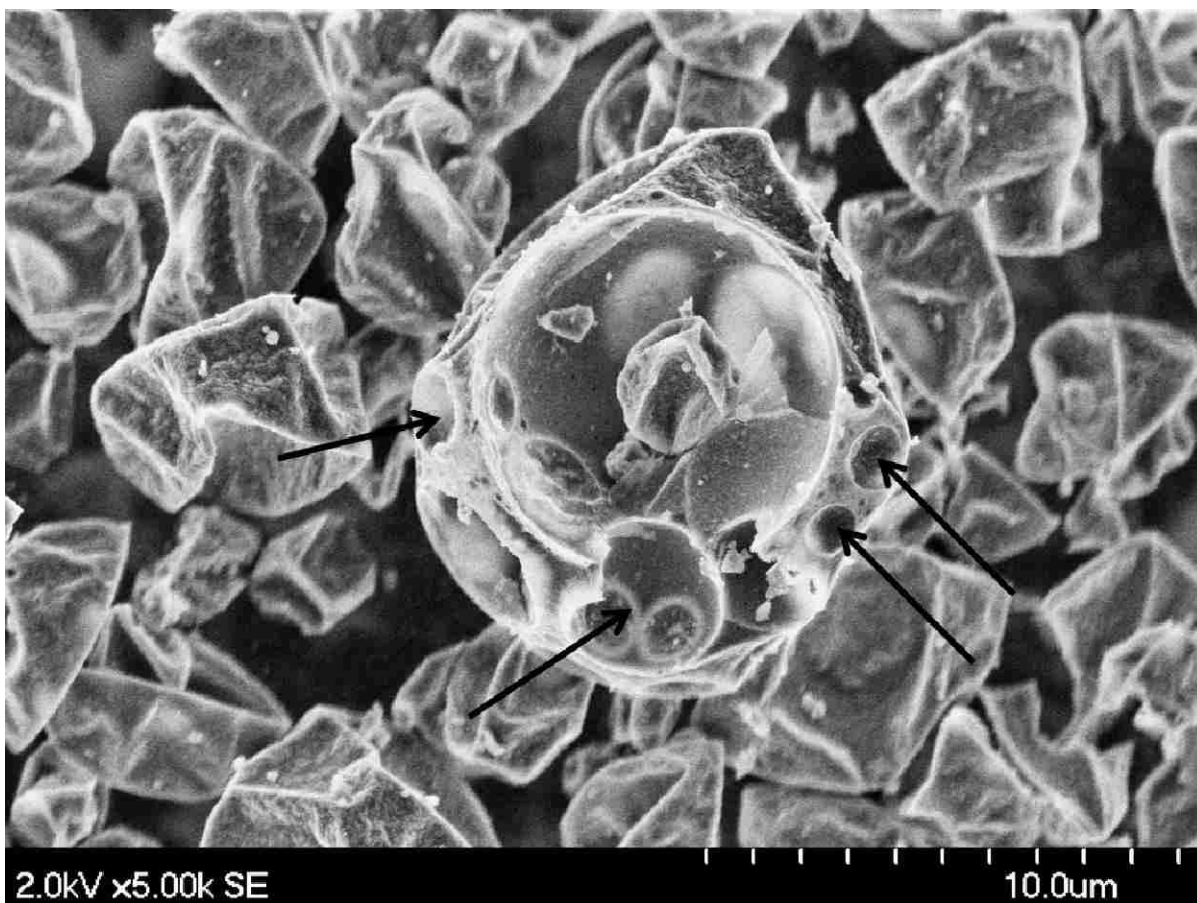


Figure 0.20. Particle from 3 day aged emulsion. Micron-sized cavities (arrows) ‘fossilized’ within the particles indicate possible oil droplet coalescence.

The decreasing surface activity of the hydrolyzed alkoxide monomers over time might produce a less stable microemulsion system and lead to a greater occurrence of oil microemulsion droplet coalescence, thus templating later surface pores. As shown in figure 3.20, large, micron-diameter spherical cavities were also observed within some particles formed from the 3 day old emulsion. The increase in microemulsion oil droplet coalescence within aqueous sol drops might also contribute to the increase in hollow particles observed in the aged samples.

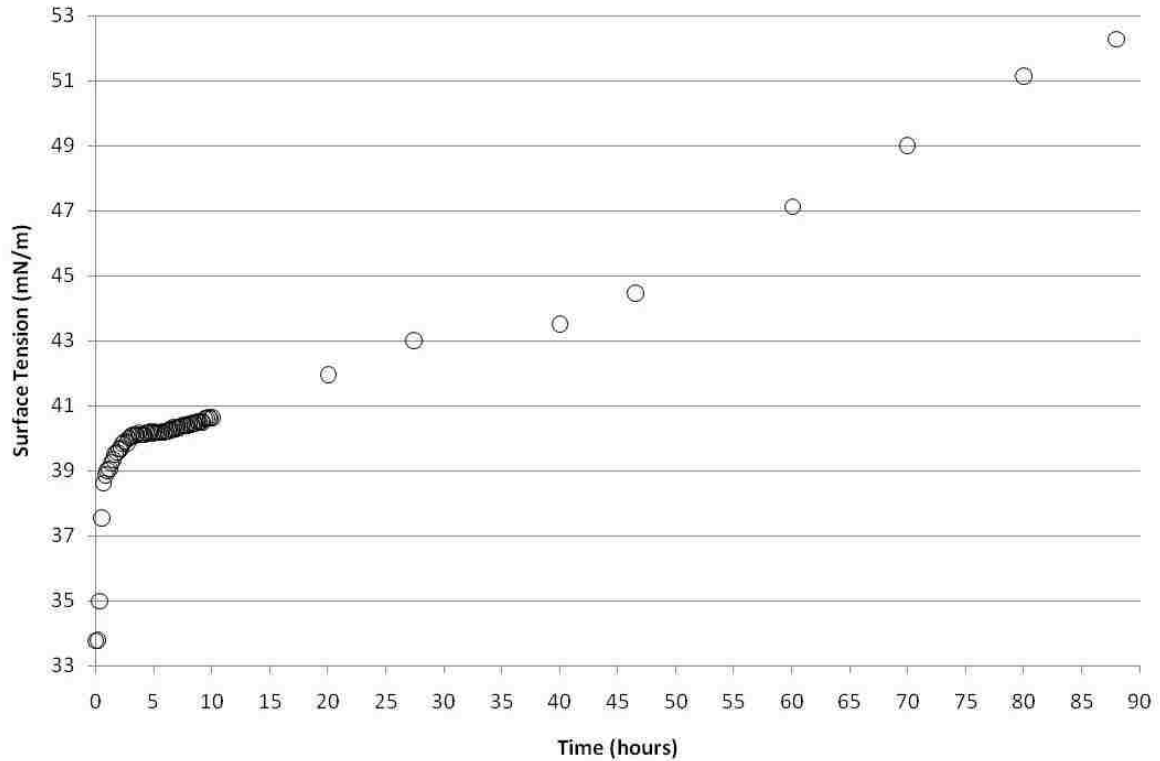


Figure 0.21. Surface tension of H₂O+HCl+TEOS solution evolving with time from t = 0 (initial hydrolysis) to 90 hours. The rapid increase in surface tension in the first few hours followed by a gradual increase over the next few days follows the trend of surface pore change observed from SEM images in figure 3.16.

Surface tension measurements were taken of an H₂O+HCl+TEOS solution from the moment TEOS is hydrolyzed and solubilized into the aqueous solution over a time period of ~ 90 hours (figure 3.21). A rapid increase in surface tension was observed over the first few hours followed by a continual, gradual increase in the measured surface tension values. This trend follows very closely the growth of surface pores observed in the SEM images of figure 3.16. A change in surface pore morphology is observed after only 3 hours of emulsion aging, slightly larger pores at 24 hours, until collapsed particles with little or no surface pores are observed after 3 days of emulsion aging. An increase of 7 mN/m is measured over the first 3

hours, an additional increase of ~ 2 mN/m at the 24 hour mark, and an additional increase of 7 mN/m at the 3 day mark, for a total increase of ~ 16 mN/m. It is yet inconclusive if the large surface pores and increase in hollow particles are a result of coalescing oil microemulsion droplets, and further studies (i.e. dynamic light scattering measurements) are needed to track the configurational changes of the microemulsion and micelle structures over time. It is, however, likely that the changing surface activity of TEOS is contributing to the time evolution of this complex microemulsion system.

Droplet-Based Microfluidics for Synthesis of Monodisperse Silica Particles with Multi-Modal Nanoporosity.

4.1 Introduction

Developing pathways for fabrication of monodisperse oxide particles with hierarchical internal nanoporous structure provides additional opportunities and level of complexity of material structural design. Same-size spherical microparticles are essential for developing novel families of functional digital inks for printing catalysts, current collectors, and creating polymer/oxide composites at the microscale.[70] Such inks are essential for miniaturization of devices for catalysis, sensing and detection, and microfuel cells. Manipulating the particle structure, pore morphology and surface chemistry allows for better control at the micro and nanoscale. Monodisperse spherical microparticles can be ordered in 2D and 3D arrays to create structures with hierarchical porosity. Such structures will exhibit a variety of characteristic pore dimensions: (i) nanoscale pores that are due to micelle (single nanometer) and microemulsion (tens of nanometers) templating and (ii) microscale pores determined by the voids between monodispers microparticles in the array.

Fabricating monodisperse emulsion drops is essential for obtaining monodisperse particles [130]. However this is not a trivial task [131-137]. The problem is resolved using the recent advancements in microfluidics that present powerful tools to generate such drops in a wide size range using pressure or an electric field [138-149]. This project utilizes the potential of

microfluidics to fabricate monodisperse emulsion drops, which will then be used for mesoporous silica particle synthesis.

Processing of oil/water/surfactant systems by microfluidics allows not only obtaining monodisperse drops (and hence particles) but enables a precise control of sol-gel chemistry.[130] Also certain combinations of surfactants, oil and water lead to formation of microemulsions instead of simple micelles. This presents an interesting and unexplored opportunity for microemulsion phase templating [109-112, 150-166] into the solidifying oxide particles. Similar approaches were used in the past to synthesize a variety of bulk monolith mesoporous oxide structures.[116, 117, 167-171] However, as mentioned above, fabricating monodisperse microparticles with designed mesoporous structure adds a level of complexity and opens new opportunities for applications. Also microemulsions are larger than pure surfactant micelles and thus offer different size scale for templating.

The ***objective*** of this project is to develop a method for fabrication of monodisperse mesoporous microparticles using microfluidics. The internal porous structure will be obtained by templating microemulsion and surfactant micelle phase structures. To avoid confusion throughout the present text we define

- ***Microparticle:*** A particle with size between a few micrometers and a few tens of micrometers. These are fabricated using microfluidic approach.
- ***Microemulsions:*** Microemulsions are water/oil/surfactant mixtures which under certain conditions may form various thermodynamically stable phases. Examples are water droplets in oil, oil droplets in water and middle bicontinuous phase.[172, 173] These phases may also be coexistent. The name *microemulsion* is historically established. It

implies *micro* dimensions. In fact the typical length-scale of the microemulsions structures (e.g. the droplets) is usually about a few tens of nanometers. For comparison pure surfactant micelles are normally below 10 nm.

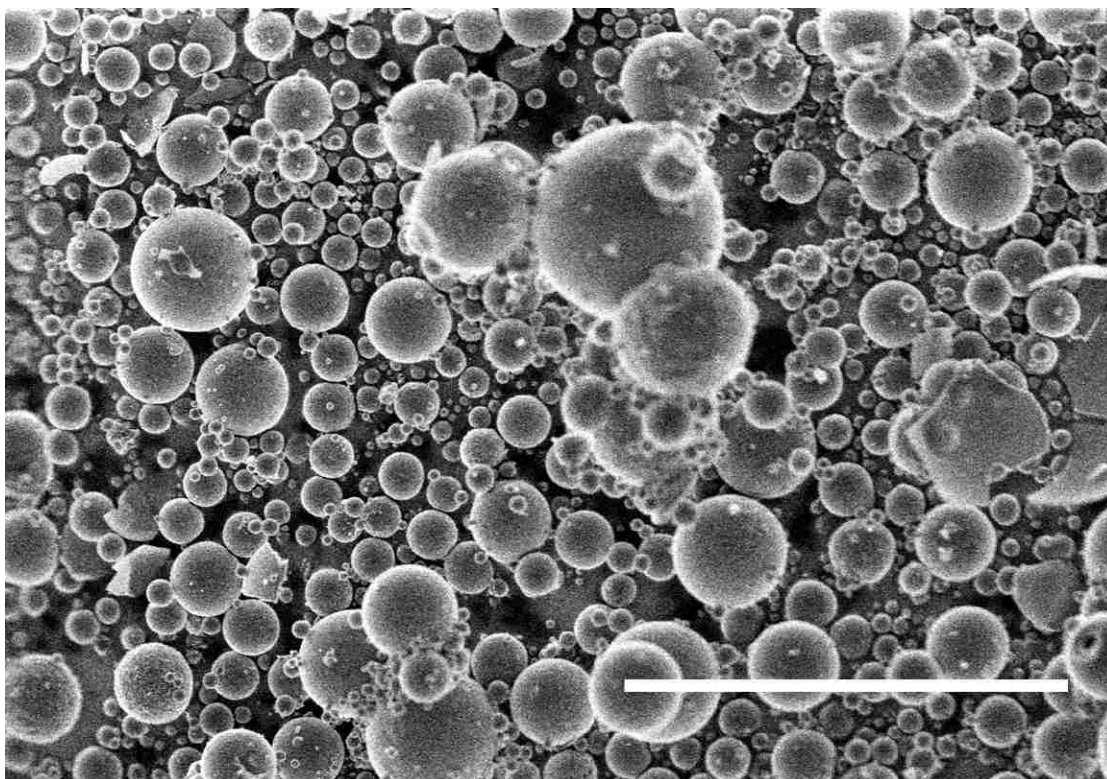


Figure 0.1. Polydisperse silica particles with bimodal nanoporosity. The emulsions were prepared in bulk using inhomogeneous vigorous stirring. As a result, the droplets, and therefore the particles, were produced with a broad size distribution. (Scale bar is 20 μm).

The main focus is to develop a microfluidic methodology for synthesis of monodisperse mesoporous oxide particles using microemulsion [116, 117, 168-170, 174] and surfactant [88, 113] templating. We have published experiments to synthesize hierarchically nanostructured silica particles using a bulk emulsion (in a vial, using a stirrer) [125]. This

approach cannot provide monodisperse microspheres but facilitated the formation of silica microparticles with hierarchical pore size distribution (figure 4.1).

The *engineering goal* of this project is:

To develop new techniques for fluidic-based monodisperse particle synthesis and fabrication of ordered structures with hierarchical porosity.

The working *hypothesis* is that when an aqueous silica precursor solution drops form in a microfluidic device, the surrounding oil phase will spontaneously penetrate and form a microemulsion phase inside them. This is facilitated by the specifically selected combination of surfactants that are present in both oil and water phases and significantly reduce the interfacial tension [125].

4.2 Experimental Methods

The aqueous silica precursor solution was prepared by dissolving 0.455 g of CTAB in 5 g of deionized water with stirring at 40° C for 15 minutes. 0.14 g of HCl and 1.3 g of TEOS was added to the solution and was hydrolyzed at room temperature for one hour under vigorous stirring. The continuous phase was prepared by dissolving ABIL EM 90 (Degussa) surfactant in hexadecane (2 wt %). The low interfacial tension necessary for the formation of a microemulsion within the aqueous silica precursor phase makes integration of microdroplet formation within a microfluidic device problematic. This is demonstrated by the characteristic time (τ) to reach capillary instability [175]:

$$\tau \approx \frac{\mu r}{\gamma} \quad (4.1)$$

where μ is fluid stream viscosity. Thus as interfacial tension (γ) approaches zero, the time for thread instability and breakage within the microfluidic orifice approaches infinity. To circumvent this problem, as shown in figure 4.2, the aqueous silica precursor (1) is emulsified in a 10 μm -diameter orifice with pure hexadecane oil (2,3). The droplets travel downstream with oil between them to prevent interaction and coalescence. Next, hexadecane with 2 wt% Abil EM90 surfactant (4,5) is added allowing the microemulsion phase to form and penetrate the aqueous silica precursor droplets (6). The droplets are collected in a large (6 mm diameter) reservoir (7) where the solvent is evaporated out of the silica precursor drops at ambient temperature and pressure to induce gelation and surfactant self assembly [88, 113, 125].

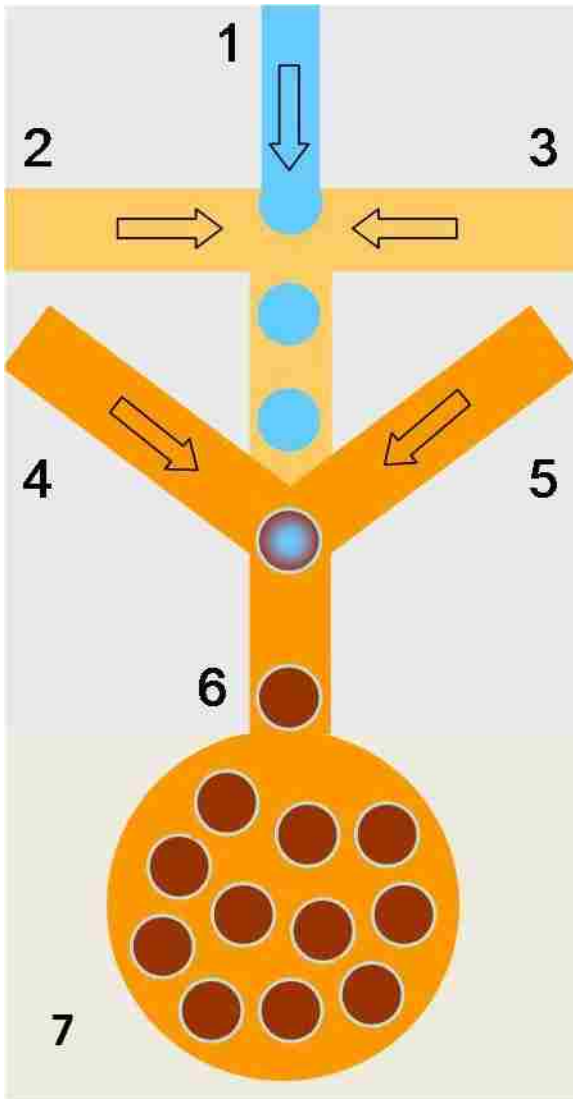


Figure 0.2 Microfluidic configuration. Aqueous silica precursor (1) is emulsified in a 10 μm diameter orifice with pure hexadecane oil (2,3). Droplets travel down the 10 μm diameter channel where hexadecane with 2 wt% Abil EM90 surfactant (4,5) is added allowing the microemulsion phase to form and penetrate the aqueous silica precursor droplets (6). The droplets are collected in a reservoir (6 mm diameter) where EISA is carried out at ambient pressure and temperature.

4.3 Results/Discussion

In our previous microemulsion-templated silica particle synthesis experiments [176], emulsion evaporation was carried out at an elevated temperature of 80 °C under vacuum pressure. Vigorous bubbling was observed during the evaporation process. It was necessary to avoid vigorous bubbling of the emulsion during the processing of monodisperse silica precursor droplets as this led to shearing of the droplets prior to gelation and thus a disruption of the narrow size distribution. The issue of droplet disruption during evaporation was further exacerbated by the low interfacial tension of the system, in which droplets are easily deformable due to low interfacial tension and small Laplace pressure (ΔP_L):

$$\Delta P_L = \frac{2\gamma}{r}, \quad (4.2)$$

where r is the spherical droplet radius and γ is the interfacial tension. Orifice diameter is the primary parameter in determining the size of droplets formed in the microfluidic device [19]. To maximize ΔP_L , we form droplets in the smallest orifice diameter possible (10 μm), limited by the resolution of the printer used to produce the soft lithography photo masks.

Emulsion evaporation was carried out at room temperature to avoid vigorous bubbling and droplet disruption. Aranberri [177] and coworkers determined that emulsion droplet evaporation occurs via a mechanism where the droplets remain separated from the vapor phase by a liquid continuous phase and transport from the droplets to the vapor occurs by

diffusion of dissolved molecules through the surrounding continuous phase. It was determined a factor f , with values between 0 and 1 represents the factor by which the rate of evaporation of emulsion droplets is reduced below that for the pure fluid, and correlates with the solubility of the fluid in the continuous phase. The flux J across the continuous phase is related to the linear concentration gradient:

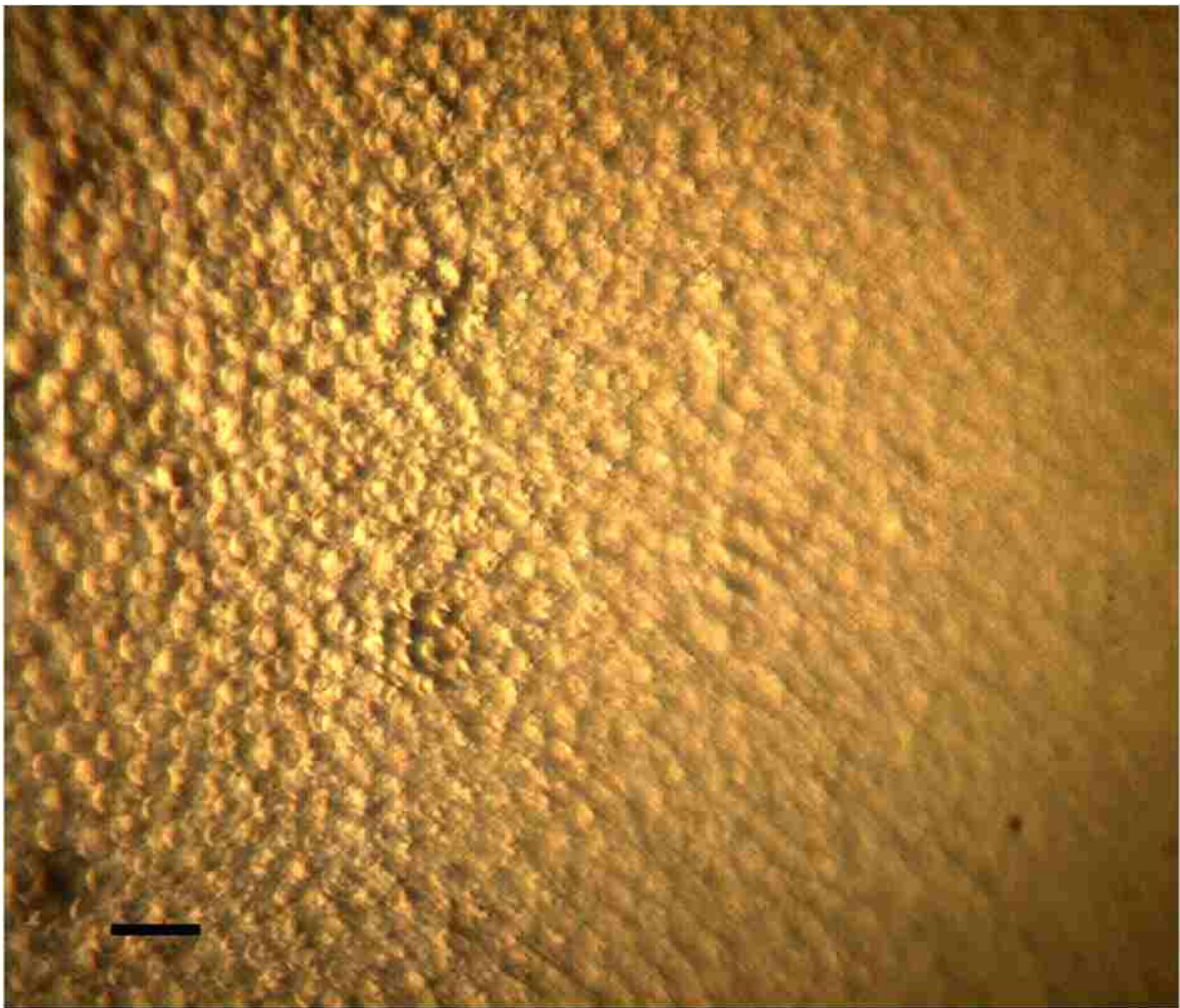


Figure 0.3. Aqueous silica precursor droplets in hexadecane oil phase. Opaqueness is observed in the continuous phase near the droplets (Scale bar 20 μm).

$$J = D_w \frac{C_s - C_I}{d}, \quad (4.3)$$

where D_w is the diffusion coefficient of droplet solvent in the continuous phase, C_s is the equilibrium solubility of the droplet fluid and the concentration at the droplet surface, C_I is the concentration of droplet solvent at the continuous phase/vapor interface, and d is the



Figure 0.4. Silica particles in hexadecane oil phase after evaporative processing. (Scale bar is 15 μm).

thickness of the continuous phase film. To increase flux of the droplet solvent, most of the hexadecane oil phase was pipetted and removed from the reservoir until only a thin film remained above the gravity-settled aqueous silica precursor droplets.

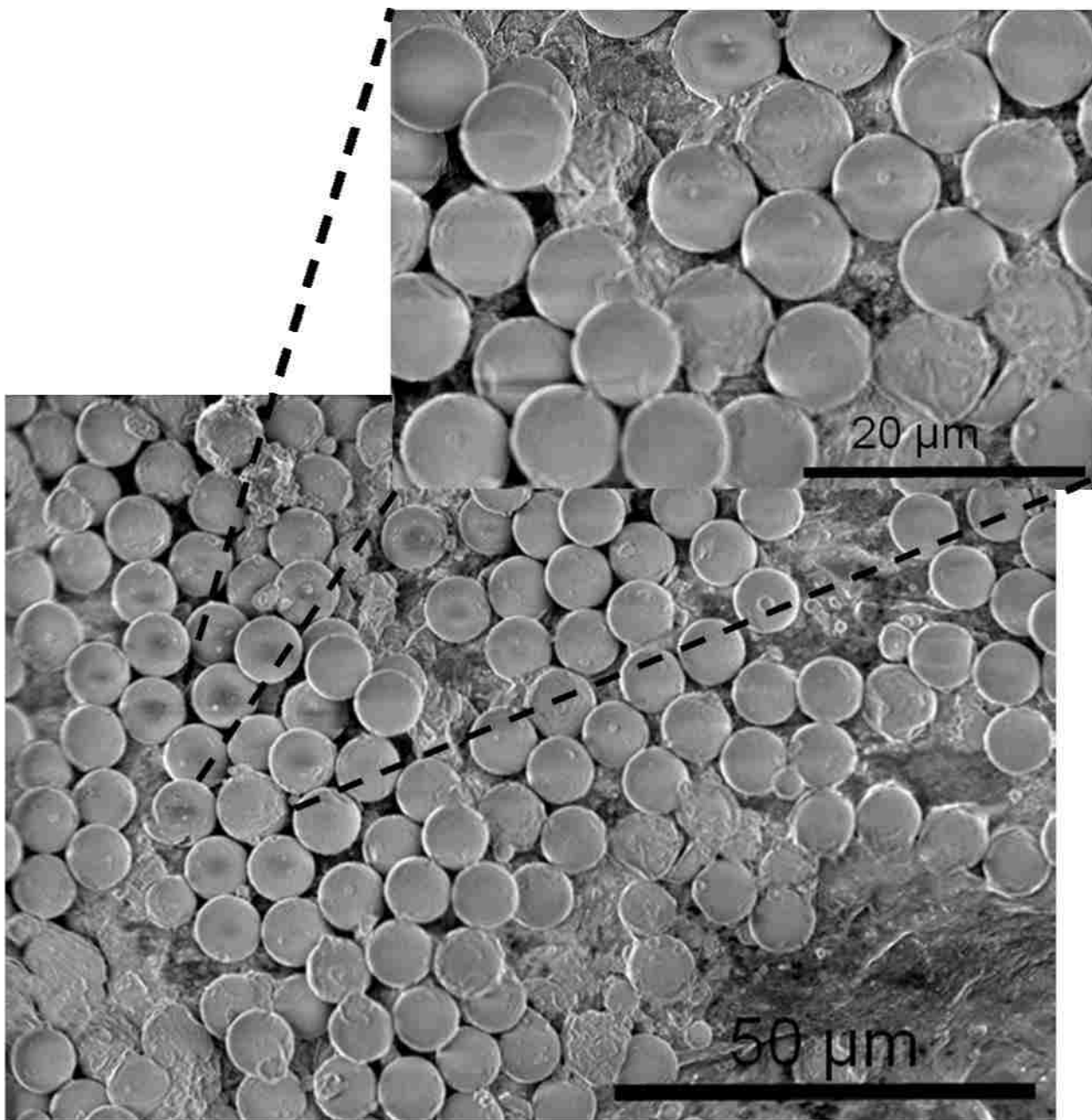


Figure 0.5. SEM image of monodisperse microemulsion-templated silica particles.

A decrease in the continuous oil phase layer from 1 cm to 1 μm would lead to a 10^4 fold increase in flux through the continuous phase.

Figure 4.3 shows the silica precursor droplets as imaged in the collection reservoir.

Opaqueness formed in the continuous phase near the droplets, which made imaging of the droplets difficult. This was also observed in previous experiments with this system using a bulk emulsion [176].

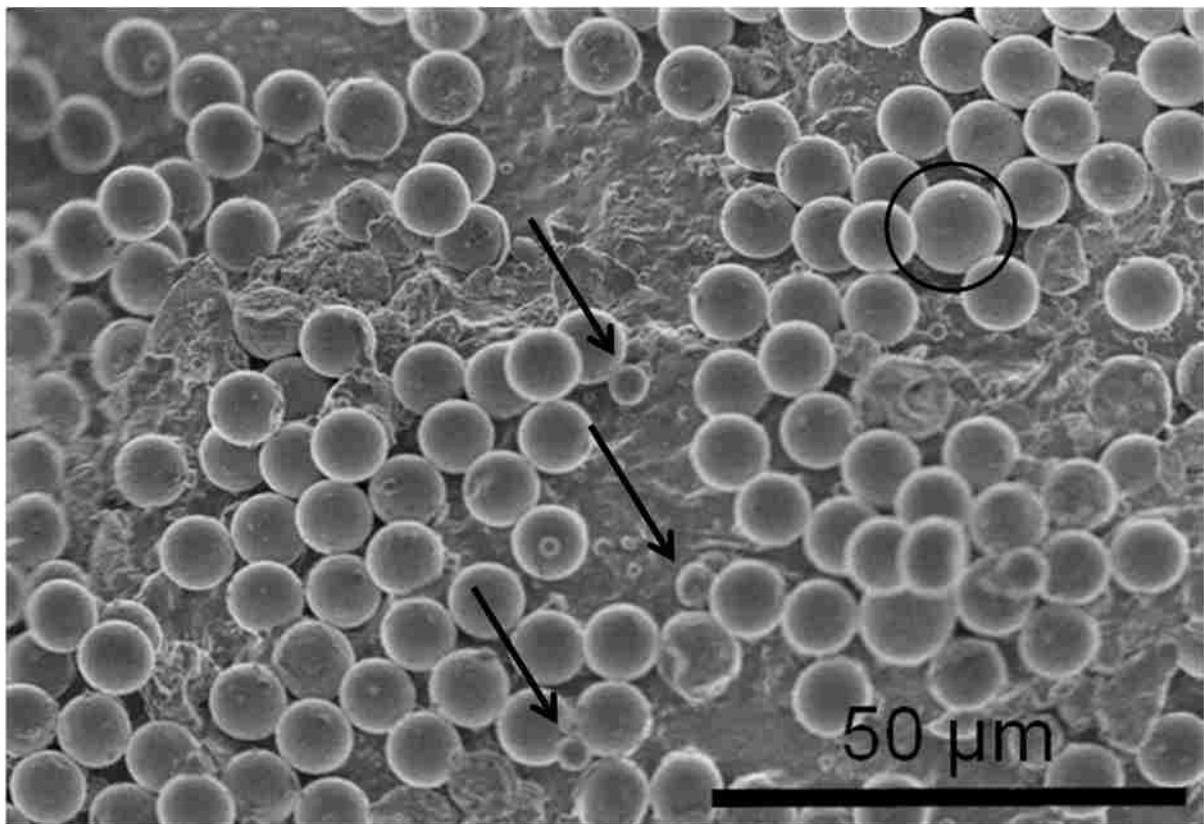


Figure 0.6. SEM micrograph shows existence of smaller particles due to satellite droplet formation (arrows) and large particles due to droplet coalescence (circle).

Figure 4.4 shows the processed silica particles in hexadecane within the collection reservoir following evaporative processing. Particle diameter is $\sim 7 \mu\text{m}$; the particles are smaller than the precursor drops ($10 \mu\text{m}$ diameter) due to loss of solvent during evaporative processing.

Following washing of the particles with hexane and drying, the particles are imaged via SEM (figure 4.5). Smaller ($1\text{-}2 \mu\text{m}$ diameter) particles are observed throughout the sample (arrows figure 4.6). These smaller particles are attributed to the formation of satellite drops during emulsification in the microfluidic orifice [19]. Some larger particles were observed in the sample, most likely due to coalescence of droplets (circled particle, figure 4.6).

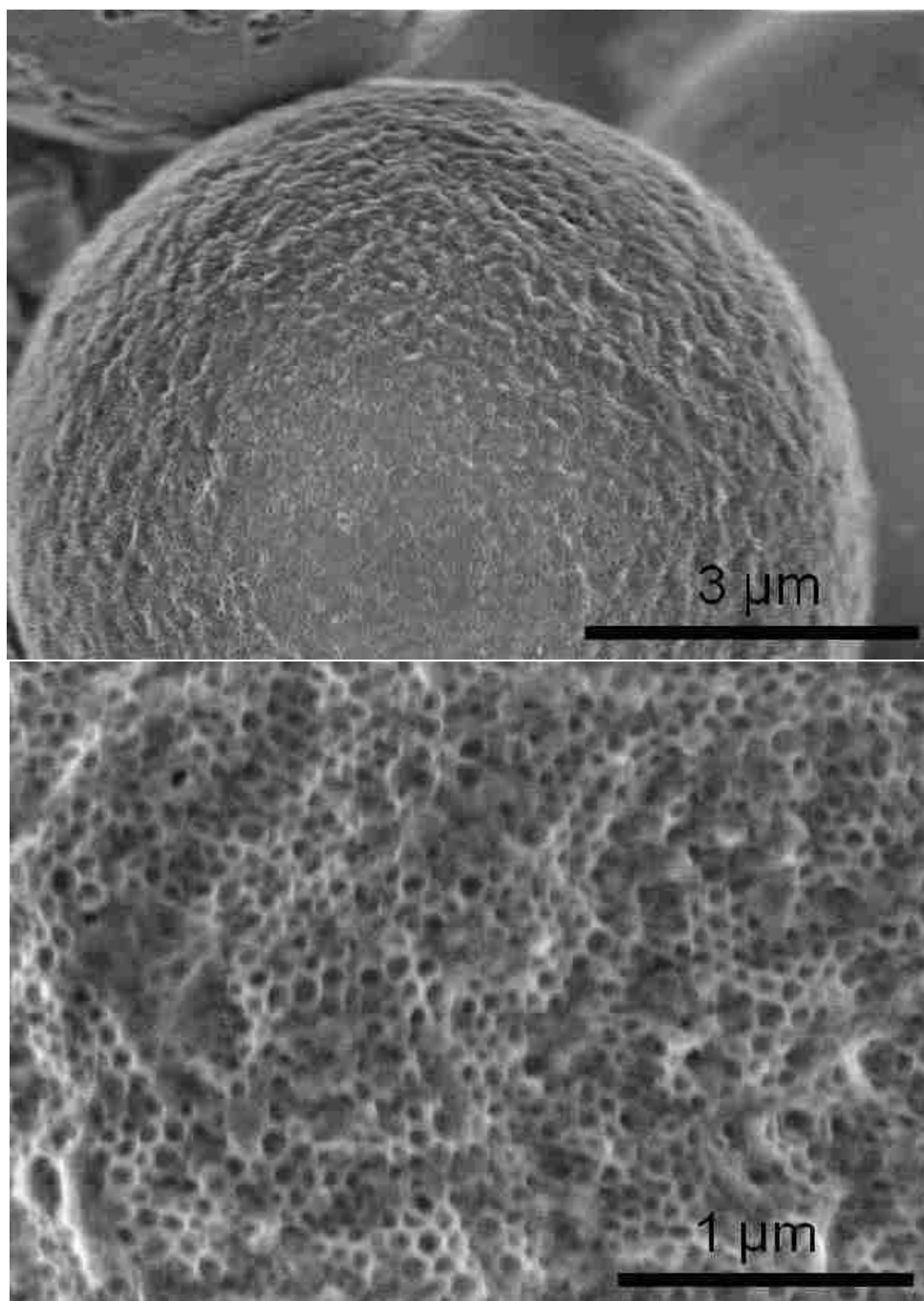


Figure 0.7. SEM micrograph showing surface morphology of microemulsion templated particles. Surface cavities are ~ 40 nm in diameter as was observed in previous synthesis experiments using a bulk emulsion system [125].

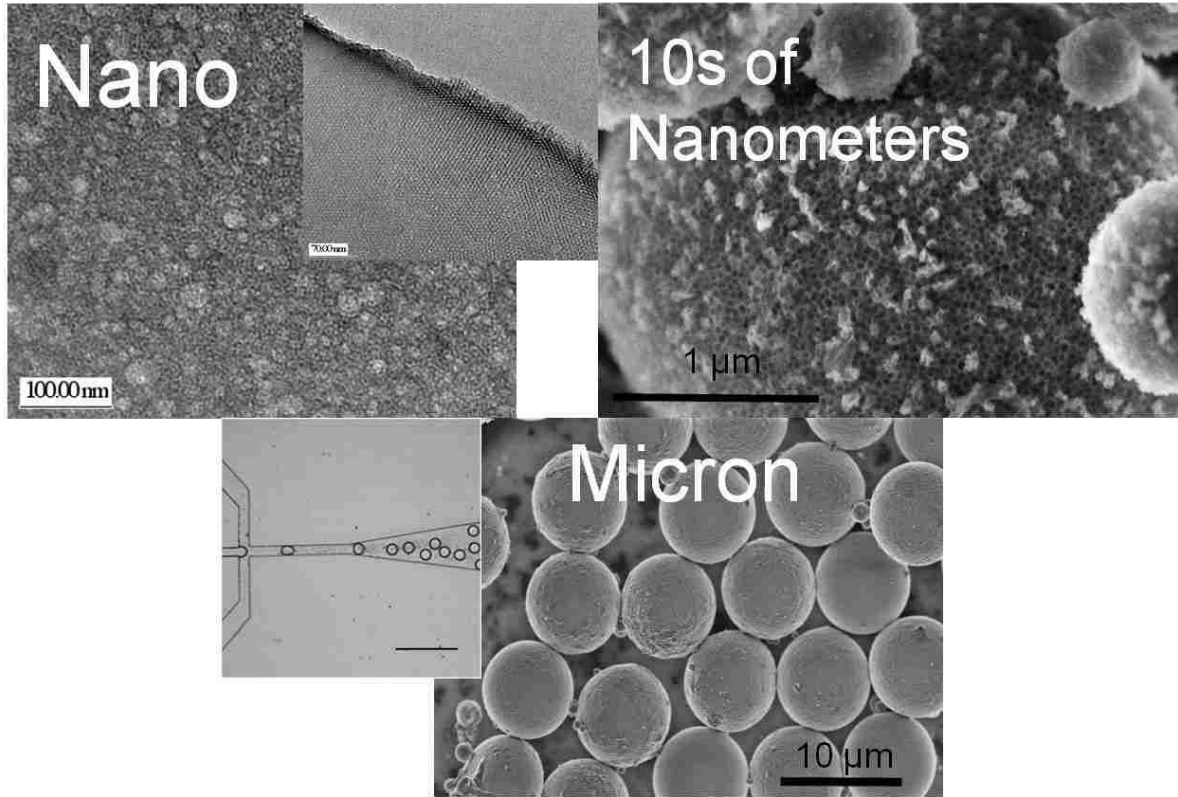


Figure 0.8. Successful synthesis of monodisperse silica particles with bimodal nanoporosity demonstrates control at three different length scales: the nanoscale via surfactant molecular templating, 10s of nanometers length scale via spontaneous microemulsion templating, and at the micron level through control of overall size distribution through microfluidic platform.

The obtained silica particles exhibit a honeycomb-like structure observed by scanning electron microscopy (SEM) (Figure 4.7), which shows the presence of cavities at the surface with diameters about 40 nm. This is in excellent agreement with the surface morphology observed in the original microemulsion-templated silica particle synthesis from a bulk emulsion system [176].

4.4 Conclusion

Developing pathways for fabrication of monodisperse oxide particles with hierarchical internal nanoporous structure provides additional opportunities and level of complexity of material structural design. The synthesis of monodisperse silica particles with bimodal nanoporosity offers the possibility for a third level of porosity associated with the void spaces between microspheres. Emulsification of silica precursor in a pure oil phase at the microfluidic orifice, with infusion of surfactant-laden oil phase into the device downstream of the orifice, allows for successful fluidic treatment of a low interfacial tension system and the formation of monodisperse particles. Temperate evaporation of the solvent from the droplets at ambient conditions preserves the excellent size distribution of the fluidic-formed precursor droplets during gelation. Successful synthesis of monodisperse silica particles with bimodal nanoporosity demonstrates control at three different length scales: the nanoscale via surfactant molecular templating, length scale in the tens of nanometers via spontaneous microemulsion templating and at the micron level through control of overall size distribution through microfluidic platform.

Templated Platinum/Carbon Oxygen Reduction Fuel Cell Electrocatalysts

5.1 Introduction

The importance of alternative energy is a well recognized problem drawing unprecedented attention to research focused towards renewable energy sources. Fuel cell research is yet to grow to be fuel cell technology that is commercially available and affordable. Even though there is no ready solution, directions that fuel cell research should focus on are well understood. First of all, cost of fuel cells, and therefore electrocatalytic materials have to be reduced. The major research thrust here is advancing currently existing platinum-based materials and lowering loading of precious metals by bringing their utilization to higher levels. Progress was made by alloying platinum with another transition metal [103, 178-180], and more recent, “de-alloying” of platinum-based alloys [181, 182]. Advantages of platinum monolayer [183] and nanostructured thin films [184] approaches were also demonstrated. Materials based on non-precious metals are another thrust area that can effectively solve cost and supply limitations if their catalytic activity reaches that of precious electrocatalysts [185]. While improving electrocatalysts and electrocatalytic layers and developing new materials is of superior importance, one should always recognize the significance of the issues associated with the durability of fuel cells. Among factor effecting lifetime of fuel cell

operation, dissolution and sintering of platinum particles and corrosion of carbon support are the ones that most closely related to the properties of electrocatalytic material itself [186].

A number of limiting parameters, including utilization of the catalyst and corrosion resistance, are strongly affected by the support material. Typically, state of the art electrocatalyst are supported on high surface area carbon blacks. More recently, advances made in the synthesis of high surface area porous carbons [187-189] lead to their further exploration as supports. Applications in catalysis and electrocatalysis require porous structures where both surface area and transport properties are maximized. Micropores can lead to a better dispersion, however their accessibility is very limited. Addition of mesopores, on the other hand can provide an enhancement in the transport by preserving high surface area necessary to provide efficient dispersion of the precious metal phase. Joo et al have reported a procedure that utilizes templating of the ordered mesoporous silica with carbon precursors resulting in an ordered carbon that allows to achieve high dispersions of platinum particles [119]. Following this report a number of publications have centered around the optimization of synthesis of ordered nanoporous carbon [187-195]. Though high-dispersions of platinum nanophase were shown, performance of electrocatalysts supported on this class of carbon was limited.

Previously, we have exemplified a number of materials obtained through templating with fumed silica and colloidal silica particles. These include non-platinum electrocatalysts, derived from cobalt and iron porphyrins [128, 196-202] and platinum-alloy-based electrooxidation catalysts [203]. Recently we have reported on the synthesis of silica particles with bimodal pore sizes obtained through simultaneous templating with

microemulsion droplets and micelles and demonstrated their use as templates for the synthesis of platinum-based carbon-supported electrocatalysts [176]. Here, we present a systematic study focused on the synthesis and optimization of this new class of electrocatalysts and investigation of oxygen reduction reaction (ORR) activity, including testing in single MEA fuel cell.

5.2 Experimental Methods

Synthesis of the bimodal porous silica particles that are utilized as the catalyst template was described in our earlier report [176]. Tetraethylorthosilicate (TEOS, Purum > 98%) was used as silica precursor. Cetyltrimethylammonium bromide (CTAB) and modified polyetherpolysiloxane/ dimethicone copolyol (ABIL EM 90, Degussa) were employed respectively as water and oil phase surfactants. The particles of this material, characterized by bi-modal pore size distribution (bi-porous silica), were impregnated with carbon and platinum precursor solutions using dry impregnation. The 1st generation (GEN1) of catalyst materials were synthesized as follows. Solution of carbon precursor was prepared by dissolving sucrose (EMD Chemicals Inc.) in 2 M H₂SO₄ and then adding acetone. Platinum precursor, H₂PtCl₆·6H₂O (Sigma-Aldrich) was also dissolved in 2 M H₂SO₄ and mixed with acetone. The loading of platinum varied from 10 to 30 wt%, and the calculation was based on the amount of carbon left after sucrose is decomposed. Silica was impregnated with carbon precursor, and after drying in oven at 70 °C overnight with platinum precursor. In the synthesis of 2nd generation (GEN2) of electrocatalysts, silica was impregnated with carbon precursor, dried in the oven at 100 °C for 30 minutes, then heat-treated at 150 °C for

1 hour, and finally, impregnated with platinum precursor. Materials were then pyrolyzed in N₂ atmosphere for 4 h, with the ramp rate at 3 °C per min at temperatures ranging from 500 to 1000 °C. To remove the silica template, powder after pyrolysis was soaked in 6 M KOH solution for 4 days, filtered, washed with DI water and dried in the oven at 70 °C. The catalyst was also prepared in the following order: impregnation with sucrose precursor, pyrolysis, impregnation with platinum precursor, reduction in N₂/10% H₂ atmosphere for 2 hours with ramp rate at 3 °C per min at 200 °C and finally, KOH etch.

Scanning electron microscopy (SEM) was performed on a Hitachi S-800 instrument and transmission electron microscopy (TEM) was conducted on JEOL 2010 and 2010F instruments. Brunauer-Emmett-Teller (BET) surface area was determined from nitrogen adsorption/desorption measurements performed on a Quantochrome Autosorb-I-MP instrument. Prior to analysis, samples were outgassed overnight at 120 °C. X-ray photoelectron spectroscopy (XPS) analysis was done using Kratos Axis Ultra XPS with a monochromatic Al K α source operated at 300 W. XPS data was processed using CasaXPS software. The X-ray powder diffraction (XRD) patterns were obtained on a Scintag diffractometer (CuK radiation).

Electrochemical characterization was carried out on a Pine Instruments AFCBP1 potentiostat in rotating disk electrode (RDE) configuration. Electrocatalyst solutions were prepared using a mixture of DI water, isopropanol (IPA) and Nafion® solution (5 wt% Nafion®, dilution of 1:10). A thin film was formed on the glassy-carbon electrode with area of 0.169 cm² by applying 10-30 μ l from 1 mg/ml ink solution. Cyclic voltammograms were obtained in 0.1M HClO₄ at room temperature using Pt counter and Ag/AgCl reference electrodes.

Single MEA testing was done on a Fuel Cell Technologies, Inc. fuel cell test station using a 5 cm² cell with serpentine flow channel. The anode ink was made by mixing and then sonicating following: 22.5 mg platinum black (Aldrich), 800 mg DI water, 50 mg of 5% Nafion® solution and 100 ml isopropanol. The cathode ink was prepared in the following way. First, Teflon modified carbon black composite (designated here as “XC-35”) is dispersed in the 500 ml of DI water and 200 mg of IPA by sonication. Then 10 mg of electrocatalyst (GEN2 10 wt% Pt/TC – platinum supported on templated catalyst), 151.2 mg of 5 wt% Nafion® solution, 500 mg DI water and 400 mg of IPA are added to the dispersion of XC-35 and sonicated. XC-35 carbon black contains about 35 wt% of Teflon and was prepared by a procedure in which PTFE30 (DuPont) and Vulcan XC-72 (Cabot) are mixed. Anode ink solution is hand painted onto Nafion® membrane (N1135, Ion Power, Inc) placed on a vacuum table at 70 °C. About 90% of cathode ink was applied to the microporous gas–diffusion material (ELAT® GDL LT 1400-W, ETEK) microporous layer and about 10% of cathode ink is applied directly to a Nafion® membrane in a similar fashion to the anode ink. The catalyst coated membrane (CCM) was pressed with GDL layers at 689 N/cm² at 125 °C for 5 min. The MEA was tested under following conditions: H₂ and O₂ gases, heated and humidified at 85 °C and pressurized at 30 psi; 80 °C cell temperature.

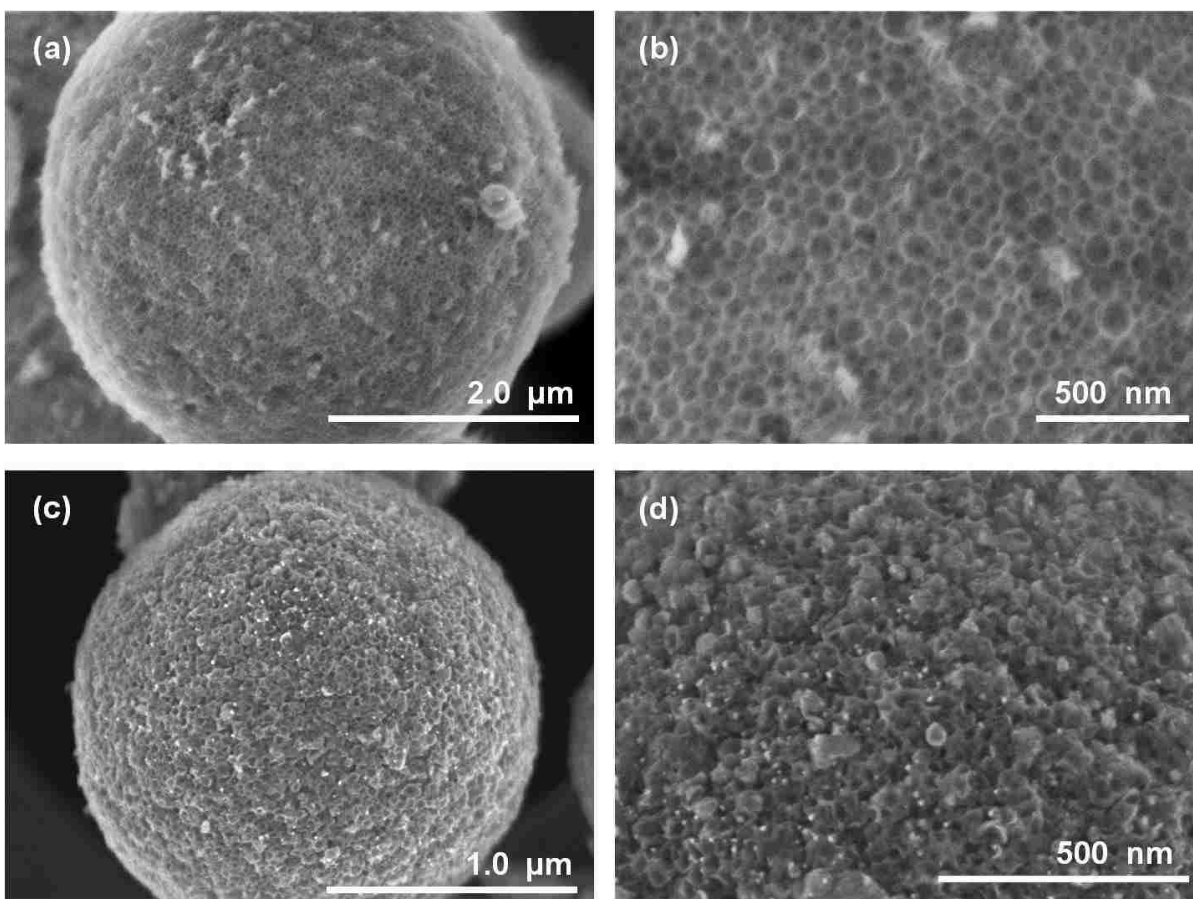


Figure 0.1. SEM images of a) silica particle, b) silica particle at higher magnification demonstrating open structure of the surface, c) templated carbon particles decorated with platinum nanoparticles, after pyrolysis and silica removal and d) templated carbon particles decorated with platinum nanoparticles after pyrolysis and silica removal, at higher magnification demonstrating templated structure

5.3 Results and Discussion

Materials characterization: The catalyst materials evaluated in this work were synthesized utilizing the templating of novel silica particles with bi-modal porosity (bi-porous silica).

Figure 1 shows SEM micrographs of the silica templating material (1a and 1b) as well as a Pt/carbon material (1c and 1d) after impregnation of the template, pyrolysis and silica template removal by dissolving it in KOH. TEM micrographs shown in Figure 2 also

exemplify silica templating material, and templated carbon and Pt/carbon particles, but here they demonstrate the internal structure and radial distribution of platinum nanophase. Single silica particle, shown in Figure 1a represents material obtained by simultaneous templating

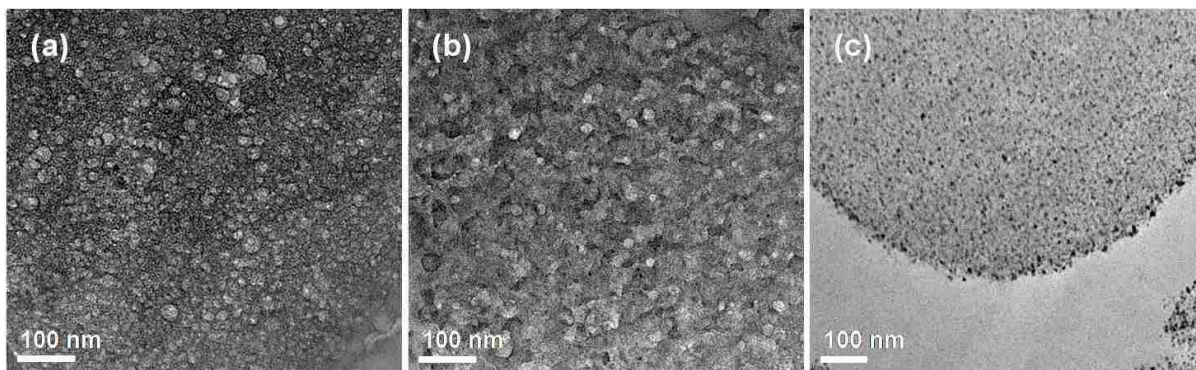


Figure 0.2. HRTEM micrographs of cross sections of a) silica particle showing porous structure obtained by templating with micelles and microemulsion droplets, b) carbon particle after pyrolysis and silica removal demonstrating the internal porous structure, and c) templated carbon particle decorated with platinum nanoparticles after pyrolysis and silica removal showing the dispersion of platinum nanoparticles.

with micelles and microemulsion droplets[176]. Here, we would like to point out that each silica particle has an internal framework of mesopores (in the range of 10-40 nm) that are connected through a network of nanopores (around 5 nm). Mesopores can be seen in the SEM images in Figures 1a and 1b and in the TEM image of the cross-section of silica particle in Figure 2a. TEM image of the silica cross-section also demonstrates the arrangement of the nanopores. Impregnation of the silica particles with carbon precursor results in the complete filling of silica mesopores. During pyrolysis, the carbon precursor (sucrose), undergoes decomposition and forms a conductive carbon backbone. SEM images in the Figures 1c and 1d show templated carbon (TC) particle decorated with platinum nanoparticles after the removal of the silica template. The low (Figures 1a and 1c) and high

(Figures 1b and 1d) magnification images of silica and carbon particles indicate that the structure of the carbon particles, negative replicas of the bi-porous silica particles is dictated by the porous structure of latter. Further, the internal structure of the carbon is exemplified by TEM analysis of the cross-section of the carbon particle (Figure 2b). The porous structure of the carbon is formed by the voids created after the removal of the silica template. BET surface area measurements for the templated carbon decorated with platinum nano-particles

Table 0-1. XPS elemental composition of GEN1 and GEN2 Pt/TC electrocatalysts.

Impregnation procedure, Sample generation		Theoretical platinum loading, wt%	Oxygen concentration, at%	Carbon concentration, at%	Platinum concentration, at%
Carbon and platinum precursors mixed together	GEN1	30	7.2	92.2	0.6
Majority of carbon precursor (70%), then the rest of carbon precursor (30%) mixed with platinum precursor	GEN1	30	8.3	90.6	1.1
Carbon precursor, then platinum precursor	GEN1	30	11.2	87.1	1.7
Carbon precursor, then platinum precursor	GEN1	20	11.1	87.9	1.0
Carbon precursor, then platinum precursor	GEN1	10	10.2	89.4	0.4
Carbon precursor, heat-treatment, then platinum precursor	GEN2	10	11.0	88.4	0.7

were found in the range of 400-700 m²/g depending on the synthesis conditions and loading of platinum.

The distribution of platinum particles supported on the carbon particles was investigated and compared for several GEN1 materials. First, the impregnation procedure was varied. When

silica was simultaneously impregnated with platinum and carbon precursors, the amount of surface platinum, as detected by XPS was quite low (Table 1). Also, a wide distribution of platinum particle size was obtained possibly from locking of platinum nanoparticles not only in the nanopores but also in the mesopores. When the platinum precursor was introduced simultaneously with carbon precursor but after the majority of carbon precursor was already loaded into silica, the amount of surface platinum increased from 0.6 to 1.1 at% (Table 1) and the average particle size of platinum, observed in

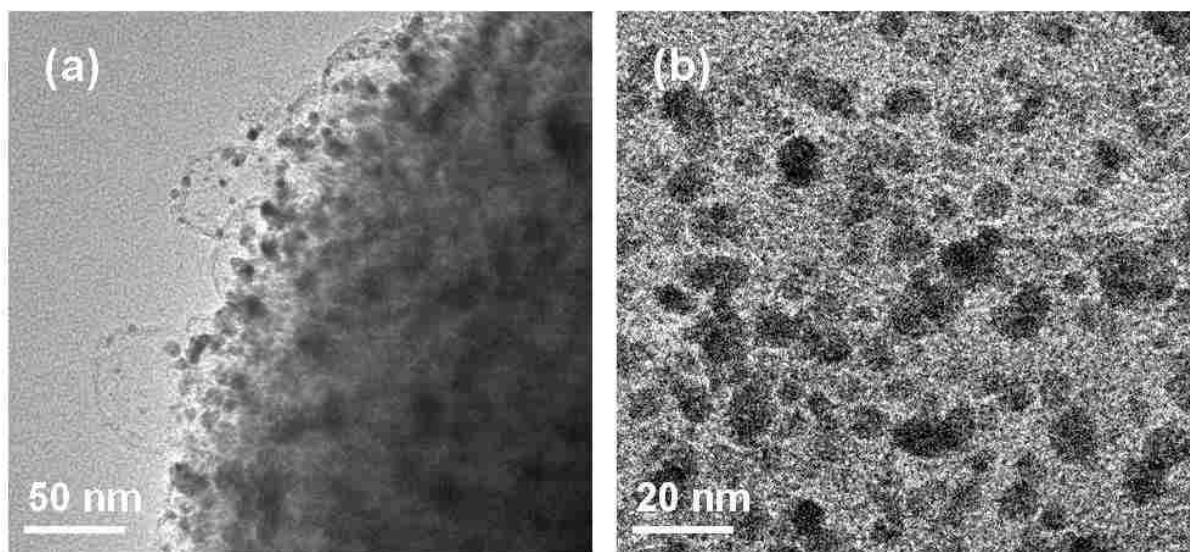


Figure 0.3. HRTEM images of 30 wt% Pt/TC a) showing edge of the carbon particle , and b) higher magnification image demonstrating size and dispersion of platinum nanoparticles.

TEM (not shown) decreased. Finally, the highest amount of platinum on the surface (about 1.7%) was detected when impregnation with platinum precursor was done after complete impregnation of the carbon precursor (Table 1). Further, the particle size distribution became more mono-dispersed and the overall dispersion was more homogeneous. Figure 3a is a TEM

micrograph of the GEN1 30 wt% Pt/TC material with the highest surface platinum content (platinum precursor impregnation after complete carbon precursor impregnation). The high-magnification image of the same material in Figure 3b illustrates that platinum particles are in the 3-8 nm range and are densely packed. TEM analysis of the cross-section of the particle has shown that platinum nano-particles are very well dispersed throughout the entire carbon particle (Figure 2c), indicating that the impregnation procedure resulted in the formation of the Pt nano-particle phase on the surface as well as within the porous network of the templated material.

The effect of the Pt loading on the size and dispersion of the decorating platinum particle phase supported on templated carbon was studied. Table 1 reflects the elemental

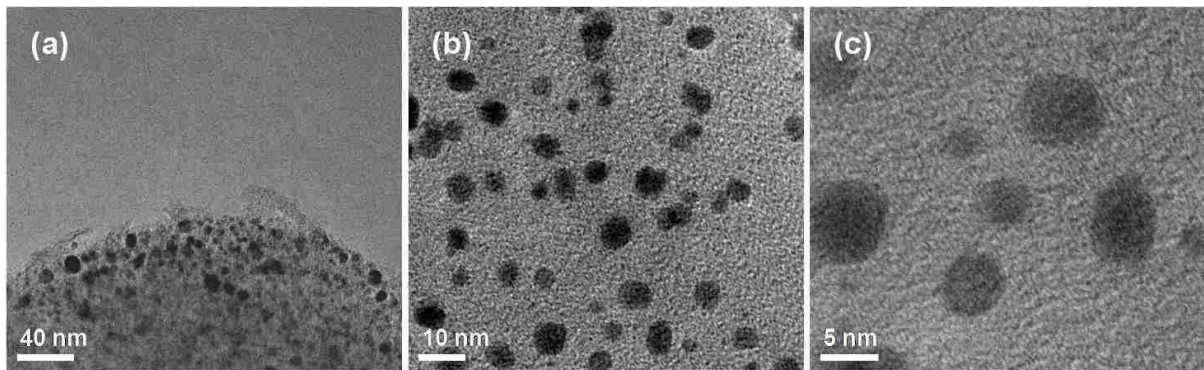


Figure 0.4. HRTEM images of 30 wt% Pt/TC a) showing edge of the carbon particle , b and c) higher magnification images demonstrating size and dispersion of platinum nanoparticles.

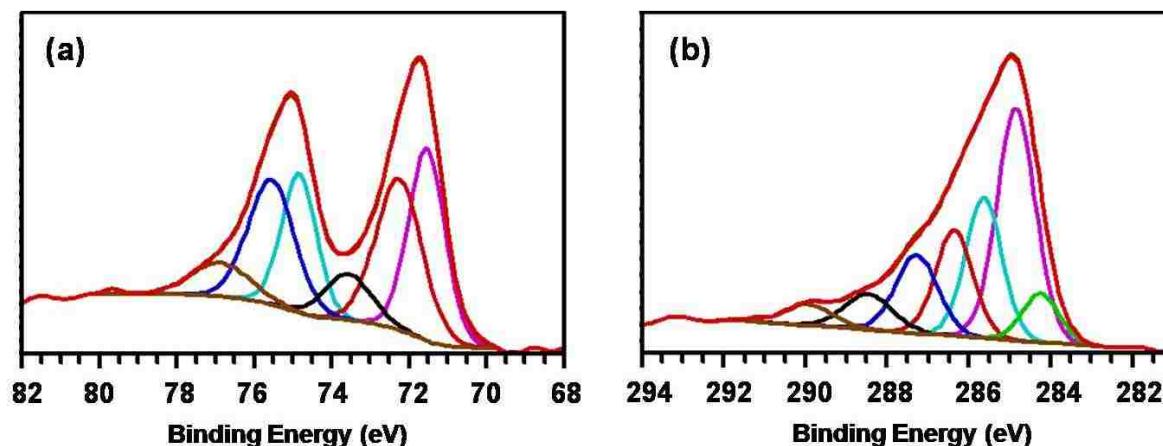


Figure 0.5. Representative high-resolution XPS spectra of Pt/TC materials a) Pt 4f spectrum and b) C 1s spectrum.

composition of materials with three different loadings of platinum as determined by XPS.

Decrease in the platinum loading results in the nominal decrease in the amount of platinum detected on the surface. For instance, the relative concentration of platinum changes from 1.7% in 30 wt% material to 1.0% and 0.4% in 20 wt% and 10 wt% Pt/TC materials.

Reduction in the nominal platinum amount results in less dense dispersion of platinum particles and accompanied by reduction in their size, as evident from the TEM analysis of 10 wt% Pt/TC material, shown in Figure 4.

Representative high-resolution Pt 4f spectrum and its deconvolution are shown in Figure 5a.

Platinum 4f spectrum consists of two components ($4f_{7/2}$ and $4f_{5/2}$) that are separated by 3.3 eV. Each of the components was curve-fitted with 3 peaks. Peaks at 71.5 eV

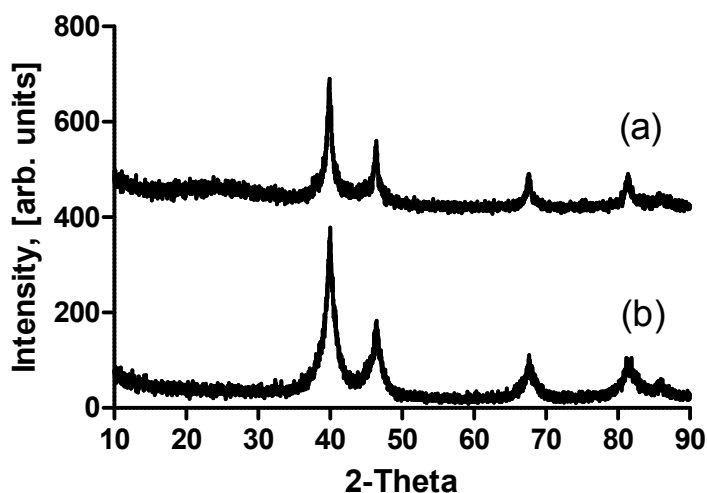


Figure 0.6. XRD patterns of Pt/TC materials a) 10 wt% Pt/TC and b) 30 wt% Pt/TC.

($7/2$ component) and 74.8 eV ($5/2$ component) correspond to metallic Pt. The next double, peaks at 72.3 eV ($7/2$ component) and 75.6 eV ($5/2$ component) are due to platinum hydroxides, Pt(OH)_x. Finally, the last double, peaks at 73.4 eV ($7/2$ component) and 76.7 eV ($5/2$ component) are contributions of platinum oxides, PtO_x. XPS analysis revealed that total platinum phase consists of metallic, hydroxide and oxide forms of approximately 35%, 48% and 16% respectively, and is about the same for all Pt/TC materials discussed above. This indicates that only elemental concentrations were affected by the variations in the impregnation steps and platinum loading.

Figure 5b shows high-resolution C1s spectrum typical of templated carbon decorated with platinum nanoparticles. Several types of carbon species can be distinguished in the C1s spectrum[204]. Amorphous carbon (C-C, at 285 eV) is the major form, while graphitic carbon (C=C, 284.3 eV) is the minor form. Other peaks are due to secondary carbon (C*-C-

O, at 285.6 eV) and carbon bonded to oxygen (C-O-C, C-OH, C=O, COOH, located in the range of 286-290 eV). The peak at 291 eV is a shake-up peak, indicative of

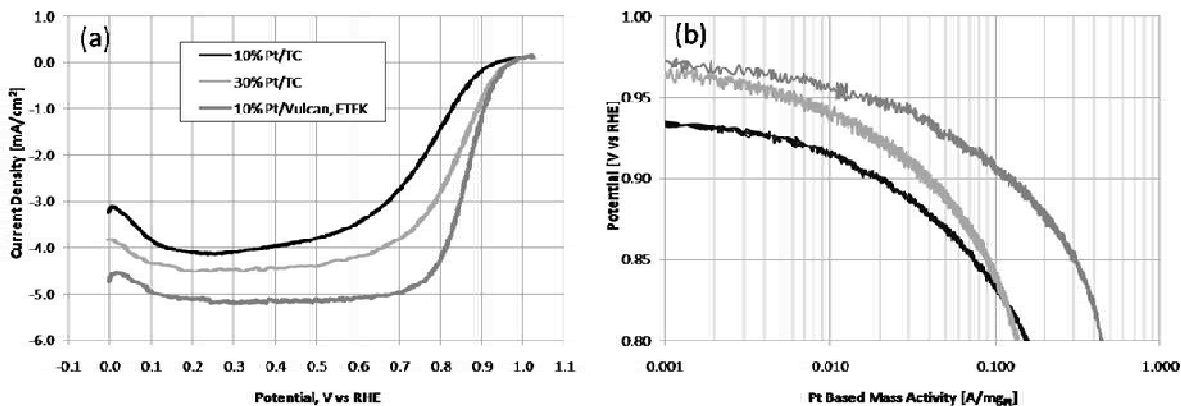


Figure 0.7. RDE polarization curves in 0.1M HClO₄ solution saturated with O₂ at 25 °C and 1600 rpm. Scan rate is 10 mV/s. Catalyst loading is 9.1 μg_{Pt}/cm² for 10 wt% Pt/TC, 20.5 μg_{Pt}/cm² for 30 wt% Pt/TC and 9.6 μg_{Pt}/cm² for 10 wt% Pt/Vulcan XC-72R, ETEK.

aromatic/graphitic structure. Only small variations in the carbon speciation were observed for materials with different loading of platinum.

XRD patterns for the 30 wt% and 10 wt% Pt/TC materials shown in Figure 6a and 6b are characteristic of carbon-supported platinum electrocatalyst. The shape of the XRD peaks, where the base of the peak is rather wide and peak around the maximum is rather sharp indicates that along with small platinum crystallites there is also a fraction of larger crystallite sizes. While smaller crystallite sizes are shown in the TEM images in Figures 2-4, larger crystallite sizes are apparent from the SEM image, shown in Figures 1c and 1d. Complete quantitative assessment of the Pt nano-phase is been hindrance at this stage

because of the different scale of the data sets (images) observed with SEM and TEM microphotography.

Electrochemical characterization of GEN1 electrocatalysts:

Oxygen reduction polarization curves obtained in RDE configuration for 10 wt% and 30 wt% Pt/TC materials are shown in Figure 7a. A 10 wt% Pt on Vulcan XC72 (commercial catalyst) was used as a benchmark. A diffusion limiting current density of -6 mA cm^{-2} , which is expected for materials that support direct $4 e^-$ transfer, such as Pt-based electrodes was not achieved for the template derived materials or the commercial 10 wt% Pt/C catalyst modified RDE. We are confident in these measurements as others have reported diffusion limiting current densities ranging between -5 and -6 mA cm^{-2} for RDE-type experiments when utilizing similar commercial catalysts as reported elsewhere[103, 205, 206]. When compared to commercial, 10 wt% Pt/Vulcan, both templated materials showed significantly lower performance. Lower than expected diffusion limited currents could be indicative of either lower number of transferred electrons per redox event and/or additional diffusion limitations in the pores of the templated material. Mass-normalized currents for these materials are shown in Figure 7b. It is clear, that intrinsic catalytic activity of GEN1 templated electrocatalysts is lower than that of commercial, Vulcan supported electrocatalyst. Comparison of templated electrocatalysts with different Pt loading reveals that material with higher Pt loading performs better than material with lower Pt loading. This observation might indicate that limited performance of templated electrocatalysts is caused by contamination, that effects low Pt loading material more than high Pt loading material.

Electrocatalyst optimization:

In search of the reasons of low ORR performance of templated materials, the pyrolysis conditions were simulated in a TGA instrument. The weight losses associated with the changes in the temperature for two unpyrolyzed materials, silica impregnated with sucrose and silica impregnated with sucrose and chloroplatinic acid are given in Figure 8. Multiple slopes, observed in the TGA graph of sucrose containing material indicate that decomposition of the sucrose to a conductive carbon phase is a multiple-step process that is

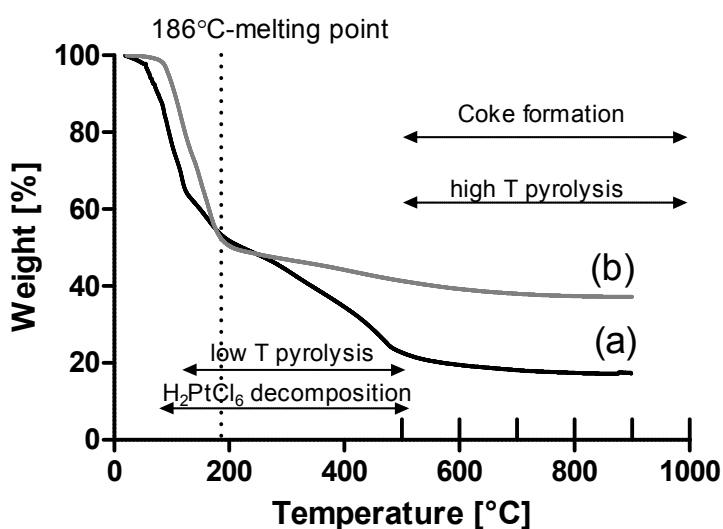


Figure 0.8. TGA analysis of a) silica filled with carbon precursor (sucrose) and b) silica filled with carbon (sucrose) and platinum (H₂PtCl₆·6H₂O) precursors. Conditions of the TGA analysis simulate conditions of the pyrolysis.

completed when the temperature reaches about 500 °C (Figure 8a). Similar temperature ranges have been reported for sucrose single crystals[207] and in other catalyst synthesis procedures utilizing sucrose as the carbon precursor[192, 195]. When the carbon and platinum precursors undergo simultaneous pyrolyzation (Figure 8b) the wt% loss is not as large due to the presence of non-volatile metal atoms. Here, pyrolysis is done in N₂

environment and therefore the only reducing agent present is the carbon precursor material. No further decomposition of sucrose or chloroplatinic acid are observed above 500°C. It is plausible that coking or Pt-catalyst deactivation may occur in the reported range. Decomposition of the sucrose might result in the coverage of the platinum, decreasing the amount of platinum accessible for participation in the oxygen reduction. Partial decomposition of sucrose at slightly elevated temperatures prior to impregnation with platinum precursor may lead to improved accessibility of platinum. Coking typically occurs at temperatures of 500 °C and higher, and is known to be catalyzed by metals, including platinum. Coking that results in the deactivation of the catalyst active phase cannot be

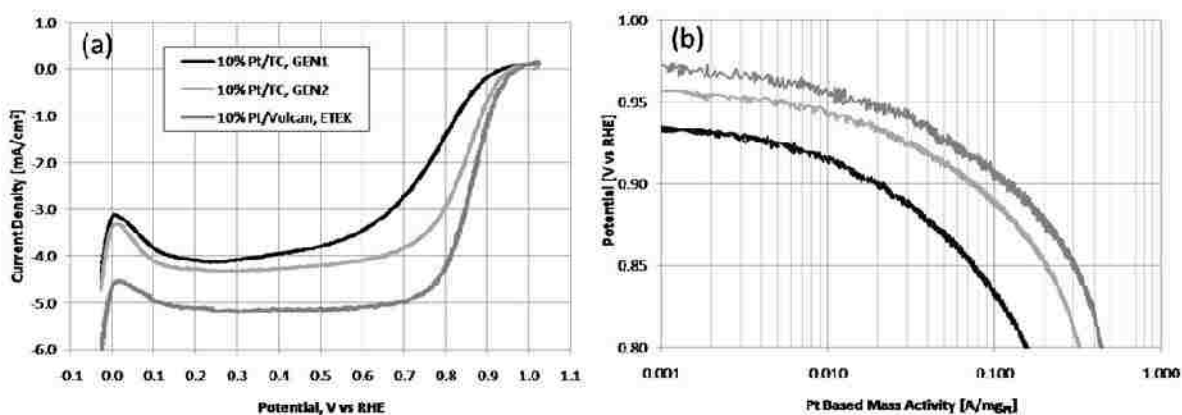


Figure 0.9. Polarization curves in RDE in 0.1M HClO₄ solution saturated with O₂ at 25 °C and 1600 rpm. Scan rate is 10 mV/s. Catalyst loading is 9.1 μg_{Pt}/cm² for GEN1 and GEN2 10 wt% Pt/TC, pyrolyzed at 900 °C, and 9.6 μg_{Pt}/cm² for 10 wt% Pt/Vulcan XC-72R, ETEK.

distinguished in the TGA curves shown in Figure 8. In order to understand if coking is indeed a problem relevant to performance of templated materials the temperature of the pyrolysis can be varied. The optimum synthesis procedure will result in decomposition of

both precursors, formation of the conductive carbon phase and minimization of coking. It appears that 500 °C is the lower end of the temperature range that should be investigated as this is the temperature when decomposition of both precursors is complete.

First, aiming to improve the accessibility of platinum and therefore the precious metal utilization, the impregnation procedure was modified to incorporate an intermediate heat-treatment step. 10 wt% Pt/TC catalyst was made using the heat-treatment performed after impregnation with sucrose precursor but before impregnation with platinum precursor. Only slight improvement in the diffusion limited region of the ORR polarization curve is achieved with an addition of intermediate heat-treatment (Figure 9a). A diffusion limiting current density of -6 mA cm^{-2} , which is expected for materials that support direct $4 e^-$ transfer, such as Pt-based electrodes was not achieved for the template derived materials or the commercial 10 wt% Pt/C catalyst modified RDE. We are confident in these measurements as others have reported diffusion limiting current densities ranging between -5 and -6 mA cm^{-2} for RDE-type experiments when utilizing similar commercial catalysts as reported here^{3,32,33}. The advancement in the mass-normalized (the theoretical Pt loading was used) currents measured at low overpotentials for this material, shown in Figure 9b is much more prominent. For instance, ORR activity at 0.9V, increased from $0.02 \text{ A/mg}_{\text{Pt}}$ to $0.075 \text{ A/mg}_{\text{Pt}}$. This result is a major improvement in the performance of the templated electrocatalyst as compared to initial results (GEN1). The initial set of materials, made without an intermediate heat-treatment is referred in the text as the first generation of templated electrocatalysts (GEN1). Materials made using intermediate heat-treatment are a second generation of templated electrocatalysts (GEN2).

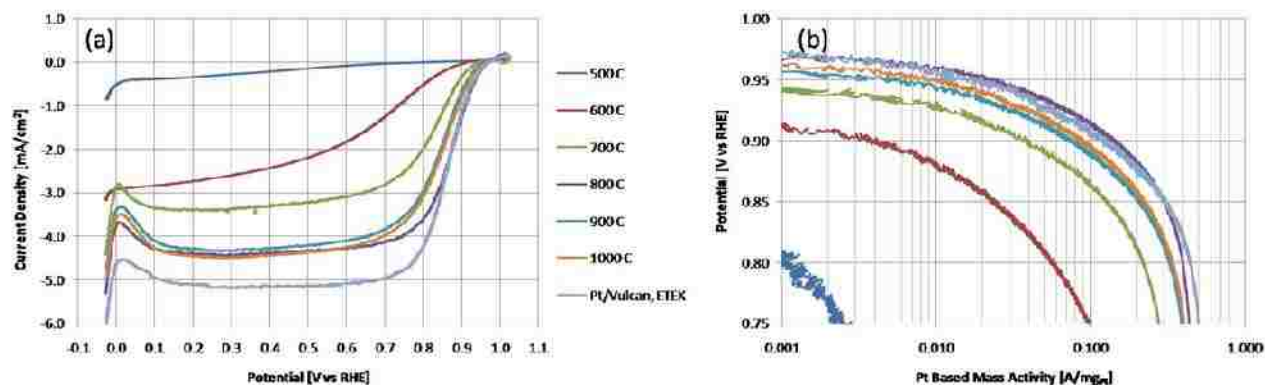


Figure 0.10. Polarization curves in RDE in 0.1M HClO₄ solution saturated with O₂ at 25 °C and 1600 rpm. Scan rate is 10 mV/s. Catalyst loading is 9.1 μg_{Pt}/cm² for GEN2 10 wt% Pt/TC, pyrolyzed at various temperatures, and 9.6 μg_{Pt}/cm² for 10 wt% Pt/Vulcan XC-72R, ETEK.

Electrochemical characterization of GEN2 electrocatalysts:

Next, an intermediate heat-treatment step was utilized during the synthesis of a number of materials. Here, silica material impregnated with sucrose was heat-treated in air at 150 °C for 1 hour and then the platinum precursor was added and a second heat-treatment in N₂ was performed at various temperatures. ORR RDE experiment results for materials pyrolyzed at 500, 600, 700, 800, 900 and 1000 °C are shown in Figure 10a. Pyrolysis temperatures lower than 800 °C result in very poor ORR performance, consequence of poor conductivity of the carbon support. The best ORR performance was obtained when pyrolysis was conducted at 800 °C. Materials, for which the temperature of the pyrolysis exceeded 800 °C, also exhibited significantly higher ORR performance as compared to materials pyrolyzed at low temperatures. The performance of 800, 900 and 1000 °C treated materials in the diffusion limited region is quite similar, but lower than expected for Pt catalyzed ORR under these conditions. It is possible that the Levich equation no longer holds for this system due to the

presence of additional diffusion limitations that occur in the mesopores of the Pt/TC modified RDE. These diffusion limitations are internal with respect to each particle of catalyst. Therefore the number electrons transferred per redox event cannot be estimated as often done in the literature. Figure 9b shows the mass-normalized currents that were calculated using the theoretical platinum loadings. The relative performance of the templated materials becomes more comparable to that of the commercial catalyst. The mass normalized currents exemplify the utility of the templated catalyst materials measured at low overpotentials. However, the mass-normalized currents for the templated materials pyrolyzed at 900 °C and 1000 °C is observed to be substantially lower than that of the 800 °C treated material. This suggests that the number of electrons transferred during oxygen reduction at temperatures above 800 °C decreases due to increase in the rate of coke formation during synthesis. The performance of the GEN2 800 °C treated material is very similar, especially in the kinetic region to that of the commercial Pt/Vulcan catalyst.

The effect of the optimized temperature conditions and addition of the intermediate heat-treatment on the elemental composition of Pt/TC material can be used to explain the improved catalytic activity of the GEN2 electrocatalysts. XPS analysis showed that despite

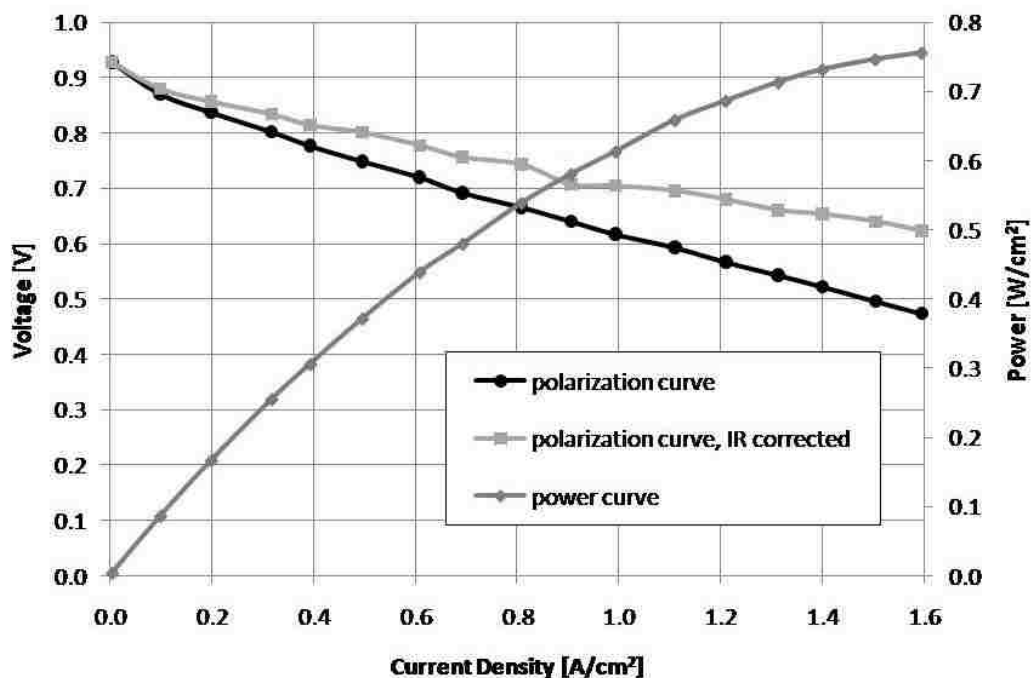


Figure 0.11. Polarization curves obtained during MEA testing with H₂/O₂ gas feeds heated and humidified at 85 °C and 30 psi backpressure. The cell temperature is 80 °C. Cathode catalyst is GEN2 10 wt% Pt/TC.

analogous theoretical loading of platinum, surface concentration of platinum in GEN2 and GEN1 electrocatalysts are different (Table 1). For instance, GEN2 electrocatalyst shows almost twice as much platinum as GEN1 electrocatalyst, and apparently, based on RDE data, the accessibility of the platinum is also much improved.

The material that showed the best RDE performance was also evaluated in MEA configuration with promising results. Single cell fuel cell polarization and power curves obtained for the GEN2 10 wt% Pt/TC electrocatalyst are shown in Figure 11. Aiming at improving hydrophobic-hydrophilic balance and thus transport of oxygen gas to the active sites, XC-35, Teflon-modified Vulcan XC72 carbon black was added to the catalyst ink.

Further, to improve the interphase between catalytic and GDL microporous layers, a majority (90%) of the catalyst ink was painted onto the GDL microporous layer and the balance (10%) was directly applied to the Nafion membrane[196].

Role of bimodal porosity of the template:

Typically, when platinum is deposited on the synthetic carbon derived from various carbon precursors, platinum impregnation is done after carbon support is formed (pyrolyzed). This procedure eliminates any problems that could potentially arise when both impregnations are done before the conductive carbon support is formed, including shielding of Pt during the decomposition of the carbon precursor at relatively low temperatures and coking, occurring at higher temperatures. SEM images of the 10 wt% Pt/TC made by impregnation of the pyrolyzed templated carbon are available in supporting information in SI Fig 1. Platinum decorated phase forms large islands made of rather large platinum particles. Apparently, the nanoporous network in silica doesn't translate into an accessible network in carbon structure that would effectively lock the size of platinum particles in the nanosize, as in the case of materials obtained when impregnation with platinum is done before the pyrolysis of carbon.

SEM images of the GEN2 10 wt% Pt/TC, that showed the best RDE performance, demonstrate two types of particles, typical for this material (Figures 2 and 3 in SI). First type of particles is formed by complete filling of the mesopores of the template. The rough surface of the carbon particles in this case is due to the voids created after the removal of the template. Second type of carbon particles is formed by incomplete filling of the mesopores in the template. Structure of these carbon particles is formed by the voids, result of the removal of silica template and by pores, result of incomplete filling of the silica mesopores.

The two roles of the mesopores in the silica template are to provide channels for effective infiltration with carbon precursor and, serve as the templates for the carbon mesopores. These, in turn are expected to serve as channels for the gaseous transport in the catalytic layer during MEA operation. Further optimization of the electrocatalyst will be focused on the optimization of the mesoporous structure of the carbon support.

Both types of carbon particles showed remarkable dispersion of the platinum phase. This emphasizes the essential role of the nanopores in the silica template for the synthesis of the electrocatalysts. Currently, pore size distribution of the nanopores in silica is centered about 5 nm. Their function is to lock platinum particles in the same nanosize range. It is conceivable that decreasing the pore size will lead to the decrease in the platinum particle size, and thus a better utilization of the noble metal. Another potential benefit of the nanoporous network is related to the degradation of electrocatalyst during fuel cell operation. Performance degradation of electrocatalysts is closely related to the growth of platinum particles and their detachment from the carbon support[186]. In the case of platinum supported on templated carbon, these processes might be less pronounced since platinum particles mobility is limited as they are locked in the pores.

5.4 Conclusions

The current study showed application of silica particles as templates for fabrication of templated carbon decorated with platinum nanophase for fuel cell catalyst applications. Silica particles have porous structure with bimodal distribution, created through micelle and microemulsion templating. The bimodal porosity of the silica template is crucial in the synthesis of electrocatalyst as it affects both structure of templated carbon and size and

dispersion of the decorated platinum nanophase. Electrocatalysts of GEN1 underperformed as compared to commercial platinum supported on Vulcan carbon black. Issues of contaminations and accessibility of platinum were addressed through optimization of the synthesis procedure by introducing an intermediate heat-treatment of the sucrose/silica material. Oxygen reduction performance for the GEN2 electrocatalysts showed close to an order of magnitude improvement in ORR activity in RDE measurements. For example, for 10 wt% Pt/TC electrocatalyst ORR activity at 0.9 V, measured in RDE, increased from 0.02 A/mg_{Pt} to 0.15 A/mg_{Pt}. The critical advantage of the novel fuel cell catalyst synthetic method is the degree of the control of the decorating platinum nanoparticle phase that can be exercised when templating bimodal porous silica particles. This allows to lock the size platinum nanoparticles in a desirable size range.. Investigation of transport properties and durability studies will be carried out to establish advantages of this class of materials.

Acknowledgments

This work was supported by NSF (PREM/DMR 0611616), NSF (CBET 0828900), DoE-EERE, V.C.7 Advanced Cathode Catalysts (UNM sub-award to Los Alamos National Laboratory) and DoE-EPSCoR Implementation Program: Materials for Energy Conversion.

Summary and Conclusions

6.1 Summary

The primary goals of this dissertation work were as follows:

- Develop novel materials and methods by executing polymerization chemistries within emulsion droplet reactors.
- Utilize unique physical and chemical properties of emulsions and interfaces for engineering of nanostructured particles.
- Merge complex emulsion polymerization systems with droplet-based microfluidic techniques to synthesize monodisperse particles with complex nanostructure.

Because emulsion droplets act as both the chemical reactor and morphological template during emulsion polymerization, the processed particles will necessarily obtain the shape and size distribution of the droplets. Emulsion systems also allow for environments necessary to carry out unique polymerization chemistries, such as anhydrous reaction synthesis of polyurethane microparticles. The ability to control the chemical makeup of two liquid phases (dispersed and continuous phases) provides exceptional and controllable environments and facilitates reactions that may not be possible in other settings, such as aerosols. Execution of poly-addition polyurethane chemistry in a fluorocarbon oil continuous phase, and the

inclusion of a novel fluorosurfactant emulsifier allowed for the 1-step synthesis of monodisperse polyurethane elastomeric microparticles.

Monodisperse P104 surfactant-templated silica particles were synthesized by modification of evaporative induced self assembly techniques within microfluidic-generated emulsion droplet reactors. The advantages of this method are control of synthesis parameters such as emulsion droplet size, temperature, evaporation speeds, humidity, and the composition of the surfactant solution. In comparison to aerosol methods, the relatively slower evaporation rate of the solvent from the emulsion droplets allows a high-degree of homogeneity of the components in the liquid crystalline phase prior to fossilization of the structures by silica condensation. This is perhaps the most important distinction of the emulsion EISA method from aerosol-based EISA methods. Two types of pores were produced, worm-like cylindrical pores and hexagonally ordered pores, both with a BJH pore width ~ 6 nm. It was also demonstrated that the particles could be connected by “bridges” that form when the particles come into contact before the completion of the gelation process. Controlled bridging and sticking of the particles allows fabrication of arrays with sufficient structural integrity for subsequent manipulation and application.

Metal oxide particles with hierarchical nanoporosity were synthesized by simultaneous templating with surfactant liquid crystalline structures co-existing with thermodynamically stable microemulsion phases. The microemulsion phase is formed at low interfacial tensions facilitated by synergistic adsorption of two types of surfactants at the aqueous sol-oil interface. Tuning the phase state by adjusting the surfactant composition and concentration allows for the controlled design of a system where microemulsion droplets coexist with

smaller surfactant micellar structures. The microemulsion droplet and micellar dimensions determine the two types of pore sizes: pores with dimensions in the tens of nanometers whose walls are themselves porous with smaller pores with widths of single nanometers. DLS measurements showed the coexistence of two structures, one with dimensions of single nanometers (representing the CTAB micelles) and one with dimensions in the tens of nanometers (representing the oil microemulsion drops). The smaller pores were characterized via XRD, which indicates cylindrical pores hexagonally packed with a d-spacing of approximately 6 nm. From nitrogen sorption isotherm data, a BET surface area of ~1000 m²/g is estimated and an NLDFT pore size distribution model indicates smaller pores (6 nm) existing with larger pores in the tens of nanometers. A key feature of the bimodally porous particles is that, unlike surfactant-only templated mesoporous particles, they allow direct, open access to the porous structures at the surface. This greatly improves the functionality of the particles for practical engineering purposes.

It was determined that slight variations in microemulsion mixture components (electrolyte concentration, wt% of surfactants, oil to sol ratio, etc.) produces strikingly different pore morphologies and particle surface areas. The results are summarized in the table below.

Table 0-1. Surface pore size and BET surface area for particles obtained by varying microemulsion mixture components.

Mixture Variation	Surface Pore Size (nm)	BET Surface Area (m²/g)
Standard	40	1000
0.075 M NaCl	> 60	650
0.15 M NaCl	~40	850
2:1 Oil to Sol	10 to 50	1038
25% less ABIL	40 to > 100	975
25% more CTAB	None	1250

Control over microemulsion phase and thus larger pores is crucial for control over transport properties within the porous particles as well as control over surface morphology of the particles. This was established as ‘smooth’ multimodal porous particles were designed for use as drug delivery vehicles in which fluidity of fused liposomes and proteins to the surface is crucial to successful cell signaling for particle uptake via endocytosis.

It was determined control over the size and structure of the smaller micelle-templated pores was possible by varying the length of the hydrocarbon block within the trimethyl ammonium bromide surfactant. The findings are summarized below.

Table 0-2. d-spacing for cationic surfactant with decreasing hydrophobic block length.

Surfactant	d_{spacing} (nm)
C ₁₆ TAB	6.0
C ₁₅ TAB	4.9
C ₁₄ TAB	4.0
C ₁₃ TAB	3.4

Replica catalyst materials (carbon and carbon decorated with platinum nano particles) were synthesized using a ‘lost wax’ method in which the porous silica is infiltrated with liquid precursors followed by controlled pyrolysis and dissolution of the silica template.

Optimization of the synthesis conditions resulted in significantly improved performance toward oxygen reduction, evaluated in rotating disk electrode (RDE) and membrane electrode assembly (MEA) configurations. The bimodal porosity of the silica template and open access to the pores at the surface are crucial in the synthesis of electrocatalyst as it affects both structure of templated carbon and size and dispersion of the decorated platinum nanophase

The effect of emulsion aging was studied by synthesizing particles at progressive time levels from a sample emulsion. It was discovered surface pore size increases after just a few hours, with high number of hollow particles observed. After 3 days, the particles were irregular shaped with little surface porosity observed via SEM. This may indicate that the microemulsion in the standard synthesis is not at equilibrium and that the alkoxide monomer, TEOS, may change surface activity over time as additional levels of hydrolysis are obtained.

Monodisperse, microemulsion nanoporous particles were synthesized utilizing a microfluidic platform. Emulsification of silica precursor in a pure oil phase at the microfluidic orifice, with infusion of surfactant-laden oil phase into the device downstream of the orifice, allows for successful fluidic treatment of a low interfacial tension system and the formation of monodisperse particles. Temperate evaporation of the solvent from the droplets at ambient conditions preserves the excellent size distribution of the fluidic-formed precursor droplets during gelation. Successful synthesis of monodisperse silica particles with bimodal nanoporosity demonstrates control at three different length scales: the nanoscale via surfactant molecular templating, the colloidal level via spontaneous microemulsion templating and at the micron level through control of overall size distribution through microfluidic platform.

6.2 Conclusions

The following conclusions can be derived from this dissertation project:

- Emulsion systems accommodate unique chemistries, including anhydrous synthesis of polyurethane latex particles in an inert fluorocarbon oil continuous phase. We demonstrate the benefits of this system with the example of suspension polymerization of polyurethane particles. In a simple one-step process, solid particles are made with the options of cross-linking, grafting fluorescent dyes to the polymer network, and controlling its mesh-size through addition of an inert solvent during polymerization.
- We have demonstrated that microfluidics can be successfully used to fabricate monodisperse mesoporous silica particles with well defined size. A great advantage of the monodisperse particles is that they can be ordered in 2D arrays on various substrates. Controlled bridging and sticking of the particles allows fabrication of arrays with sufficient structural integrity for subsequent manipulation and application. In comparison to aerosol methods, the relatively slower evaporation rate of the solvent from the emulsion droplets through a liquid continuous phase allows a high-degree of homogeneity of the components in the liquid crystalline phase prior to fossilization of the structures by silica condensation. This is perhaps the most important distinction of the emulsion EISA method from aerosol-based EISA methods.
- Particles with hierarchical porosity can be synthesized by templating of the silica with coexisting surfactant micelle and microemulsion structures. There are two necessary conditions for obtaining bimodal porous structures through the microemulsion templating procedure described in this dissertation. First the two surfactants should significantly decrease the interfacial tension when adsorbed leading to a spontaneous

formation of microemulsion droplets. Second, the ionic surfactant should be soluble *only* in the aqueous phase while the non-ionic surfactant should be soluble *only* in the oil phase. The excess ionic surfactant that remains in the bulk forms micelles that are trapped in the solidifying silica, creating the subset of smaller pores with dimensions of a few nanometers. Mixture components such as electrolyte and surfactant concentrations have direct effect on the larger pores templated by the microemulsion phase. The size and dispersion of the smaller pores can be controlled by changing the length of the hydrophobic block of the cationic trimethyl ammonium bromide surfactant. Aging experiments suggest the microemulsion may not be at equilibrium, but could be undergoing conformational changes as TEOS is further hydrolyzed and changes level of surface activity.

- The surface structure of microemulsion templated particles facilitates direct access to the porous network, greatly improving the functionality of the particles for engineering applications. The excellent functionality and transport properties of the particles were demonstrated by their use as templates for replica catalyst materials and as drug delivery vehicles.
- Monodisperse hierarchically porous particles can be synthesized using a microfluidic platform. The key to the methodology is first forming droplets within a microfluidic orifice then adding surfactant-laden oil phase further downstream to initiate microemulsion formation at low interfacial tension.

6.3 Recommendations for Future Work

Extensive experimental research on hierarchically porous particles templated from surfactant and microemulsion phases suggests that as the emulsion is aged, structural changes take place over time. This would indicate that there are changes in interfacial tension as time progresses. To better understand and therefore control the microemulsion phase transformation in the aqueous drops it will be necessary to perform measurements of the interfacial tension of the oil/aqueous phase/surfactant system as a function of time. This will test our hypothesis on how the interfacial tension affects the microemulsion formation and provide necessary quantitative information for the data interpretation. The interfacial tension is essential for determining the phase state. It usually exhibits a sharp minimum when the salt concentration and temperature are varied.

In conjunction with interfacial measurements, light scattering experiments should be carried out to track the conformational changes of the microemulsion and surfactant structures and correlate this data to the interfacial tension measurements. This will give insight into the kinetics and associated structural changes of this complex system.

The formation of monodisperse hierarchically porous particles is desirable as this enables the particles to potentially be ordered in 2D and 3D arrays for designing structures with hierarchical porosity. The driving force is capillary interactions that bring the particles together [208-214]. A custom built set up for 2D and 3D ordered layers self assembly can be utilized that has been proven to be very suitable for obtaining particle arrays [99]. This experimental set-up is available at UNM and will allow obtaining bulk structures with

hierarchical porosity. There will be three typical pore sizes: (i) a few nanometers from the templating of pure oil free surfactant micelles, (ii) a few tens of nanometers from templating of microemulsion droplets and (iii) in micrometer range from the interparticle voids. The latter is directly related to the particle size.

References

1. Nie, Z.H., et al., *Polymer particles with various shapes and morphologies produced in continuous microfluidic reactors*. Journal of the American Chemical Society, 2005. **127**(22): p. 8058-8063.
2. Dendukuri, D., et al., *Controlled synthesis of nonspherical microparticles using microfluidics*. Langmuir, 2005. **21**(6): p. 2113-2116.
3. Serra, C., et al., *A predictive approach of the influence of the operating parameters on the size of polymer particles synthesized in a simplified microfluidic system*. Langmuir, 2007. **23**(14): p. 7745-7750.
4. Xu, S., et al., *Generation of monodisperse particles by using microfluidics: Control over size, shape, and composition (vol 44, pg 724, 2005)*. Angewandte Chemie-International Edition, 2005. **44**(25): p. 3799-3799.
5. Ikkai, F., et al., *New method of producing mono-sized polymer gel particles using microchannel emulsification and UV irradiation*. Colloid and Polymer Science, 2005. **283**(10): p. 1149-1153.
6. Zhang, H., et al., *Microfluidic production of biopolymer microcapsules with controlled morphology*. Journal of the American Chemical Society, 2006. **128**(37): p. 12205-12210.
7. Hu, Y. and J.M. Prausnitz, *Molecular Thermodynamics of Partially-Ordered Fluids - Microemulsions*. Aiche Journal, 1988. **34**(5): p. 814-824.
8. Nagarajan, R. and E. Ruckenstein, *Molecular theory of microemulsions*. Langmuir, 2000. **16**(16): p. 6400-6415.
9. Binks, B.P., *Modern Aspects of Emulsion Science*, in *Modern Aspects of Emulsion Science*. 1998, The Royal Society of Chemistry. p. 56-444.
10. Ivanov, I.B., *Thin liquid films : fundamentals and applications*. 1988, New York: M. Dekker. viii, 1126 p.
11. Bancroft, W.D., *The theory of emulsification, V*. Journal of Physical Chemistry, 1913. **17**(6): p. 501-519.
12. Birdi, K.S., *Handbook of surface and colloid chemistry*. 1997, Boca Raton, Fla.: CRC Press. 763 p.
13. Barnes, G. and I. Gentle, *Interfacial science : an introduction / Geoffrey Barnes, Ian Gentle*, Oxford :: Oxford University Press.

14. Margulies, M., et al., *Genome sequencing in microfabricated high-density picolitre reactors*. Nature, 2005. **437**(7057): p. 376-380.
15. Shendure, J., et al., *Accurate multiplex polony sequencing of an evolved bacterial genome*. Science, 2005. **309**(5741): p. 1728-1732.
16. Janasek, D., J. Franzke, and A. Manz, *Scaling and the design of miniaturized chemical-analysis systems*. Nature, 2006. **442**(7101): p. 374-380.
17. Psaltis, D., S.R. Quake, and C.H. Yang, *Developing optofluidic technology through the fusion of microfluidics and optics*. Nature, 2006. **442**(7101): p. 381-386.
18. deMello, A.J., *Control and detection of chemical reactions in microfluidic systems*. Nature, 2006. **442**(7101): p. 394-402.
19. Anna, S.L., N. Bontoux, and H.A. Stone, *Formation of dispersions using "flow focusing" in microchannels*. Applied Physics Letters, 2003. **82**(3): p. 364-366.
20. Song, H., D.L. Chen, and R.F. Ismagilov, *Reactions in droplets in microfluidic channels*. Angewandte Chemie-International Edition, 2006. **45**(44): p. 7336-7356.
21. Xia, Y.N. and G.M. Whitesides, *Soft lithography*. Annual Review of Materials Science, 1998. **28**: p. 153-184.
22. Li, W., et al., *Screening of the effect of surface energy of microchannels on microfluidic emulsification*. Langmuir, 2007. **23**(15): p. 8010-8014.
23. Gunther, A. and K.F. Jensen, *Multiphase microfluidics: from flow characteristics to chemical and materials synthesis (vol 6, pg 1487, 2006)*. Lab on a Chip, 2007. **7**(7): p. 935-935.
24. Tan, Y.C., V. Cristini, and A.P. Lee, *Monodispersed microfluidic droplet generation by shear focusing microfluidic device*. Sensors and Actuators B-Chemical, 2006. **114**(1): p. 350-356.
25. Thorsen, T., et al., *Dynamic pattern formation in a vesicle-generating microfluidic device*. Physical Review Letters, 2001. **86**(18): p. 4163-4166.
26. Garstecki, P., H.A. Stone, and G.M. Whitesides, *Mechanism for flow-rate controlled breakup in confined geometries: A route to monodisperse emulsions*. Physical Review Letters, 2005. **94**(16).
27. Zhou, H.S., et al., *NO and NO₂ gas sensors based on surface photovoltage system fabricated by self-ordered mesoporous silicate film*. Nanoporous Materials, 2002. **141**: p. 623-630.
28. Prim, A., et al., *Synthesis and characterization of chromium-doped mesoporous tungsten oxide for gas-sensing applications*. Adv. Functional Mat., 2007. **17**: p. 2957-2963.
29. Ismail, A.A., *A selective optical sensor for antimony based on hexagonal mesoporous structures*. J. Colloid Interface Sci., 2008. **317**: p. 288-297.
30. Yantasee, W., et al., *Nanostructured electrochemical sensors based on functionalized nanoporous silica for voltammetric analysis of lead, mercury, and copper*. J. Nanosci. Nanotechnol., 2005. **5**.
31. Kim, N.H. and G.J. Kim, *Synthesis of mesoporous tin oxide and its application as a LNG sensor*. J. Nanosci. Technol., 2007. **7**: p. 3914-3916.
32. Qi, Z.M., I. Honma, and H. Zhou, *Ordered-mesoporous-silica-thin-film-based chemical gas sensors with integrated optical polarimetric interferometry*. Appl. Phys. Lett., 2006. **88**: p. 053503.

33. Ramarao, G.V., et al., *Biomimetic molecular assemblies on glass and mesoporous silica microbeads for biotechnology*. Langmuir, 2003. **19**: p. 1654-1663.
34. Martinez, C.J., et al., *Porous tin oxide nanostructured microspheres for sensor applications*. Langmuir, 2005. **21**: p. 7937-7944.
35. Blasco, T., et al., *Synthesis, characterization, and catalytic activity of Ti-MCM-41 structures*. J. Catalysis., 1995. **156**: p. 65-74.
36. Ayyappan, S. and N. Ulagappan, " , ,, *Synthesis and catalytic properties of cobalt- and molybdenum-containing mesoporous MCM-41 molecular sieves*. Proc. Ind. Acad. Sci., 1996. **108**: p. 505-510.
37. Cejka, J. and S. Mintova, *Perspectives of micro/mesoporous composites in catalysis*. Catalysis Rev.-Sci. Eng., 2007. **49**: p. 457-509.
38. Li, C., et al., *Chiral catalysis in nanopores of mesoporous materials*. Chem. Comm., 2007. **6**: p. 547-558.
39. De Vos, D.E., et al., *Ordered mesoporous and microporous molecular sieves functionalized with transition metal complexes as catalysts for selective organic transformations*. Chem. Rev., 2002. **102**: p. 3615-3640.
40. Stein, A., B.J. Melde, and R.C. Schroden, *Hybrid inorganic-organic mesoporous silicates - Nanoscopic reactors coming of age*. Adv. Mater., 2000. **12**: p. 1403-1419.
41. Ying, J.Y., C.P. Mehnert, and M.S. Wong, *Synthesis and applications of supramolecular-templated mesoporous materials*. Angew. Chem., 1999. **38**: p. 56-77.
42. Vallet-Regi, M., et al., *A new property of MCM-41: drug delivery system*. Chem. Mater., 2001. **13**: p. 308-311.
43. Song, S.W., K. Hidajat, and S. Kawi, *pH-controllable drug release using hydrogel encapsulated mesoporous silica*. Chem. Comm., 2007. **42**: p. 4396-4398.
44. Qu, F.Y., et al., *Controlled release of Captopril by regulating the pore size and morphology of ordered mesoporous silica*. Microporous Mesoporous Mater., 2006. **92**: p. 1-9.
45. Song, S.W., H. K., and S. Kawi, *Functionalized SBA-15 materials as carriers for controlled drug delivery: Influence of surface properties on matrix-drug interactions*. Langmuir, 2005. **21**: p. 9568-9575.
46. Barbe, C., et al., *Silica particles: A novel drug-delivery system*. Adv. Mater., 2004. **16**: p. 1959-1966.
47. Vallet-Regi, M., et al., *Hexagonal ordered mesoporous material as a matrix for the controlled release of amoxicillin*. Solid State Ionics, 2004. **172**: p. 435-439.
48. Xue, J.M. and M.J. Shi, *PLGA/mesoporous silica hybrid structure for controlled drug release*. Controlled Release, 2004. **98**: p. 209-217.
49. Lai, C.Y., et al., *A mesoporous silica nanosphere-based carrier system with chemically removable CdS nanoparticle caps for stimuli-responsive controlled release of neurotransmitters and drug molecules*. J. Am. Chem. Soc, 2003. **125**: p. 4451-4459.
50. Liu, Y.Y., H. Miyoshi, and M. Nakamura, *Novel drug delivery system of hollow mesoporous silica nanocapsules with thin shells: Preparation and fluorescein isothiocyanate (FITC) release kinetics*. Colloids Surfaces B, 2007. **58**: p. 1800-1807.
51. Zhou, J.C., et al., *Immunoassays for cortisol using antibody-doped sol-gel silica*. J. Mater. Chem., 2004. **14**: p. 2311.

52. Urabe, Y., et al., *Encapsulation of hemoglobin in mesoporous silica (FSM) - Enhanced thermal stability and resistance to denaturants*. Chem. BioChem., 2007. **8**: p. 668-674.
53. Baca, H.K., et al., *Cell-directed assembly of lipid-silica nanostructures providing extended cell viability*. Science, 2006. **313**: p. 337-341.
54. Yokogawa, Y., S. Seelan, and Y. Zhang, " , 309-311, 939-942., *Hyperstructured hydroxyapatite ceramics as a carrier for cell and protein*. Bioceramics, 2006. **18**.
55. Kim, J., J.W. Grate, and P.-C. Wang, *Nanostructures for enzyme stabilization*. Chem. Eng. Sci., 2006. **61**: p. 1017-1026.
56. Galarneau, A., et al., *Immobilization of lipase on silicas. Relevance of textural and interfacial properties on activity and selectivity*. New J. Chem., 2006. **30**: p. 562-571.
57. Luo, T.-J.M., et al., *Photo-induced proton gradients and ATP biosynthesis produced by vesicles encapsulated in a silica matrix*. Nature Materials, 2005. **4**: p. 220.
58. Wang, Y.J. and F. Caruso, *Mesoporous silica spheres as supports for enzyme immobilization and encapsulation*. Chem. Mater., 2005. **17**: p. 953-961.
59. Hartmann, M., *Ordered mesoporous materials for bioadsorption and biocatalysis*. Chem. Mater., 2005. **18**: p. 4577-4593.
60. Muresanu, M., et al., *A new mesoporous micelle-templated silica route for enzyme encapsulation*. Langmuir, 2005. **21**: p. 4648-4655.
61. Sudant, G., et al., *Synthesis and electrochemical properties of vanadium oxide aerogels prepared by a freeze-drying process*. J. Electrochem. Soc., 2004. **151**: p. A666-A671.
62. Kickhoefer, V.A., et al., *Engineering of vault nanocapsules with enzymatic and fluorescent properties*. Proc. Natl Acad. Sci. (USA), 2005. **102**: p. 4348-4352.
63. Chia, S., et al., *Patterned Hexagonal Arrays of Living Cells in Sol-Gel Silica Films*. J. Am. Chem. Soc, 2000. **122**: p. 6488-6489.
64. Mamak, M., N. Coombs, and G.A. Ozin, *Practical solid oxide fuel cells with anodes derived from self-assembled mesoporous-NiO-YSZ*. Chem. Comm., 2002. **20**: p. 2300-2301.
65. Emons, T.T., J.Q. Li, and L.F. Nazar, *Synthesis and characterization of mesoporous indium tin oxide possessing an electronically conductive framework*. J. Am. Chem. Soc, 2002. **124**: p. 8516-8517.
66. Lee, J.S., S.H. Joo, and R. Ryoo, *Synthesis of mesoporous silicas of controlled pore wall thickness and their replication to ordered nanoporous carbons with various pore diameters*. J. Am. Chem. Soc, 2002. **124**: p. 1156-1157.
67. Yantasee, W., et al., *Screen-printed electrodes modified with functionalized mesoporous silica for voltammetric analysis of toxic metal ions*. Electrochem. Comm., 2005. **7**: p. 1170-1176.
68. Lim, J., et al., *Nanostructured sol-gel electrodes for biofuel cells*. J. Electrochem. Soc., 2007. **154**: p. A140-A145.
69. Lim, J., et al., *Direct electron transfer in nanostructured sol-gel electrodes containing bilirubin oxidase*. Phys. Chem. Chem. Phys., 2007. **9**: p. 1809-1814.
70. Lee, D.H., et al., *Functional porous tin oxide thin films fabricated by inkjet printing process*. Electrochem. Solid State Lett., 2007. **10**: p. K51-K54.

71. Assink, R.A. and B.D. Kay, *SOL-GEL KINETICS .1. FUNCTIONAL-GROUP KINETICS*. Journal of Non-Crystalline Solids, 1988. **99**(2-3): p. 359-370.
72. Assink, R.A. and B.D. Kay, *SOL-GEL KINETICS .3. TEST OF THE STATISTICAL REACTION MODEL*. Journal of Non-Crystalline Solids, 1988. **107**(1): p. 35-40.
73. Israelachvili, J.N., *Intermolecular and surface forces*. 3rd ed, Burlington, MA: Academic Press. xxx, 674 p.
74. Lettow, J.S., et al., *Hexagonal to mesocellular foam phase transition in polymer-templated mesoporous silicas*. Langmuir, 2000. **16**(22): p. 8291-8295.
75. Brinker, C.J., et al., *Evaporation-induced self-assembly: Nanostructures made easy*. Advanced Materials, 1999. **11**(7): p. 579-+.
76. Pecora, R., *Dynamic light scattering : applications of photon correlation spectroscopy*. 1985, New York: Plenum Press. xiv, 420 p.
77. Langmuir, I., *THE ADSORPTION OF GASES ON PLANE SURFACES OF GLASS, MICA AND PLATINUM*. Journal of the American Chemical Society, 1918. **40**: p. 1361-1403.
78. Langmuir, I., *The constitution and fundamental properties of solids and liquids Part I Solids*. Journal of the American Chemical Society, 1916. **38**: p. 2221-2295.
79. Gilbert, R. 1995: Academic Press Inc., San Diego.
80. VivaldoLima, E., et al., *Industrial & Engineering Chemistry Research*, 1997: p. 36.
81. Dieterich, D. and H.G. Schmelzer, *Polyurethane Handbook*, ed. G. Oertel. 1994, Munich: Hanser publishers.
82. Levy, J. and K. Lai, *New Developments in Water-Borne Polyurethane Dispersions*. JALCA, 1994. **89**: p. 66 - 79.
83. Odian, G. 4th ed: Wiley & Sons.
84. Muller, K., M. Klapper, and K. Mullen, *Preparation of high molecular weight polyurethane particles by nonaqueous emulsion polyaddition*. Colloid and Polymer Science, 2007. **285**(10): p. 1157-1161.
85. B. K. Kim Colloid Polym. Sci., 1996. **274**: p. 599-611.
86. Dietrich, D., Prog. Org. Coat., 1981. **9**: p. 281.
87. Barni, A. and M. Levi, *Aqueous polyurethane dispersions: A comparative study of polymerization processes*. Journal of Applied Polymer Science, 2003. **88**(3): p. 716-723.
88. Andersson, N., et al., *Combined emulsion and solvent evaporation (ESE) synthesis route to well-ordered mesoporous materials*. Langmuir, 2007. **23**(3): p. 1459-1464.
89. Schacht, S., et al., *Oil-water interface templating of mesoporous macroscale structures*. Science, 1996. **273**(5276): p. 768-771.
90. Huo, Q.S., et al., *Preparation of hard mesoporous silica spheres*. Chemistry of Materials, 1997. **9**(1): p. 14-&.
91. Rao, G.V.R., et al., *Monodisperse mesoporous silica microspheres formed by evaporation-induced self assembly of surfactant templates in aerosols*. Advanced Materials, 2002. **14**(18): p. 1301-+.
92. Luo, T.J.M., et al., *Photo-induced proton gradients and ATP biosynthesis produced by vesicles encapsulated in a silica matrix*. Nature Materials, 2005. **4**(3): p. 220-224.
93. Denkov, N.D., et al., *Mechanism of Formation of 2-Dimensional Crystals from Latex-Particles on Substrates*. Langmuir, 1992. **8**(12): p. 3183-3190.

94. Dimitrov, A.S. and K. Nagayama, *Continuous convective assembling of fine particles into two-dimensional arrays on solid surfaces*. Langmuir, 1996. **12**(5): p. 1303-1311.
95. Buranda, T., et al., *Biomimetic molecular assemblies on glass and mesoporous silica microbeads for biotechnology*. Langmuir, 2003. **19**(5): p. 1654-1663.
96. Bore, M.T., et al., *Hexagonal mesostructure in powders produced by evaporation-induced self-assembly of aerosols from aqueous tetraethoxysilane solutions*. Langmuir, 2003. **19**(2): p. 256-264.
97. Garcia, A.L., et al., *Electrokinetic molecular separation in nanoscale fluidic channels*. Lab on a Chip, 2005. **5**(11): p. 1271-1276.
98. O'Brien, M.J., et al., *Fabrication of an integrated nanofluidic chip using interferometric lithography*. Journal of Vacuum Science & Technology B, 2003. **21**(6): p. 2941-2945.
99. Prevo, B.G. and O.V. Velev, *Controlled, Rapid Deposition of Structured Coatings from Micro- and Nanoparticle Suspensions*. Langmuir, 2004. **20**: p. 2099-2107.
100. Prevo, B.G., J.C. Fuller, and O.D. Velev, *Rapid deposition of gold nanoparticle films with controlled thickness and structure by convective assembly*. Chemistry of Materials, 2005. **17**(1): p. 28-35.
101. Cejka, J. and S. Mintova, *Perspectives of micro/mesoporous composites in catalysis*. Catalysis Reviews-Science and Engineering, 2007. **49**(4): p. 457-509.
102. Hartmann, M., *Ordered mesoporous materials for bioadsorption and biocatalysis*. Chemistry of Materials, 2005. **17**(18): p. 4577-4593.
103. Gasteiger, H.A., et al., *Activity benchmarks and requirements for Pt, Pt-alloy, and non-Pt oxygen reduction catalysts for PEMFCs*. Applied Catalysis B-Environmental, 2005. **56**(1-2): p. 9-35.
104. Gallis, K.W., et al., *The use of mesoporous silica in liquid chromatography*. Advanced Materials, 1999. **11**(17): p. 1452-1455.
105. Vallet-Regi, M., et al., *A new property of MCM-41: Drug delivery system*. Chemistry of Materials, 2001. **13**(2): p. 308-311.
106. Kresge, C.T., et al., *Ordered Mesoporous Molecular-Sieves Synthesized by a Liquid-Crystal Template Mechanism*. Nature, 1992. **359**(6397): p. 710-712.
107. Lu, Y.F., et al., *Aerosol-assisted self-assembly of mesostructured spherical nanoparticles*. Nature, 1999. **398**(6724): p. 223-226.
108. Lee, I., et al., *Generation of Monodisperse Mesoporous Silica Microspheres with Controllable Size and Surface Morphology in a Microfluidic Device*. Advanced Functional Materials, 2008. **18**(24): p. 4014-4021.
109. Holyst, R., A. Ciach, and W.T. Gozdz, *Ordering in Microemulsions*, in *Computational Methods in Surface and Colloid Science*, M. Borowko, Editor. 2000, Marcel Dekker: New York. p. 685-743.
110. Palmer, K.M. and D.C. Morse, *Statistical Mechanics of Microemulsions: Droplet Phases and Macroscopic Interfaces*. J. Chem. Phys., 1996. **105**(24): p. 11147.
111. Aveyard, R., B.P. Binks, and J. Mead, *Interfacial Tension Minima in Oil+Water+Surfactant Systems*. J. Chem. Soc. Faraday Trans. I, 1985. **81**: p. 2169-2177.
112. Aveyard, R., et al., *Interfacial Tension Minima in Oil- Water- Surfactant Systems*. J. Chem. Soc. Faraday Trans. I, 1986. **82**: p. 125-142.

113. Carroll, N.J., et al., *Droplet-based microfluidics for emulsion and solvent evaporation synthesis of monodisperse mesoporous silica microspheres*. Langmuir, 2008. **24**(3): p. 658-661.
114. Schmidt-Winkel, P., C.J. Glinka, and G.D. Stucky, *Microemulsion templates for mesoporous silica*. Langmuir, 2000. **16**(2): p. 356-361.
115. Van der Voort, P., M. Benjelloun, and E.F. Vansant, *Rationalization of the synthesis of SBA-16: Controlling the micro- and mesoporosity*. Journal of Physical Chemistry B, 2002. **106**(35): p. 9027-9032.
116. Schmidt-Winkel, P., C.J. Clinka, and G.D. Stucky, *Microemulsion Templates for Mesoporous Silica*. Langmuir, 2000. **16**: p. 356-361.
117. Schmidt-Winkel, P., et al., *Microemulsion Templating of Siliceous Mesostructured Cellular Foams with Well-Defined Ultralarge Mesopores*. Chem. Mater., 2000. **12**: p. 686-696.
118. El-Safty, S.A. and T. Hanaoka, *Microemulsion liquid crystal templates for highly ordered three-dimensional mesoporous silica monoliths with controllable mesopore structures*. Chemistry of Materials, 2004. **16**(3): p. 384-400.
119. Joo, S.H., et al., *Ordered nanoporous arrays of carbon supporting high dispersions of platinum nanoparticles*. Nature, 2001. **412**(6843): p. 169-172.
120. Chen, G.Y., S.R. Bare, and T.E. Mallouk, *Development of supported bifunctional electrocatalysts for unitized regenerative fuel cells*. Journal of the Electrochemical Society, 2002. **149**(8): p. A1092-A1099.
121. Garcia, B.L., R. Fuentes, and J.W. Weidner, *Low-temperature synthesis of a PtRu/Nb_{0.1}Ti_{0.9}O₂ electrocatalyst for methanol oxidation*. Electrochemical and Solid State Letters, 2007. **10**(7): p. B108-B110.
122. Ioroi, T., et al., *Stability of corrosion-resistant magneli-phase Ti₄O₇-supported PEMFC catalysts at high potentials*. Journal of the Electrochemical Society, 2008. **155**(4): p. B321-B326.
123. Sasaki, K. and R.R. Adzic, *Monolayer-level Ru- and NbO₂-Supported platinum electrocatalysts for methanol oxidation*. Journal of the Electrochemical Society, 2008. **155**(2): p. B180-B186.
124. Sasaki, K., L. Zhang, and R.R. Adzic, *Niobium oxide-supported platinum ultra-low amount electrocatalysts for oxygen reduction*. Physical Chemistry Chemical Physics, 2008. **10**(1): p. 159-167.
125. Carroll, N.J., Pylypenko, P., Atanassov, P.B., and Petsev, D.N. , *Microparticles with Bimodal Nanoporosity Derived by Microemulsion Templating*. Langmuir, 2009.
126. Liu, J.W., et al., *Electrostatically Mediated Liposome Fusion and Lipid Exchange with a Nanoparticle-Supported Bilayer for Control of Surface Charge, Drug Containment, and Delivery*. Journal of the American Chemical Society, 2009. **131**(22): p. 7567-+.
127. Ashley, C.E. and University of New Mexico. Dept. of Chemical and Nuclear Engineering., *Development of novel bio/nano interfaces for materials science and biomedical applications*, University of New Mexico, Dept. of Chemical and Nuclear Engineering, 2010. p. vii, 98 leaves.

128. Pylypenko, S., et al., *Non-platinum oxygen reduction electrocatalysts based on pyrolyzed transition metal macrocycles*. *Electrochimica Acta*, 2008. **53**(27): p. 7875-7883.
129. Vega, A.J. and G.W. Scherer, *STUDY OF STRUCTURAL EVOLUTION OF SILICA-GEL USING H-1 AND SI-29 NMR*. *Journal of Non-Crystalline Solids*, 1989. **111**(2-3): p. 153-166.
130. Carroll, N.J., et al., *Droplet-Based Microfluidics for Emulsion and Solvent Evaporation Synthesis of Monodisperse Mesoporous Silica Microspheres*. *Langmuir*, 2008. **24**: p. 658-661.
131. Bibette, J., *Depletion Interactions and Fractionated Crystallization for Polydisperse Emulsion Purification*. *J. Colloid Interface Sci.*, 1991. **147**: p. 474-478.
132. Bibette, J., et al., *Kinetically Induced Order in Gelation of Emulsions*. *Phys. Rev. Lett.*, 1992. **69**: p. 981-984.
133. Bibette, J., *Stability of Thin Films in Concentrated Emulsions*. *Langmuir*, 1992. **8**: p. 3178-3182.
134. Bibette, J., *Structure of Adhesive Emulsions*. *Langmuir*, 1993. **9**: p. 3352-3356.
135. Mason, T.G., J. Bibette, and D.A. Weitz, *Yelding and Flow of Monodisperse Emulsions*. *J. Colloid and Interface Sci.*, 1996. **179**: p. 439-448.
136. Mason, T.G. and J. Bibette, *Shear Rupturing of Droplets in Complex Fluids*. *Langmuir*, 1997. **13**: p. 4600-4613.
137. Umbanhowar, P.B., V. Prasad, and D.A. Weitz, *Monodisperse emulsion generation via drop break of in a coflowing stream*. *Langmuir*, 2000. **16**: p. 347-351.
138. Villermaux, E., *Fragmentation*. *Ann. Rev. Fluid Mech.*, 2007. **39**: p. 419-446.
139. Ahn, K., et al., *Dielectrophoretic Manipulation of Drops for High Speed Microfluidic Sorting Devices"*. *Appl. Phys. Lett.*, 2006. **88**: p. 024104.
140. Link, D.R., et al., *Electric control of droplets in microfluidic devices*. *Angew. Chem. Int. Ed.*, 2006. **45**: p. 2556 -2560.
141. Utada, A.S., et al., *Monodisperse Double Emulsions Generated from a Microcapillary Device*. *Science*, 2005. **308**: p. 537-541.
142. Garstecki, P., et al., *Formation of Monodisperse Bubbles in a Microfluidic Flow-Focusing Device*. *Appl. Phys. Lett.*, 2004. **45**: p. 2649-2651.
143. Lewis, P.C., et al., *Continuous Synthesis of Copolymer Particles in Microfluidic Reactors*. *Macromolecules*, 2005. **38**: p. 4536-4538.
144. Nie, Z., et al., *Polymer Particles with Various Shapes and Morphologies Produced in Continuous Microfluidic Reactors*. *J. Amer. Chem. Soc.*, 2005. **127**: p. 8058-8063.
145. Seo, M., et al., *Continuous Microfluidic Reactors For Polymer Particles*. *Langmuir*, 2005. **21**: p. 4773-4775.
146. Zhang, H., et al., *Microfluidic Production of Biopolymer Microcapsules with Controlled Morphology*. *J. Amer. Chem. Soc.*, 2006. **128**: p. 12205 -12210.
147. Zhang, H., et al., *Exploring Microfluidic Routes to Microgels of Biological Polymers*. *Macromol. Rapid Comm.*, 2007. **28**: p. 527-538.
148. Millman, J.R., et al., *Anisotropic particle synthesis in dielectrophoretically controlled microdroplet reactors*. *Nature Materials*, 2005. **4**: p. 98-102.
149. Velez, O.D., B.G. Prevo, and K.H. Bhatt, *On-chip Manipulation of Free Droplets*. *Nature*, 2003. **426**: p. 515-516.

150. Binks, B.P., et al., *Measurement of Film Rigidity and Interfacial Tension in Several Ionic Surfactant- Oil- Water Microemulsion Systems*. Langmuir, 1986. **5**: p. 1755.
151. Camardo, M., et al., *Effect of surfactant counterion on spectroscopic properties of water in oil microemulsions*. Colloids and Surfaces A: Physicochemical and Engineering Aspects, 1996. **119**: p. 183-187.
152. Chen, S.H., *Small angle neutron scattering studies of the structure and interaction in micellar and microemulsion systems*. Ann. Rev. Phys. Chem., 1986. **37**: p. 351-399.
153. Chen, S.-H. and E.Y. Sheu, *Interparticle Correlations in Concentrated Charged Colloidal Solutions -- Theory and Experiment*, in *Micellar Solutions and Microemulsions: Structure, Dynamics, and Statistical Mechanics*, S.-H. Chen and R. Rajagopalan, Editors. 1990, Springer-Verlag: New York.
154. Chew, C.H., et al., *Bicontinuous-Nanostructured Polymeric Materials from Microemulsion Polymerization*. Langmuir, 1998. **14**: p. 6068.
155. Denkov, N.D., et al., *Effect of Droplet Deformation on the Interactions in Microemulsions*. J. Colloid and Interface Sci., 1991. **143**: p. 157.
156. Fletcher, P.D.I. and D.N. Petsev, *A Model for the Temperature Dependent Interactions in Uncharged Droplet Microemulsions*. J. Chem. Soc..Faraday Trans., 1997. **93**: p. 1383-1388.
157. Goldszal, A. and M. Bourrel, *Demulsification of Crude Oil Emulsions: Correlation to Microemulsion Phase Behavior*. Ind. Eng. Chem., 2000. **39**: p. 2746-2751.
158. Lade, O., et al., *Polymerizable Nonionic Microemulsions: Phase Behavior of H₂O--n-Alkyl Methacrylate--n-Alkyl Poly(ethylene glycol) Ether (C_iE_j)*. Langmuir, 2000. **16**: p. 4122.
159. Milner, S.T. and S.A. Safran, *Dynamical Fluctuations of Droplet Microemulsions and Vesicles*. 1987. **36**: p. 4317.
160. Petsev, D.N. and P. Linse, *Statistical Mechanical Properties of Dense Emulsions and Microemulsions*. Phys. Rev . E., 1997. **55**: p. 586-591.
161. Petsev, D.N., *Structure and Film Formation in Charged Emulsions and Microemulsions*. Physica A, 1997. **250**: p. 115-132.
162. Petsev, D.N., *Interactions and Macroscopic Properties of Emulsions and Microemulsions*, in *Modern Aspects of Emulsion Science*, B.P. Binks, Editor. 1998, RSC: London.
163. Safran, S.A., *Fluctuations of Spherical Microemulsions*. J. Chem. Phys., 1983. **78**: p. 2073.
164. Teubner, M. and R. Strey, *Origin of Scattering Peak in Microemulsions*. J. Chem. Phys., 1987. **87**: p. 3195-3200.
165. Wang, L., X. Liu, and Y. Li, *Microemulsion Polymerization of Styrene Using Surface-Active Peresters as Photoinitiators*. Langmuir, 1998. **14**: p. 6879.
166. Wu, M., et al., *Microemulsion-Mediated Hydrothermal Synthesis and Characterization of nanosize Rutile and Anatase Particles*. Langmuir, 1999. **15**: p. 8822.
167. Imhof, A. and D.J. Pine, *Preparation of titania foams*. Adv. Mater., 1999. **11**: p. 311-314.
168. Schaht, S., et al., *Oil-water interface templating of mesoporous macroscale structures*. Science, 1996. **273**: p. 768-771.

169. Schmidt-Winkel, P., et al., *Mesocellular Siliceous Foams with Uniformly Sized Cells and Windows*. J. Am. Chem. Soc, 1999. **121**: p. 254-255.
170. Schmidt-Winkel, P., C.J. Glinka, and G.D. Stucky, *Microemulsion Templates for Mesoporous Silica*. Langmuir, 2000. **16**: p. 356-361.
171. El-Safty, S.A. and T. Hanaoka, *Microemulsion liquid crystal templates for highly ordered three-dimensional mesoporous silica monoliths with controllable mesopore structures*. Chem. Mater. **16**: p. 384-400.
172. Winsor, P.A., *Solvent Properties of Amphiphilic Compounds*. 1954, London: Butterworth.
173. Binks, B.P., *Emulsions*, in *Annu. Rep. Prog. Chem., Sect. C*. 1996. p. 97.
174. Lukens, W.W., et al., *Evaluating Pore Sizes in Mesoporous Materials: A Simplified Standard Adsorption Method and a Simplified Broekhoff-de Boer Method*. Langmuir, 1999. **15**: p. 5403-5409.
175. Duclaux, V., C. Clanet, and D. Quere, *The effects of gravity on the capillary instability in tubes*. Journal of Fluid Mechanics, 2006. **556**: p. 217-226.
176. Carroll, N.J., et al., *Microparticles with Bimodal Nanoporosity Derived by Microemulsion Templating*. Langmuir, 2009.
177. Aranberri, I., et al., *How do emulsions evaporate?* Langmuir, 2002. **18**(9): p. 3471-3475.
178. Mukerjee, S. and S. Srinivasan, *Enhanced Electrocatalysis of Oxygen Reduction on Platinum Alloys in Proton-Exchange Membrane Fuel-Cells*. Journal of Electroanalytical Chemistry, 1993. **357**(1-2): p. 201-224.
179. Mukerjee, S., et al., *Role of Structural and Electronic-Properties of Pt and Pt Alloys on Electrocatalysis of Oxygen Reduction - an in-Situ Xanes and Exafs Investigation*. Journal of the Electrochemical Society, 1995. **142**(5): p. 1409-1422.
180. Paulus, U.A., et al., *Oxygen reduction on carbon-supported Pt-Ni and Pt-Co alloy catalysts*. Journal of Physical Chemistry B, 2002. **106**(16): p. 4181-4191.
181. Koh, S. and P. Strasser, *Electrocatalysis on bimetallic surfaces: Modifying catalytic reactivity for oxygen reduction by voltammetric surface dealloying*. Journal of the American Chemical Society, 2007. **129**(42): p. 12624-+.
182. Neyerlin, K.C., et al., *Electrochemical activity and stability of dealloyed Pt-Cu and Pt-Cu-Co electrocatalysts for the oxygen reduction reaction (ORR)*. Journal of Power Sources, 2009. **186**(2): p. 261-267.
183. Adzic, R.R., et al., *Platinum monolayer fuel cell electrocatalysts*. Topics in Catalysis, 2007. **46**(3-4): p. 249-262.
184. Debe, M.K., et al., *High voltage stability of nanostructured thin film catalysts for PEM fuel cells*. Journal of Power Sources, 2006. **161**(2): p. 1002-1011.
185. Dodelet, J.P., *Oxygen reduction in PEM fuel cell conditions : heat-treated non-precious metal-N4 macrocycles and beyond*, in *N4-macrocyclic metal complexes*, J.H. Zagal, Bedioui, F., Dodelet, J. P., Editor. 2006, Springer Science + Business Media Inc.: New York. p. 83-150.
186. Borup, R., et al., *Scientific aspects of polymer electrolyte fuel cell durability and degradation*. Chemical Reviews, 2007. **107**(10): p. 3904-3951.

187. Lee, J., J. Kim, and T. Hyeon, *Recent progress in the synthesis of porous carbon materials*. *Advanced Materials*, 2006. **18**(16): p. 2073-2094.
188. Liang, C.D., Z.J. Li, and S. Dai, *Mesoporous carbon materials: Synthesis and modification*. *Angewandte Chemie-International Edition*, 2008. **47**(20): p. 3696-3717.
189. Stein, A., Z.Y. Wang, and M.A. Fierke, *Functionalization of Porous Carbon Materials with Designed Pore Architecture*. *Advanced Materials*, 2009. **21**(3): p. 265-293.
190. Raghuveer, V. and A. Manthiram, *Mesoporous carbon with larger pore diameter as an electrocatalyst support for methanol oxidation*. *Electrochemical and Solid State Letters*, 2004. **7**(10): p. A336-A339.
191. Chang, H., S.H. Joo, and C. Pak, *Synthesis and characterization of mesoporous carbon for fuel cell applications*. *Journal of Materials Chemistry*, 2007. **17**(30): p. 3078-3088.
192. Kim, T.W., I.S. Park, and R. Ryoo, *A synthetic route to ordered mesoporous carbon materials with graphitic pore walls*. *Angewandte Chemie-International Edition*, 2003. **42**(36): p. 4375-4379.
193. Choi, M. and R. Ryoo, *Mesoporous carbons with KOH activated framework and their hydrogen adsorption*. *Journal of Materials Chemistry*, 2007. **17**(39): p. 4204-4209.
194. Ryoo, R., S.H. Joo, and S.J. Choi, *Ordered mesoporous carbons exhibiting extraordinary metal dispersion*. *Abstracts of Papers of the American Chemical Society*, 2001. **221**: p. U475-U475.
195. Joo, S.H., S. Jun, and R. Ryoo, *Synthesis of ordered mesoporous carbon molecular sieves CMK-1*. *Microporous and Mesoporous Materials*, 2001. **44**: p. 153-158.
196. Olson, T.S., K. Chapman, and P. Atanassov, *Non-platinum cathode catalyst layer composition for single membrane electrode assembly proton exchange membrane fuel cell*. *Journal of Power Sources*, 2008. **183**(2): p. 557-563.
197. Olson, T.S., et al., *Electrochemical Evaluation of Porous Non-Platinum Oxygen Reduction Catalysts for Polymer Electrolyte Fuel Cells*. *Fuel Cells*, 2009. **9999**(9999): p. NA.
198. Olson, T.S., et al., *Bifunctional Oxygen Reduction Reaction Mechanism on Non-Platinum Catalysts Derived from Pyrolyzed Porphyrins*. *Journal of the Electrochemical Society*, 2010. **157**(1): p. B54-B63.
199. Ziegelbauer, J.M., et al., *Direct spectroscopic observation of the structural origin of peroxide generation from co-based pyrolyzed porphyrins for ORR applications*. *Journal of Physical Chemistry C*, 2008. **112**(24): p. 8839-8849.
200. Artyushkova, K., et al., *Predictive modeling of electrocatalyst structure based on structure-to-property correlations of X-ray photoelectron spectroscopic and electrochemical measurements*. *Langmuir*, 2008. **24**(16): p. 9082-9088.
201. Artyushkova, K., et al., *XPS structural studies of nano-composite non-platinum electrocatalysts for polymer electrolyte fuel cells*. *Topics in Catalysis*, 2007. **46**(3-4): p. 263-275.
202. Jaouen, F.d.r., et al., *Cross-Laboratory Experimental Study of Non-Noble-Metal Electrocatalysts for the Oxygen Reduction Reaction*. *Acs Applied Materials & Interfaces*, 2009.

203. Switzer, E.E., et al., *Templated Pt-Sn electrocatalysts for ethanol, methanol and CO oxidation in alkaline media*. *Electrochimica Acta*, 2009. **54**(3): p. 989-995.
204. Beamson, G. and D. Briggs, *High resolution XPS of organic polymers : the Scienta ESCA300 database*. 1992, Chichester [England] ; New York: Wiley. 295 p.
205. Paulus, U.A., et al., *Oxygen reduction on a high-surface area Pt/Vulcan carbon catalyst: a thin-film rotating ring-disk electrode study*. *Journal of Electroanalytical Chemistry*, 2001. **495**(2): p. 134-145.
206. Guilminot, E., et al., *Comparing the thin-film rotating disk electrode and the ultramicroelectrode with cavity techniques to study carbon-supported platinum for proton exchange membrane fuel cell applications*. *Journal of Electroanalytical Chemistry*, 2007. **599**(1): p. 111-120.
207. Kumaresan, R. and S.M. Babu, *Crystal growth and characterization of sucrose single crystals*. *Materials Chemistry and Physics*, 1997. **49**(1): p. 83-86.
208. Kralchevsky, P.A. and K. Nagayama, *Particles at Fluid Interfaces and Membranes*. 2001, Amsterdam: Elsevier.
209. Kralchevsky, P.A. and K. Nagayama, *Capillary Interactions between Particles Bound to Interfaces, Liquid Films and Biomembranes*. *Adv. Colloid Interface Sci.*, 2000. **85**: p. 145-192.
210. Nagayama, K. and P.A. Kralchevsky, *Two-Dimensional Forces Universally Working between Particles at an Interface*. *J. Phys. Soc. (Japan)*, 1999. **54**: p. 519-527.
211. Kralchevsky, P.A., *Lateral Forces Acting between Particles in Liquid Films or Lipid Membranes*. *Adv. Biophys.*, 1997. **34**: p. 25-39.
212. Kralchevsky, P.A., et al., *Formation of Two-dimensional Colloid Crystals in Liquid Films under the Action of Capillary Forces*. *J. Phys.: Condens. Matter.*, 1994. **6**: p. A395-A402.
213. Denkov, N.D., et al., *Two-Dimensional Crystallization*. *Nature*, 1993. **361**: p. 26-26.
214. Denkov, N.D., et al., *Mechanism of Formation of Two-Dimensional Crystals from Latex Particles on Substrates*. *Langmuir*, 1992. **8**: p. 3183-3190.